Imaging Skin Structures for Health, Body Mapping, and Identification (Under the Tucson Skin)

by

Ina Annesha Kundu Benjamin

B.S. in Mechanical Engineering, University of Arizona (2013)
B.S. in Mathematics, University of Arizona (2013)
M.S. in Mechanical Engineering, Massachusetts Institute of Technology (2015)

Submitted to the Department of Mechanical Engineering
In partial fulfillment of the requirements for the degree of
Doctor of Philosophy in Mechanical Engineering
at the

MASSACHUSETTS INSTITUTE OF TECHNOLOGY

June 2018

Author..... Signature redacted .....
Department of Mechanical Engineering
May 25, 2018

Certified by... Signature redacted .....
Brian W. Anthony
Principal Research Scientist, Department of Mechanical Engineering
Thesis Supervisor

Accepted by..... Signature redacted
Rohan Abeyaratne
Professor, Department of Mechanical Engineering
Graduate Officer

ABSTRACT

The human skin is dense with features that can be imaged and then analyzed for applications in human health. Applications include using natural body landmarks as a position encoding system for the body, as potential biometric identifiers, and as biomarkers correlated to health. Monitoring these features over time may be useful in the early diagnosis of several health conditions. Two prominent naturally occurring networks of features on the body are the skin microrelief and the superficial vascular structures just below the skin surface. Microreliefs are the fine micrometer scale furrows and ridges that appear like irregular geometric patterns on the skin surface; often, the intersection of the microrelief lines are at the outlets of the sweat ducts, which are used to regulate body temperature. The superficial vasculature is the subdermal network of veins responsible for supplying blood to the body. Since these features have important biological functions, monitoring the evolution of these features over time may be impactful.

Long-term monitoring of these networks and network features may be useful for noninvasive methods to aid in computer-assisted diagnosis of numerous dermatological diseases and assessment of overall health. However, it is challenging to accurately observe the microrelief structure and its evolution and variation over time due to its micrometer dimensions distributed over square meters of the body and the 3D non-rigid nature of the body. Imaging the vasculature is difficult as it is below the skin surface. Current optical imaging technology to penetrate the skin surface is expensive. Image processing algorithms often incorrectly identify the subdermal features, mistaking the veins with other similarly shaped skin surface features (like deep wrinkles). Therefore, the evolution of healthy superficial vascular structure has not been well studied. Registration and matching of the skin and vascular regions are further complicated by non-rigid deformation, variations in illumination, and other noise sources.

We have designed handheld optical imaging systems in an attempt to address these challenges through a combination of image system design and image processing. The two systems designed and presented here are (1) a high resolution, visible spectrum imaging device to image the skin microrelief and (2) a near-infrared (NIR) imaging system to image the superficial vascular structure. Both systems are ergonomic, lightweight, portable, easily integrated into common

computer systems and relatively inexpensive, thereby having the potential to be used in clinical settings.

We designed the optical imaging systems to have a convenient form factor while ensuring high-quality imaging of skin features at different length scales. Repeatability experiments were performed over a period of 1 – 2 years. Finally, we developed custom registration and matching algorithms to robustly extract and compare the biological networks on and below the surface of the skin.

In an IRB approved study, 16 – 20 healthy volunteers were tested serially in order to characterize the systems. For a controlled set of motions, the vein imaging system correctly finds a position on the body within 5% error (or 0.22cm of true position) and corrects angular viewpoint variations within 3% error. Vein structures are noted to be stable over a span of 8 months. Using real and synthetic skin images, the microrelief imaging system achieved matching accuracies of 26μm - 80μm. The skin structure is found to be stable over a period of 1 – 2 years.

Because it has been shown that these networks are stable over time, they hold promise in being used as a human body positioning system, a non-invasive diagnostic tool, and an accurate biometric identifier.

Thesis Supervisor: Brian W. Anthony

Title: Principal Research Engineer, Mechanical Engineering and Institute for Medical Engineering and Science

ACKNOWLEDGEMENTS

It is when you reach those precious milestones in life that you realize how lucky you are to have the wonderful, loving, and supportive network that helped get you there. Getting a PhD is no different. After nearly two decades of schooling, the degree culminates in a hundred some odd page document (this thesis) after which people will forever call you "Doctor." But it isn't the document that must be celebrated and acknowledged, but rather the journey. As Carl Friedrich Gauss once said, "it is not knowledge, but the act of learning, not possession but the act of getting there, which grants the greatest enjoyment." And I was fortunate enough to have the unconditional love, support, and encouragement from my family and friends that made this such an enjoyable journey! I take this moment now to recognize a few special individuals who significantly influenced my academic and personal life.

I must first thank my doctoral committee for their academic and research advice. Professor Maria Yang inspired me to pursue product design and Professor Juejun (JJ) Hu always had valuable clinical questions to motivate the research work. Of course, my advisor, Dr. Brian Anthony, requires a special mention without whose financial and academic support this research would not have been possible. A father and entrepreneur himself, Brian ran his lab like a small company; the nearly 30 graduate students were always given life advice as they met one-on-one, in small groups, or in big gatherings, and we were always expected to become specialists in our own projects. Our lab (The Device Realization Lab) had fun navigating Brian's calendar to figure out when he might be free or which of his predictions about his graduate students would come true next.

Being such a big lab, we always had something to do together: eat lunch, go bowling, watch movies, play poker, discuss wedding planning details, figure out ways to make veins pop, or whatever the new topic of the day was – somehow we found time to hang out beyond the lab despite the continuous stream of students coming and leaving the basement lab of building 35.

Then there were the friendships formed outside the lab circle. From my time on the Graduate Student Council Executive Board (GSC ExComm), Graduate Association of Mechanical Engineers (GAME), Ashdown House Officer Team, and Muddy Charles Board of Governors, I encountered a diverse set of individuals who further enriched my time at Boston and MIT. There

are too many of you to name individually, but you all know who you are – thank you for making my Boston experience such a memorable one. From social events to weekly meetings, we found time to hang out and make a difference in the broader MIT community.

Planning the largest social event on campus for graduate students (the GSC Grad Gala) and organizing the largest student run orientation in the nation, it seemed there was always time for fun and parties at school. It was through planning these parties that I formed close bonds with like-minded individuals. Alex Guo, Bomy Lee Chung, Amy Gao, Wardah Inam, and Filiz Yitisir – all our shopping trips, girls nights, and movie nights were a welcome break after discussing image processing with men all the time – it's fun, but sometimes we just want to talk about shoes!

Finally, I come to my family – both born into and that which I acquired during grad school. My parents were the first to teach me about manners and how to be a good person, an education more valuable than any famed institution could ever provide. As I was faced with a number of challenges, my mom never stopped supporting me with her nurturing nature. It was through her constant attention to all my needs that I was able to recover from a debilitating bout of acute pancreatitis during my time at MIT. Despite my father's training as an engineer, we hardly ever talked work or research; being a man of few words, he always saved his one-liners to entertain the family during family vacations and to bond with my husband during the week of our wedding. My sister, Auni...there are no words left to describe her or our relationship. From stressing about grad school to celebrating my engagement with our unique version of a bachelorette party, we had an eventful few years. Although we lived on opposite coasts, she always made me laugh with her constant "puppies in pajamas" photos or videos of fainting goats!

But family isn't only the one you are born into. Through my time in grad school, I had the great fortune of befriending, dating, and finally marrying one of the most amazing, thoughtful, generous, and intelligent people I have ever met, Rishon Benjamin. He introduced me to the wonders of coffee and was a calming presence when I stressed about various facets of life (wedding planning, graduation, travels). It was through our relationship that I gained a second family. My in-laws, Annie and Robert Benjamin, always wished me well, especially during the final stages of the PhD. Alex Benjamin, Rishon's twin brother, was one of my closest friends and favorite labmates – we discussed everything from women to homographies to famous mathematicians.

To all my family and friends: thank you for always supporting me and making me who I am; this PhD would not have been possible without you!

CONTENTS

Abstract **3**

Acknowledgements **5**

Contents **7**

Figures **11**

Tables **19**

1 ..... **21**

Introduction **21**

1.1 Clinical Relevance 22

1.2 Skin Microrelief 22

1.2.1 Microrelief Structure 23

1.2.2 Imaging Technologies 24

1.2.3 Existing Registration Techniques 25

1.3 Veins 26

1.3.1 Veins for Health 27

1.3.2 Veins as a Biometric Identifier 28

1.3.3 Superficial Veins 28

1.3.4 Near Infrared (NIR) Imaging 29

1.3.5 Existing Technology 30

1.4 Skin and Veins Are Connected 31

1.5 Gaps in Existing Literature 32

1.6 Our Work 33

2 ..... **35**

Microrelief **35**

2.1 Mitutoyo Vision System (Microscope) 36

2.1.1 Acquiring Images with the Microscope 38

2.1.2 Sample Images Analyzed 40
2.1.3 Challenges of the Microscope 41
2.2 Handheld Skin Imaging Device Design 42
2.2.1 Camera and Lens 42
2.2.1.1 Optical Parameters 43
2.2.2 Lighting 45
2.2.2.1 Lighting Calibration 45
2.2.2.2 Light Invariance 46
2.2.3 Housing Fixture 46
2.3 Experimental Procedure 49
2.3.1 Long Term Monitoring of the Skin 51
2.3.2 Large Area Skin Patch 53
2.4 Methodology 54
2.4.1 Registration and Matching Overview 55
2.4.1.1 Keypoint Detection 56
2.4.1.2 RANSAC Homography Estimate 57
2.4.2 Skin Point Pattern Matching 58
2.4.2.1 Extraction of Microrelief Structure 58
2.4.2.2 Junction Point Detection 59
2.4.2.3 Voronoi-Based Point Pattern Matching (PPM) 59
2.5 Microrelief Results 62
2.5.1 Ground Truth 62
2.5.2 Evaluation Criteria 62
2.5.3 Algorithms Used on Experimental Images 65
2.6 Summary of Microrelief Work 68
2.6.1 Potential Design Changes 69
2.6.2 Limitations and Future Work 69

3 71

Superficial Vasculature 71

3.1 Handheld Vein Imaging Device 72
3.1.1 NIR Camera 73

3.1.1.1 NIR Camera Control 74
3.1.1.2 Other NIR Cameras Considered 75
3.1.2 Light Source 76
3.1.2.1 Alternate Light Options 78
3.1.3 Housing Fixture 79
3.1.3.1 Iteration 1 80
3.1.3.2 Iteration 2 82
3.1.3.3 Future Iterations and Design Changes 83
3.2 Acquiring Vein Images (Experimental Procedure) 84
3.2.1 Experiments 86
3.3 Processing the Vein Images (Image Processing) 86
3.4 Results 93
3.4.1 Re-Localization (Vascular Body Map) 93
3.4.2 Vascular Stability over Time 94
3.4.3 Sensitivity Analysis 99
3.4.3.1 Algorithm Robustness 99
3.4.3.2 Device Robustness 101
3.4.4 Use as a Biometric 104
3.4.4.1 Qualitative Approach 104
3.4.4.2 Quantitative Approach 106
3.4.4.3 Future Work for Characterizing the Vasculature 109
3.4.5 Error Analysis 110
3.4.5.1 Discussion about the Errors along the Axes 113
3.4.6 Characterizing the Overall System 115
3.5 Summary of Vein Imaging Work 116
3.5.1 Limitations of Current System 116
3.5.2 Future Work 118

4 121

Conclusions And Future Work 121

4.1 Skin and Vein Network Commonalities 121
4.2 Future Work 124

4.2.1 Future Design Changes 124
4.2.2 Future Experiments 124
4.2.3 Improved Biological Understanding 125

References 127

A 133

Appendices 133

A.1 Homography Overview 133
A.2 Vein Code Overview 134
A.3 Skin Registration and Matching Procedure 136

FIGURES

Figure 1: Microrelief Structure of the Skin Surface: Furrows intersect at junction points to form geometric patterns (i.e. the ridge) 23
Figure 2: Imaging System for Microrelief Structure: The principle of the skin image acquisition device is shown here. It consists of white LED lamps to illuminate the skin surface, an optical transmission magnifying glass, and a 6mm x 8mm CCD sensor to image. This schematic is reproduced from [6]. 24
Figure 3: Near Infrared (NIR) Image of the Vasculature: Blood absorbs IR light, so the blood vessels appear darker than surrounding skin and tissue 29
Figure 4: Skin and Vein Relationship: Vessels and capillaries are found in the dermis layer of the skin 32
Figure 5: Mitutoyo Vision System: (a) The Mitutoyo vision system integrated on the Quick Vision Active 220 Microscope. The lens and light move together orthogonal and parallel to the imaged region, which rests on the glass plate. (b) Connecting the Quick Vision Active System to a PC with accompanying software to manipulate camera parameters (such as magnification, focus, and aperture size). (c) Subject arm placement on custom designed armrest such that the ring light uniformly illuminates ROI and the ROI is normal to the lens. 37
Figure 6: Sample Microrelief Image Obtained by the Mitutoyo Vision System: This sample comes from the underside of the forearm where the primary and secondary lines are clearly visible. The image resolution is 7μm/pixel, which gives an average ridge thickness of 0.175mm and an average plateau area of 0.1455mm^2. Image dimensions are provided in the figure 38
Figure 7: Camera Motion during Experimentation: The head of the Quick Vision Active system moves along the direction of the arrows towards increasing number of image frames, as indicated in the figure. The thick red borders indicate the amount of overlap between the frames. There are 20 images acquired in a 1 in^2 area on the skin. 39
Figure 8: Extracting the Microrelief Pattern: The blue lines are the ridges of the microrelief extracted during image processing. The primary lines are especially prominent. This particular image was provided by a collaborator, Judy Beaudoin. 41

Figure 9: Geometry to Calculate Depth of Field (DoF): This geometry assumes a 10° maximum rotation of the image region (i.e. the forearm). The WD and its relationship to the DoF is also shown in this figure..... 44
Figure 10: Effects of White Balancing in (a) Nominal lighting conditions and (b) Poor lighting conditions..... 46
Figure 11: Custom Designed and Fabricated Camera Mount: (a) Mount with high resolution camera, frame, and LED light ring (b) Ergonomic hold and USB to micro-USB connector cable (for a "plug-and-play" system)..... 47
Figure 12: Skin Scanning Experimental Setup: (a) Subject places arm in a comfortable position on top of a solid surface. The device is rotated and aligned with the scan region, such that the lens is perpendicular to the skin surface and the ring is flush against the skin surface. (b) Red square stamp used for alignment purposes and to enhance the micorelief structure. (c) Custom designed user interface with LabView where the operator aligns the stamp with the on-screen red square before taking an image..... 49
Figure 13: Enhancing Microrelief Structure with Ink: The stamp ink bleeds into the microrelief ridges, which enhances the contrast between the ridges and plateaus. This is contrasted with the other area of the skin surface (no ink), which has less of a contrast..... 50
Figure 14: Skin Patch Imaged for Long Term Monitoring: The part of the forearm that is roughly planar and has minimal distortion is used as a second monitoring point on the forearm (the first monitoring point is on the wrist). Across subjects with forearm lengths of 7in – 10in, this area tends to be 2in – 3in from the elbow crease..... 51
Figure 15: Skin Scanning Workflow: (a) Image acquisition with custom built handheld device (b) Hair detection and algorithmic removal (c) Image registration and matching: the purple and green networks are the computer contrived feature points that are detected from the pre-processed skin images of the same skin image at two instances of time. These features are what the computer determines are the intersection points (i.e. junction points) of the microreliefs. The white points are the matched feature points between the two networks obtained on different days..... 53
Figure 16: Flowchart of Proposed Algorithm for Skin Registration and Matching: Target image, I_A, and source image, I_B, are inputs to the registration and matching algorithm. The grey blocks are the global transformation, which aligns the images based on differing viewpoints and large-

scale skin stretching. The blue blocks are the local transformation which corrects for deformation of the skin due to curvature and other nonlinearities. 56
Figure 17: Sample Images and Detected SIFT Keypoints: (a) The target image, I_A, and source image, I_B, taken some time later (b) The detected SIFT keypoints that are consistent throughout the image between the target and source images. 57
Figure 18: Algorithm Flowchart for the Microrelief Structure Matching Procedure 58
Figure 19: Voronoi-Based Junction Point Matching Results: Each Voronoi cell is constructed around the SIFT keypoints. Junction points within the cell are matched. Corresponding cells have the same shape and are denoted with the same color across a pair of images. 61
Figure 20: Correspondence Points Overlaid on Raw Images 61
Figure 21: Evaluating the Developed Registration and Matching Algorithms (NN) to Existing Shape Context Matching Algorithms (CS): (a) Matching Accuracy – developed NN algorithms are accurate within 1-3 pixels, existing CS algorithms are less accurate (7 – 12 pixel accuracy) (b) Computation Time - NN algorithms take approximately 2 seconds to match 1000 junction points; CS algorithms take a little over 1 second for 1000 junction points (c) Missing Point Ratios – nearly 70% of the junction points are used for matching between two images, this suggests nearly 20-30% missing points 64
Figure 22: The Registration and Matching Process Illustrated: a) Target image, I_A, taken at the initial visit (b) Real source image, I_B, taken some time later (c) Synthetic source image with rotation and translation, $I_{B'}$, (d) Registered target and source images, (e) Highlight of registered SIFT keypoint structure, (f) Voronoi cells for matching the registered images 65
Figure 23: A Sample Set of Experimental Images and Registration Results over Time (1.5 years): (a) Target image (b) Source image acquired after 18 months (c) Registered target and source images overlaid; ROI in red rectangle is used for matching 66
Figure 24: A Sample Set of Experimental Images and Registration Results on Subjects with Hair: (a) The target and source images of a ROI with hair. The camera is also rotated, significantly altering the viewpoint. (b) The registered target and source images overlaid; the red rectangle is the region used for matching. (c) A close-up view of the SIFT keypoint patterns of the target and source images where the hair is clearly discernible. The green points are the SIFT network from the target image, pink points are the SIFT network from the source image, and the white points illustrate the overlapping locations between the target and source images. 66

Figure 25: A Sample Set of Experimental Images and Registration Results on a Young Subject: : (a) The target and source images of a ROI on a child. The ROI is stretched to significantly alter the viewpoint. (b) The registered target and source images overlaid; the red rectangle is the region used for matching. (c) A close-up view of the SIFT keypoint patterns of the target and source images. The green points are the SIFT network from the target image, pink points are the SIFT network from the source image, and the white points illustrate the overlapping locations between the target and source images. The SIFT keypoint network appears much denser than in other subjects (primary and secondary lines clearly distinguishable)..... 67
Figure 26: Technical Specifications for the Manta G145B-NIR camera and the M1620-MPW2 Lens: (a) Quantum efficiency curve for Manta G145B-NIR camera shows the camera meets the minimum clinical requirements of more than 30% QE at 800nm. (b) Transmission curve for the M1620-MPW2 lens shows it is transparent in the NIR range of 700nm – 1000nm..... 74
Figure 27: Blood Absorption Based on Wavelength: Veins carry deoxygenated blood from the tissues back to the heart, so we care about the blue line of the graph. We must image at wavelengths >580nm to image the veins instead of the artery where the absorption of the blood vessels is greater than the absorption for the veins [75]. 77
Figure 28: Reflections on ROI from Broadband Source 78
Figure 29: Uniform Lighting and Visible Veins in ROI using a Tungsten Bulb for Illuminating the ROI..... 79
Figure 30: Light, Camera, and ROI Configuration for High Quality Vein Images: The light and camera must be on the same side with relation to the ROI (i.e. the forearm) in order to image the reflected light from the forearm, which makes the veins more prominent. 79
Figure 31: Ring Light Flush with Camera Lens for a Convenient Form Factor and Maximum Portability..... 80
Figure 32: Camera and Light Fixture: By keeping the light hidden from view, we keep a small form factor to make it handheld and more aesthetically pleasing. 81
Figure 33: Ergonomics of the Handheld Vein Imaging Device: (a) Slot cuts to adjust the focus and exposure of the lens (b) Contoured housing surface for a more comfortable hold. There is just enough material to encase and secure the components to the mount. 81
Figure 34: Ergonomic and DFA Considerations on the Mount: The camera aligns in the (a) back and (b) front with the properly dimensioned mounts..... 82

Figure 35: Contoured Base along the ROI: This base helps increase device stability during experimentation 82
Figure 36: Breadboard LED Ring Light: This breadboard prototype incorporates visible spectrum and NIR LEDs with wavelengths of 660nm, 680nm, 780nm, 850nm, 870nm, 910nm, and 940nm. 83
Figure 37: Experimental Setup for Acquiring Vein Images: The forearm is kept flat on a hard surface with the handheld device on top such that the camera is always perpendicular to the ROI as shown. The device moves along the length of the forearm from elbow to wrist, as indicated with the dotted arrow. 85
Figure 38: Setup of Controlled Experiments: (a) Forearm exercise to increase blood flow in the forearm veins. (b) Blood vessel constriction above elbow to allow blood pooling in the veins at the elbow as in phlebotomy. (c) Using weights to increase blood flow in the forearm for subjects with veins that are hard to see. 86
Figure 39: Overview of Image Processing Steps to Get a Vein Map of the Body 87
Figure 40: Pre-Processing Raw Images (Left) to Enhance the Vasculature and Eliminate Surface Effects. The result is the binarized, vein segmented image (right) 88
Figure 41: The binarized vein image shows the prominent vascular network structure along with some artifacts from the pre-processing. 88
Figure 42: Alternate Pre-Processing Options: (a) Skeletonizing the image: the network is visible, but the lines do not resemble the vasculature visible to the human eye. (b) Edge detection makes the vessel structure more visible, but the features matched from these images do not result from the vascular features. 90
Figure 43: SURF Features detection on the segmented vessel images: (a) There are 1500+ detected SURF features on the binarized vessel images, (b) Only approximately 100 of the detected features are unique and can be used for matching. 90
Figure 44: Registration Process Between Two Images: (a) Matched feature points between two images are shown with the corresponding yellow lines; there are 100+ matched feature points between two images. (b) Inlier points are the strongest matches from (a) that are used for registering the images. 5 inlier points are required for registration to solve the homography matrix; many more points would be redundant to solve the system and may lead to detecting unreliable feature points. 92

Figure 45: Stitched Images: (a) Two images are overlaid and matched at the locations corresponding to their inlier points. The green shows the areas of vasculature in the first image and non-vasculature in the second image; the pink lines show the vascular structure of the second image, but not in the first image; the black lines in the white space show the overlapping vascular network that is present in both images; the white space are the regions of no vasculature in both images. (b) Multiple images stitched together get the full stitch of the arm, which serves as the "vascular map" of the arm. 92
Figure 46: Re-Localization of a Random Image within an Arm Stitch: With feature-based re-localization, small viewpoint changes (up to 30°) do not affect the ability to find a random image within a map. The same random image can be found within a stitch from two different viewpoints, (a) and (b)..... 94
Figure 47: Re-Localization of a Small Image (Local Vasculature) within an Arm Stitch over Time: The prominent features of the vascular network for this subject can be re-localized over time as shown with the black lines overlapping in the white region. (a) Small local image taken same day as arm stitch is generated. (b) Small local image taken 1 day after arm stitch is generated. (c) Small local image taken 60 days (2 months) after arm stitch is generated. (d) Small local image taken 240 days (8 months) after arm stitch is generated. 96
Figure 48: Segmenting the Various Colored Pixels to Understand Vascular Stability Over Time (Data for one subject at one instance of time.): We care about the amount of pink + black and green + black pixels over time to understand if the amount of vessels is changing over time..... 97
Figure 49: Vein Matching over Time: Proportion of vasculature present in images over a period of 8 months. Corresponds to data in Table 10. Error bars at 5% illustrate the data is consistent over a number of data sets. 98
Figure 50: Vein Matching over Short Time Periods: Proportion of vasculature present in images over short period (2 months). The proportion of vessels in the image and the percent of vessel matching stay constant in the short term. Error bars at 5% illustrate the data is consistent over a number of data sets. 99
Figure 51: A synthetically stretched image patch is found within the full forearm map. A stretch of 150 pixels along the length and width of the binarized image correlates to a 1.5cm stretch of the vessels, which can still be found within the original forearm map. Black indicates matching vascular pixels as before. 100

Figure 52: A synthetically compressed image patch is found within the full forearm map. A compression of 100 pixels along the length and width of the binarized image correlates to a 1cm compression of the vessels, which can still be found within the original forearm map. Black indicates matching vascular pixels as before. 101
Figure 53: Experimental Images to Test Device Robustness: The median cubital vein is more prominent after constricting flow above the elbow (b) compared to (a) since the constriction allows the blood to pool in the vein. 102
Figure 54: Vessels along the length of the forearm: The median cubital vein, ulnar artery, and basilic vein are prominent in the vein images acquired. They can be measured to understand normal vessel size variation across a population. 103
Figure 55: Variation as a Function of Vessel Size: This graph illustrates the amount of vessel deformation correlated to the undeformed width of the median cubital vein. With this sample set, we find that the data is not normally distributed, but can determine the range of variation in vessels across our healthy volunteer population. 103
Figure 56: Vasculature Maps of the Forearm for a Pair of Identical Twins: (a) Subject 1 (b) Subject 2..... 104
Figure 57: Demonstration of Uniqueness of Superficial Vasculature: Forearm vascular images taken from a pair of identical twins. (a) A failed registration attempt of an image from the forearm of Subject 1 in Subject 2's forearm stitch. (b) A failed registration attempt of an image from the forearm of Subject 2 in Subject 1's forearm stitch. (c) A failed registration attempt of the forearm of Subject 1 with the forearm of Subject 2. 106
Figure 58: Magnitude Plot of Fourier Transform of Vascular Images: The aggregate directions of the vasculature between subjects 1 and 2 do not align as noticed with the lack of overlap between green and pink lines. 106
Figure 59: Process Overview to Extract Desired Features for Characterizing Vein Images..... 107
Figure 60: The forearm map of the vasculature reduced to a series of lines and branch points: The white lines in the pink background shows how the vessels are reduced to single pixel lines; the branch points of the network are the intersection and crossing points, similar to the junction points in the skin microrelief images. 107
Figure 61: Characteristics Extracted from the Vein Network: The angle of the vessels with respect to the horizontal, the average length of the vein segments, the length of the smallest vessels, and

the size of the branch point clusters can be extracted from the network of lines and branch points to characterize the network. 108
Figure 62: OptiTrak Setup for Determining Ground Truth: (a) The experimental process is the same as described in Section 3.2 with the device orthogonal to the ROI. (b) The OptiTrak Trio looks at the IR reflective balls, which are placed on the camera to track camera motion. (c) Motive (OptiTrak's accompanying software) looks at the motion of the 3 balls through the 3 cameras. (d) The camera oriented along the ROI: x is along the scan direction, y is the width of the scan region, and z is the distance of the ROI from the camera. 111
Figure 63: Output from the OptiTrak Trio: There are 6 images captured for this particular subject as labeled with "Rand" indicating the small image patch taken from some point along the forearm. To get the true distance, we use the coordinates of the relative distance (coordinates of random image – coordinates of image 1). 112
Figure 64: Random Image Correctly Positioned after Rotating and Translating the Arm: Controlled experimentation to showcase the current limitations of the algorithm and hardware setup given that the body is 3D. However, we are still able to find the image within a larger image patch. 117
Figure 65: Drawback of One Camera System to Detect Curvature: Multiple images of small angle rotations of the forearm stitched together are seen as many small linear translations rather than small angle rotations. Therefore, to "unwrap" the human limb, we would need two cameras to understand true curvature, rather than the one camera system we have designed. 117
Figure 66: Sample Images and Vein Extractions of Other Parts of the Body: (a) The biceps (b) The hamstrings 118
Figure 67: Experimental Images of Skin and Veins with Dimensions Provided: (a) Vein images are larger and the features are more prominent because of greater contrast between the veins and surrounding skin (b) Skin images are smaller in size and features are less prominent because of the limited contrast between shallow microrelief and skin 122
Figure 68: Skin and Vein Imaging Devices: (a) Skin microrelief imaging device (b) Vein imaging device. Both are handheld and comprise of a camera, light source, and housing fixture. 123

TABLES

Table 1: Skin Imaging Technologies for Various Applications 25
Table 2: Existing Vein Imaging Technology: Benefits and Limitations 31
Table 3: Design Requirement for Skin Imaging System: Requirements determined as primary or secondary based on clinical and technical specifications. 36
Table 4: Results of Light Calibration Using Color Card QP101 46
Table 5: How Custom Designed Device Satisfies Design Requirements 48
Table 6: Summary of Subject Distribution: The IRB approved study had a variety of subjects ranging in age from 4.5 to 45. Here is a summary of the 16 long-term subjects. 52
Table 7: Handheld System Benchmarked Against Comparable Technology 68
Table 8: System Design Requirements to Image the Superficial Vasculature 72
Table 9: Possible Features to Extract from the Vein Images for Matching 89
Table 10: Vein Matching Over Time: Comparing proportion of vasculature present over time. Corresponds to Figure 47 and Figure 49 98
Table 11: Sensitivity Analysis with Simulated Expansion/Contraction of Blood Vessels 101
Table 12: Network Characteristics for Quantifying Vasculature 109
Table 13: Output of the Homography Matrix from the Algorithms: The last column provides the linear motion in the x and y axes with pixel values. Using the resolution (0.01cm/pixel), the motion in physical units is calculated. 112
Table 14: Error between Predicted (Developed Algorithms) and True (OptiTrak) Motion 113
Table 15: Skin and Vein Devices Compared 123

CHAPTER

1

INTRODUCTION

The human body contains a number of naturally occurring networks that are clinically important. In this thesis, we concentrate on skin and vascular networks. Structural changes observed in these networks have clinical significance as they can aid in disease diagnosis and determining the overall health of an individual. Furthermore, stability of these networks suggests their usability as body positioning systems. There is a clinical and scientific value to study these networks in the human body.

Optical imaging is a powerful, noninvasive method for studying the networks on and just below the body's surface. A combination of hardware and software solutions may allow for computer-assisted diagnosis of numerous dermatological diseases and overall health assessment. By monitoring the evolution of various skin features, we can track indicators of health of an individual. We are interested in using the unique feature networks of the body as a biometric for person identification and body location mapping. However, imaging technology is often prohibitively expensive for consumer and clinical use. From the technical standpoint, imaging the features is difficult due to the varying length scales of feature size and area of distribution and the 3D non-rigid nature of the body. Image analysis is also complicated by inconsistent illumination, non-rigid deformation, and other noise sources.

Two networks of interest explored in this thesis are the microrelief and superficial vein structures. "Microreliefs" are the fine micrometer scale furrows and ridges that appear like irregular geometric patterns on the skin surface. A subdermal network made of veins close to the skin surface comprise the superficial vein structure. Each of these networks is explained in greater detail in the subsequent sections.

1.1 Clinical Relevance

Before we begin an in depth discussion of the various features found on the human body, it is important to understand *why* we choose to study these features and what we hope to accomplish. Recall: we are curious about how stable the skin and vein networks are over time (both short and long term). If these networks are not changing with time (i.e. stable), they can be used for two purposes: (1) a biometric identifier since the network is unique to individual and (2) a body positioning system since the network is unique depending on body part.

Structural changes observed in the networks can provide insight into disease progression, since these changes may be correlated to underlying health conditions. Thus, we are curious about the time and length scales at which we need features to be stable for clinical relevance. To understand the time scales at which the features must be stable, we use current clinical practice as a benchmark. Dermatologists follow up with at-risk skin cancer patients four times a year, so the skin networks must be stable for at least three months. Follow ups for patients with varicose veins occur twice a year, so the vein networks must be stable for at least six months. The length scale at which these features must be stable is an unanswered scientific question that we hope to answer with the work presented in this thesis. However, we can again use clinical practice to benchmark the limits: moles on the order of millimeters and vein diameters on the order of centimeters are observed over time for disease progression. With this foundation, we can now delve deeper into the various skin features.

1.2 Skin Microrelief

Skin is the body's largest organ and serves as the body's first line of defense against harmful pathogens and microbes. Properties (i.e. structure, elasticity, and color) of skin can be used to aid in the diagnosis and treatment of several diseases. Observing and quantifying skin features and their properties over time may be useful to characterize the rate and severity of disease progression. Much prior work has been done for skin cancer and its evolution [1]–[3] and the population based aging effects on skin (i.e. wrinkles) [4]–[8]. Little research has been conducted in observing an individuals' skin feature stability and evolution because of the difficulty in properly imaging the irregular geometric patterns on the skin surface.

1.2.1 Microrelief Structure

A close visual inspection of human skin at the 20μm to 8mm scale reveals intersecting fine ridges that create geometric patterns. These are the "microrelief" of the skin (Figure 1) [9]. The mechanical forces imposed on the tissue from the underlying muscle and collagen fibers create a net-like structure comprised of triangles and quadrangles to form the microrelief pattern [6], [10]. These patterns are created by a combination of environmental and genetic factors that exhibit characteristic patterns for different regions of the body; they are particularly prominent on the wrists and forearms [10], [11].

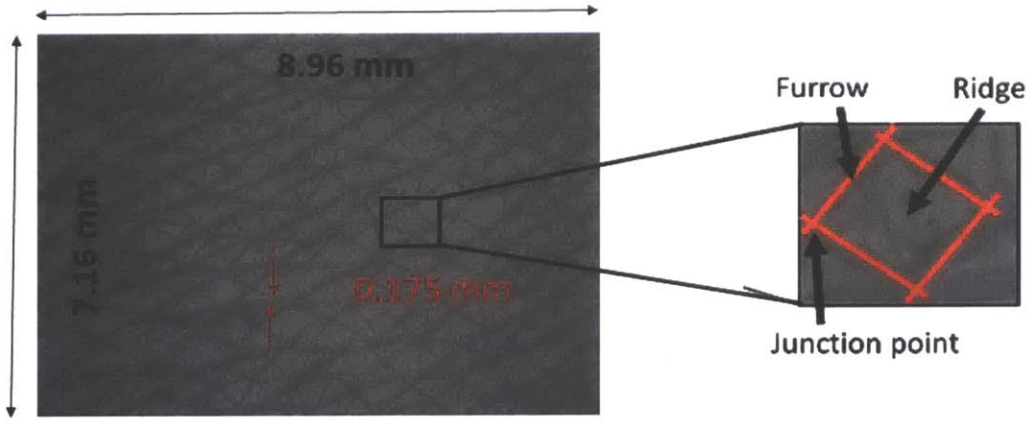

Figure 1: Microrelief Structure of the Skin Surface: Furrows intersect at junction points to form geometric patterns (i.e. the ridge)

Microrelief structure also changes with age [6], [10]. As elasticity decreases, the skin folding capacity increases, forming wrinkles that become increasingly common with age. Zou et. al studied the aging effects on forearm microrelief structure. The sampled population age ranged from 10-79 years of age [6]. The authors identified two types of skin lines which form the skin structure: (1) "primary lines" in a prominent direction that are 20μm - 100μm deep and get deeper with age, and (2) other "secondary lines" that are 5μm - 40μm deep and disappear with age [6], [12]. The secondary lines were found to be mostly orthogonal to the primary lines during youth and become increasingly parallel to the primary lines with age.

1.2.2 Imaging Technologies

Imaging the skin structure in order to extract accurate and precise measurements is difficult since image properties vary with imaging parameters, such as viewing angles and illumination angles [1], [13]. The complex optical properties of skin and the geometry of pores and wrinkles cause reflections, making it difficult to consistently image the skin. Hardware, imaging methodologies, and technologies have been developed to address these challenges. Two example approaches are described below.

Zou et. al studied the changing forearm microrelief structure at 50x zoom by using a USB skin detector produced by Boseview Technology Company (Figure 2) [6]. However, this system has several limitations. Without any polarizing filters to minimize light diffusion, there are specular reflections (i.e. "hot spots") on images for subjects with oily, smooth, or well-moisturized skin. Additionally, directional lighting induces shadows on uneven surfaces. Shadows and hot spots are eliminated by the algorithm developed, not the device itself.

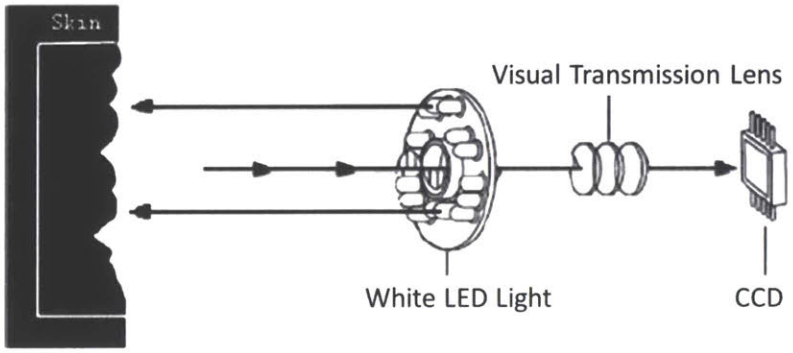

Figure 2: Imaging System for Microrelief Structure: The principle of the skin image acquisition device is shown here. It consists of white LED lamps to illuminate the skin surface, an optical transmission magnifying glass, and a 6mm x 8mm CCD sensor to image. This schematic is reproduced from [6].

An alternate method to image the skin microrelief structure uses the amount of light absorbed through a replica of the skin with a device called "The Skin Visiometer" [14]. The skin replica is a thin piece of silicone with the skin texture artificially fabricated onto its surface; this replica measures 9mm x 6.7mm and is placed between a light emitting diode (LED) light source and a black-and-white, high resolution (5MP) CMOS camera. A software program then converts the amount of light absorbed through the silicone replica to reproduce the skin valleys and give a

topographical view of the skin surface. The device weighs 2.7kg and measures 26cm x 24cm x 7cm [15]. Other skin imaging technologies have been detailed in [16] and are summarized below in Table 1.

Table 1: Skin Imaging Technologies for Various Applications

Imaging Platforms	Application	Benefits	Drawbacks
Finger Knuckle Print	Imaging the finger knuckles	Repeatable images, consistent lighting, ergonomic	Limited imaging region (only finger knuckle)
USB Skin Detector	Microrelief	Image at 50x zoom, pigment, pores, and microreliefs can be imaged	Shadows, specular reflections in image (i.e. non-uniform lighting)
Skin Visiometer	Microrelief	5MP camera, light absorption to get skin topography	Skin replica required
Video Microscopy	Microrelief	100x zoom	No lighting changes permissible
Confocal Laser Scanning Microscopy (CLSM)	Microreliefs	Lighting can be controlled	Small imaging area
Capacitance Imaging (CI)	Microrelief, hydration state	High resolution	Sensitive to external moisture
Corneometer	Skin hydration	Accurate to 3%	Uses capacitance changes to measure hydration, so cannot image other skin features
Colorimeter	Skin color	Characterize red color resulting from blood flow	RGB data used for skin color only

1.2.3 Existing Registration Techniques

Most computational skin analysis has been devoted to analyzing and matching the microrelief patterns that appear on fingerprints for biometric identification applications [17]. Methods of fingerprint registration algorithms rely on macro-features and have limited registration accuracy at the micrometer scale, which is the size of microreliefs.

Skin microrelief registration is challenging. The general skin surface is non-planar and external strain gives rise to noticeable stretching of the surface. Additionally, the skin surface lacks high-

contrast boundaries and results in relatively low-contrast repetitive patterns across an image. Thus, many deformable registration algorithms are not robust and are susceptible to incorrect matching.

Researchers have investigated a number of rigid skin registration techniques. A common approach is to identify a sparse set of landmarks in two images and align the images by a homography transformation. These algorithms use the SIFT key point matching method proposed by Lowe and are used for the registration of cutaneous hemoangioma and melanocytic nevus [18]–[20]. However, these algorithms only work well for images where the features have high-contrast boundaries; they do not model situations where the skin is locally deformed or slightly curved (like the forearm). Madan *et al.* used keypoints extracted from various skin microscale features such as pigmentation, pores, and hair follicles, for time-lapse multimodal facial skin registration via homography warping [21]. They designed a chinrest to fix the face in a position and acquired multimode images every second, reducing the problem of mismatches. However, the clinical setting would have unconstrained patient movement when monitoring over time, which further complicates the registration.

Additionally, rigid registration does not allow us to register the free skin surface accurately. A homography transformation does not model situations in which the skin is locally deformed, nor does it take into account different viewpoints of a slightly curved surface, like the forearm. Several studies have proposed non-rigid registration methods to register pairs of stress-deformed, full-field 2D skin images using physical markers [22]. Naturally, it is inconvenient and impractical to fix these markers at the microscale and on human skin, especially for long-term skin monitoring. An efficient and robust constellation point pattern matching (PPM) algorithm like [23] is desirable to match the junction points of the skin network. However, [23] is limited by a rigid matching trajectory for a regular and repetitive point pattern. These limitations require improving the SIFT feature-based registration methods and developing matching algorithms for microscale skin features, which we accomplish in this work.

1.3 Veins

The human circulatory system is comprised of 60,000 – 100,000 miles of arteries, veins, and vessels, supporting nearly 1800 gallons of blood flow daily [24]. Most commonly thought of for their role in cardiovascular health, the veins also serve other purposes. Two prominent uses for veins are in (1) better understanding the overall health of an individual (such as kidney function

and skin health [25]) by looking at aspects like an individual's hydration state [26] and abnormalities in the vascular structure [27], [28] and (2) using the vasculature as a biometric identifier [29].

Determined by neural guidance and blood flow during embryogenesis, the vein network structure and positioning is partly genetic. Epigenetic factors (such as blood flow and tissue oxygenation) are responsible for the remainder of the tree network [30], [31]. Because vein patterns are created from the combined effects of genetic and epigenetic factors, they are unique. Making up 20% of the volume of the dermis, the vascular network also helps with regulating body temperature; as the body warms up, the blood vessels expand, allowing the heat to escape through the skin surface [27].

1.3.1 Veins for Health

Changes in the vascular network are important for diagnosing venous disease since the structural changes can account for 80-90% of deep vein problems [32]–[34]. Examples of vasculature changes are in the number of vessels, vessel spacing, and abnormalities in the vein network [25]. More variable than arterial anatomy, the venous anatomy helps to understand chronic venous disease and helps with surgical planning. Chronic venous disease commonly manifests itself in varicose veins, which result from a lack of support from the saphenous veins in the legs [32], [35].

Nearly 2-4% of varicose veins progress to deep vein thrombosis (DVT), a painful condition caused by a blood clot that results in leg swelling [33]. Patients are at a higher risk of thrombus after undergoing hip and knee replacements, so a non-invasive way to monitor and track these patients is important. Ultrasound modalities are commonly used to estimate the risks of DVT by monitoring and tracking the critical sites over time. This proves difficult since there is no way to know the exact body location for monitoring over serial exams [28], [33]. Furthermore, ultrasound imaging systems are typically more expensive than the optical approaches we propose here, require significant training, and the gel makes the setup messy and sometimes uncomfortable for patients.

Veins are also important in other clinical areas. In phlebotomy, or the clinical practice of drawing blood for diagnosis, the veins are the puncture sites, so there is a need to enhance and locate the ideal vein locations [34], [36]. Dermatologists also look for injection sites when trying to eliminate varicose and spider veins for the procedure known as sclerotherapy [37]. Clinicians mostly observe the vasculature with their naked eye since other technologies (i.e. confocal

microscopy) are either too expensive or image further below the skin surface than desired. A small device (such as the Dermatoscope) is desired, which can be used to diagnose vasculitis (a condition where the blood vessels are inflamed) and vasculopathy (a condition where obstructions in the blood vessels lead to skin manifestations) [38]. The superficial vasculature also helps dermatologists diagnose diseases, such as basal cell carcinomas and lupus [37], [38].

1.3.2 Veins as a Biometric Identifier

Veins are a promising biometric identifier since the "patterns are 100 times more unique than fingerprints" [29], [39]. It is believed (though not yet proven) that vein patterns are unique among individuals and on different parts of the body. The stability of the vasculature is disputed; some claim the structure is unaffected by aging [39], [40] while others claim the blood pumps in different patterns with age and are continually restructuring [24]. Additionally, since veins are subdermal (i.e. lie below the skin), the vein pattern cannot be falsely duplicated. This seemingly more secure form of identification (compared to fingerprints) is gaining popularity in places like Japan and India where fingerprint and palm scanning devices are used in financial institutions and for attendance purposes [41].

1.3.3 Superficial Veins

Superficial veins, closer to the skin surface, aid in cooling the body by collecting blood from the surrounding superficial tissues and exchanging the heat outside the body via the skin [42]. They are also responsible for transporting blood to the deep veins, which are closer to the muscles [43]. Veins carry deoxygenated blood from tissues back to heart unlike arteries, which carry blood away from the heart. The superficial veins are mostly prominent in the limbs and vary in size; some are small enough to be invisible to the naked eye (diameters vary from 100μm – 0.8mm) [27], [44]. However, normal variation in vascular size and structure is unknown. No known studies of long term monitoring of veins in healthy individuals have been performed [33].

Veins lie as deep as 15mm below the skin surface, with veins in the lower extremity as deep as 4cm [33]. However, clinically, veins only as deep as 10mm (1cm) are important for diagnostic and phlebotomy purposes [36], [45]. Methods, such as ultrasound and near infrared imaging, can see veins as shallow as 2.7mm (with ultrasound) to as deep as 7.8mm (near infrared imaging) [44].

1.3.4 Near Infrared (NIR) Imaging

Infrared (IR) imaging is a relatively fast (nearly 400 frames per second), non-invasive imaging modality. It has been used for a variety of applications including: understanding the hydration state of individuals [26], [27], visualizing blood flow [46], using the vascular structure for biometric authentication [29], [39], and being used to assist in phlebotomy [47]. IR imaging is ideal for imaging veins because the hemoglobin found in blood absorbs light in the 760nm range, which makes the blood vessels appear darker than the surrounding tissue (Figure 3) [27], [39]. Additionally, since no probe contact is required, IR imaging is more reproducible over time unlike spectroscopy, which is commonly used to study biological tissues. Non-invasive IR imaging also preserves the geometry of smaller, feeder veins which can aid in later diagnosis of vascular disease. These feeder veins are biologically important, but often collapse under the pressure from ultrasound probes during ultrasound imaging.

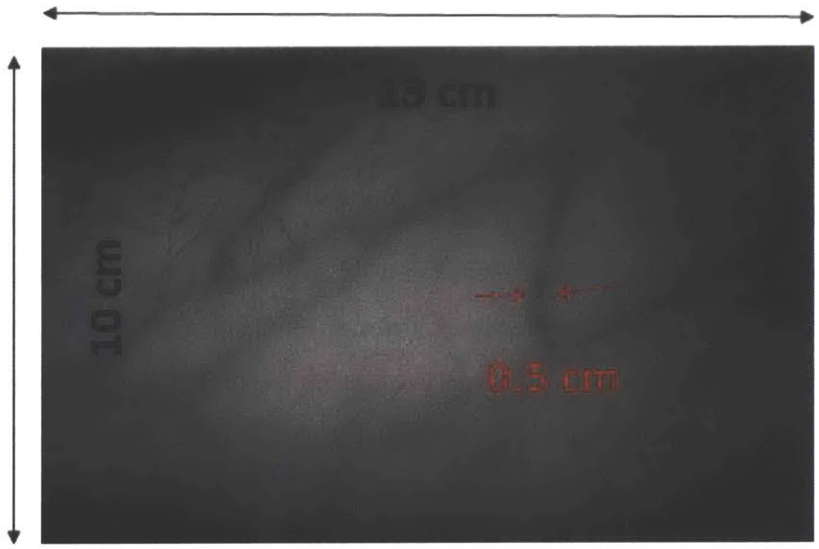

Figure 3: Near Infrared (NIR) Image of the Vasculature: Blood absorbs IR light, so the blood vessels appear darker than surrounding skin and tissue.

The IR spectrum is classified into near infrared (NIR) and far infrared (FIR). NIR spectrum spans 650nm – 1700nm, of which 780nm – 950nm is clinically relevant [26], [27], [34]; FIR spans 1000nm – 1700nm. For vein imaging, NIR is preferred to FIR since NIR images are tolerant to environmental changes and changes in physical attributes whereas FIR images are not [40]. For example, NIR images look identical regardless of ambient room temperature whereas FIR images

do not. Additionally, NIR imaging can capture smaller veins (and more of the vascular network) than FIR imaging, which is only good for the prominent veins on the back of the hand. However, NIR imaging is not robust to surface features (i.e. skin texture, hair, and wrinkles); most NIR images capture visible spectrum features since the NIR spectrum borders the visible spectrum. These extraneous features need to be removed through later image processing.

1.3.5 Existing Technology

Commercially developed by Hitachi in 1997, Vein Pattern Recognition (VPR) technology has been rapidly developed and used in recent years. VPR technology provides high quality images at a high price point (up to $4000 compared to simple fingerprint scanners costing $500) [41]. Although the FBI and CIA currently use vein matching techniques, these practices do not extend to crime labs due to lack of reliability and the higher price point compared to current fingerprinting techniques [19], [29], [39]. However, since vein imaging does not require contacting the skin (unlike most fingerprinting technology), it can be more sanitary and used by a wider audience, including people with diseased skin.

Many NIR technologies have been developed to image and study the vasculature for research and commercial use. Most of these technologies use CCD cameras and require a light source [27], [39]. Since the human body is a source of IR radiation, a separate radiation light source may not be necessary [40]. However, the imaged area should still have uniform illumination to see the features, so an external light source is required. Prior work found that in addition to having a light source, high quality images result from properly selecting the imaging wavelength, which depends on skin pigmentation (760nm for pale skin, 920nm for darker skin [48]). Benefits and limitations of selected existing technology are provided in Table 2.

Table 2: Existing Vein Imaging Technology: Benefits and Limitations

Product	Technology and Uses	Benefits	Drawbacks
Logitech Pro 2000 Webcam [39]	Sensitive to IR region by using a diffusion filter; IR LEDs used for high contrast; Concentric LED arrays used for uniform lighting	Low-Cost; Uniform Lighting; Portable	Limited Resolution; Images only the palm
PC-1280 with Visible Filter [34]	Monochrome camera with visible cutoff filter; Emitters at two different wavelengths and at various angles to illuminate region of interest; Used to study identification capabilities of vasculature in finger and dorsal hand veins	Filter allows imaging in only NIR spectrum; Variable lighting for high quality images	Illumination not consistent and not uniform; Image processing does not differentiate between small veins and wrinkles
Vein Eye [36]	Real-time digital image of patient vasculature to find optimal venipuncture site	Used for phlebotomy; Portable	Costly
Luminetx VeinViewer [47]	Use IR filter on real-time video capture to get only the veins; Enhances images of subcutaneous veins onto subjects skin	Real-time image capture of veins; Constant contrast images	Need to calibrate alignment for each subject; Variable focal distance depending on subject; Not "plug-and-play" solution

1.4 Skin and Veins Are Connected

The skin and vein networks are biologically and physiologically connected as seen in Figure 4. Both are clinically relevant for diagnosis and can be used as a biometric identifier. Both have properties that can be imaged and analyzed to understand overall health of an individual. And both inspired the development of various technology to image and analyze the features.

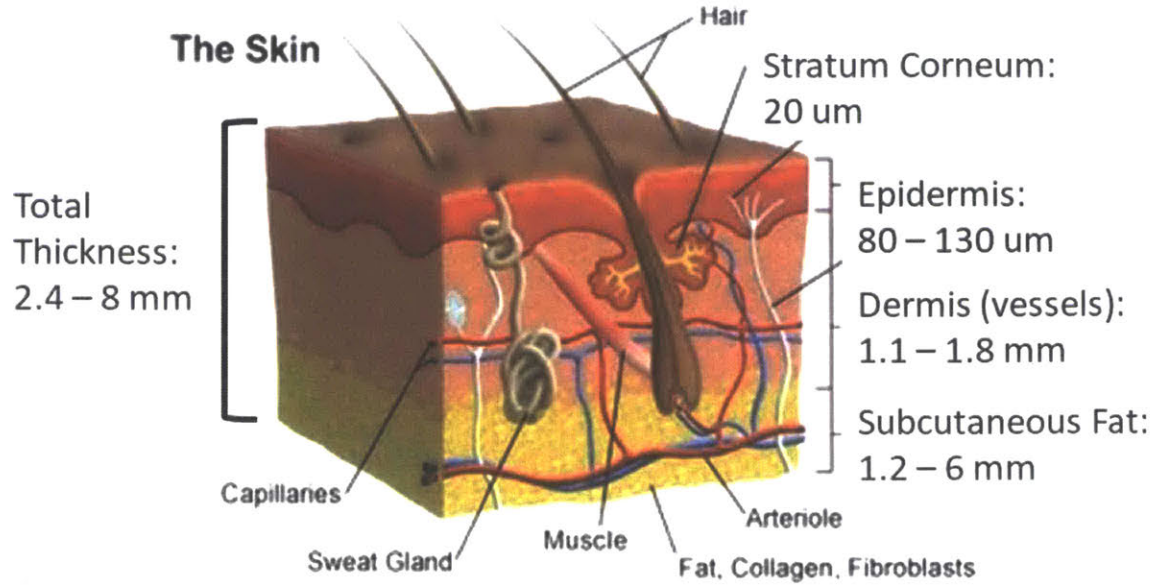

Figure 4: Skin and Vein Relationship: Vessels and capillaries are found in the dermis layer of the skin

Unsurprisingly, a number of venous diseases have skin manifestations. Examples include superficial thrombophlebitis, Raynaud's phenomenon, renal artery disease, and peripheral artery disease [49]. More commonly known, the skin and veins help regulate body temperature; i.e. cold temperatures reduce blood flow (veins get smaller) and increase surface area (presence of goosebumps). Thus, imaging the skin in conjunction with the veins gives insight into the overall health state of an individual.

1.5 Gaps in Existing Literature

Despite the various technology developed and experiments conducted in the space of skin and veins, there remain a number of unanswered questions. Especially absent are the areas of structure stability – skin and veins are thought to be stable, yet restructuring of biologic tissue is well known. What are the time scales at which these features are stable? Few people have carried out longitudinal experiments on healthy individuals, so normal variation in feature size and shape is unknown. Additionally, there is no standard on the repeatable imaging and analysis of the features – what is the imaging procedure to ensure repeatable image capture? How should the images be registered to understand change over time? Finally, most technology does not permit full-body

image capture; thus, existing work focuses on the structures in the palms or wrists. We seek to fill these gaps as summarized in Section 1.6.

1.6 Our Work

Imaging and analyzing the skin and vein networks over time is clinically important with applications including, but not limited to, (1) understanding the overall health of an individual, (2) using naturally occurring networks as a body position encoding system, and (3) using skin features as a form of biometric identifier. As such, studying skin and veins have been extensively studied as mentioned in the preceding sections.

Apart from the technologies described, other hardware and imaging methodologies have been developed to image and study the skin and veins. However, no single system has seen widespread use in clinics. This is likely because all the technologies have some limitations that prohibit their clinical usability. For clinical use, the system should be handheld, lightweight, inexpensive, and easy-to-use. With associated developed algorithms, the overall system must be light invariant for use in any setting regardless of ambient lighting conditions. Lastly, for longitudinal monitoring of network stability, the system must allow repeatable image capture.

To address these clinical requirements, we developed handheld imaging devices and custom algorithms to image the skin and vein structures and analyze their stability and evolution over time. With a compact design, the developed systems enable large area scanning to demonstrate that skin and veins are unique among individuals and distinct in each part of the body, which have not yet been proven. To our knowledge, this is the first system of its kind that can understand skin structure or venous anatomy over time and enables looking at feature variation in healthy individuals. With proper experimental setup and algorithms, repeatable image capture is possible, which allow us to use the body networks as a body positioning system (i.e. finding a particular position on the body based on the features). Lastly, we provide the hardware and software that can enable long-term feature monitoring for early diagnosis of health conditions through non-invasive means. The device design, experimental process, algorithm development, and results are presented here. Chapter 2 discusses the skin microrelief work and Chapter 3 discusses the vein work. Chapter 4 ends the thesis with conclusions and future work.

CHAPTER

2

MICRORELIEF

Techniques to image and analyze the skin microrelief structure could be used to monitor skin health or to develop a position encoding system for the body. Since these techniques require both hardware and software innovations, we outline them in this section. Clinical and technical requirements drive the design of the custom developed handheld device. Algorithms are customized for the micrometer length scale features and tested for robustness and accuracy.

The imaging technology must allow for high-resolution imaging of the skin surface to discern the microrelief features. For clinical and consumer use, the hardware must be lightweight, easy-to-use, and inexpensive. A handheld form factor is desired for portability and enabling placement on any location of the body. To assess the stability of the microrelief features and understand their change over time, the overall system must permit repeatable image capture. This means the system should be robust to changes in ambient light and viewing angles. Here, we consider the system to include the imaging hardware, support hardware required during imaging, and algorithms. Balanced system integration is desired. The design requirements are summarized in Table 3.

In this section, we discuss the hardware and software developed to study the skin structure. Outlined first are the two imaging systems used and developed to acquire images of the skin (other imaging systems considered can be found in [16]). Following that is an outline of the algorithms developed. This chapter concludes with sample results of a skin patch localized over time and an analysis of the developed technologies.

Table 3: Design Requirement for Skin Imaging System: Requirements determined as primary or secondary based on clinical and technical specifications.

Requirement	Specification/Design Parameter	Primary/Secondary?
The system can image skin features on the body.	Image features on length scales from 20 μm to 10 mm with sufficiently large FOV (at least 1"x1")	Primary
The system allows image parameters to be varied.	Change camera exposure, lighting parameters, and optical zoom.	Primary
The system provides high quality images.	Image has uniform lighting. User can resolve all skin surface features.	Primary
The system can take repeatable images.	Can return to same imaged region multiple times.	Primary
The system prevents deformation of the skin surface.	Minimize contact area.	Primary
The system is easy to use.	"Plug-and-play" system.	Secondary
The system can be used anywhere and at any time of day.	System is light invariant.	Secondary
The system is lightweight.	System is less than 4 kg.	Secondary
The system is ergonomic.	Operators do not have to use extra attachments during imaging. Subjects do not have to rest body parts on hard surfaces or hold body in uncomfortable positions for long times.	Secondary
The system is cost – effective.	System costs less than existing state-of-the-art technology at $20,000 (Ideally, system should be <$1000).	Secondary
The system is portable.	System is handheld.	Secondary

2.1 Mitutoyo Vision System (Microscope)

The Quick Vision Active 220 microscope is equipped with the Mitutoyo Vision System (Mitutoyo America Corporation, Illinois 60502) and is used to look at the primary and secondary lines of the microrelief pattern on the forearm (Figure 5). In this configuration, the lens and light move together

normal and parallel to the imaged region; the imaged region rests on the glass plate as shown in Figure 5a. Accompanying software (QVPAK3D Vision) and calibration targets from Mitutoyo are used to calibrate the microscope lens at the desired feature level; the nominal magnification and aperture are found to be 1.5 and 0.12, respectively. Under these settings, the captured image resolution is 7μm/pixel.

QVPAK3D Vision software can also manipulate various camera parameters (such as focal depth, light intensity/saturation, and direction of illumination) to acquire high-resolution images at each capture. For acquiring good quality skin images, a top-down ring light at 8% intensity is integrated onto the 1.5x objective lens providing uniform lighting onto the region of interest (ROI). This intensity level is automatically detected to prevent light reflections from the surface of the ROI, while also making the skin microrelief prominent.

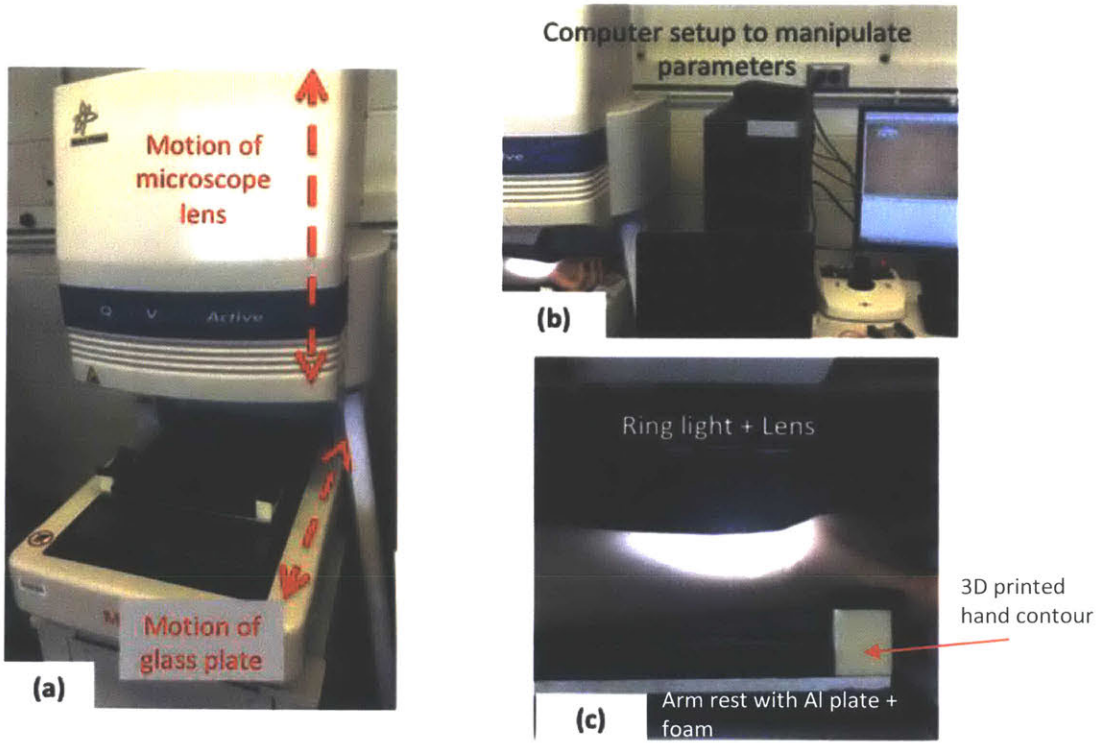

Figure 5: Mitutoyo Vision System: (a) The Mitutoyo vision system integrated on the Quick Vision Active 220 Microscope. The lens and light move together orthogonal and parallel to the imaged region, which rests on the glass plate. **(b)** Connecting the Quick Vision Active System to a PC with accompanying software to manipulate camera parameters (such as magnification, focus, and aperture size). **(c)** Subject arm placement on custom designed armrest such that the ring light uniformly illuminates ROI and the ROI is normal to the lens.

2.1.1 Acquiring Images with the Microscope

A custom designed armrest is used during experimentation. It is fabricated from a piece of aluminum (sized to length of the subject's forearm), some foam sponges to provide padding and support from the aluminum plate, and 3D printed contours for the hands (Figure 5c). Subjects are asked to place their arm on the armrest such that the underside of the forearm is normal to the lens as shown in Figure 5c. In this configuration, the ring light uniformly illuminates the ROI and the lens gets the top down view of the microrelief. Using the QVPAK 3D software, the ROI is automatically focused, the light intensity is set after the region is tested for oversaturation (or excessive lighting in the image), and the skin patch is imaged and saved.

A sample image is shown in Figure 6, where the primary and secondary lines are clearly discernable. The acquired images represent a 7.16mm x 8.96mm patch on the skin. With lighting optimized by the QVPAK 3D software as described above, there is good contrast between the microrelief ridges and the plateaus. The average ridge is 25 pixels thick; with a resolution of 7μm/pixel, the ridges are 175μm, or 0.175mm, thick. Similarly, the average plateau is a quadrangle measuring 54 pixels x 55 pixels; again, using the 7μm/pixel resolution, we get the average area of the plateau to be 0.1455mm^2.

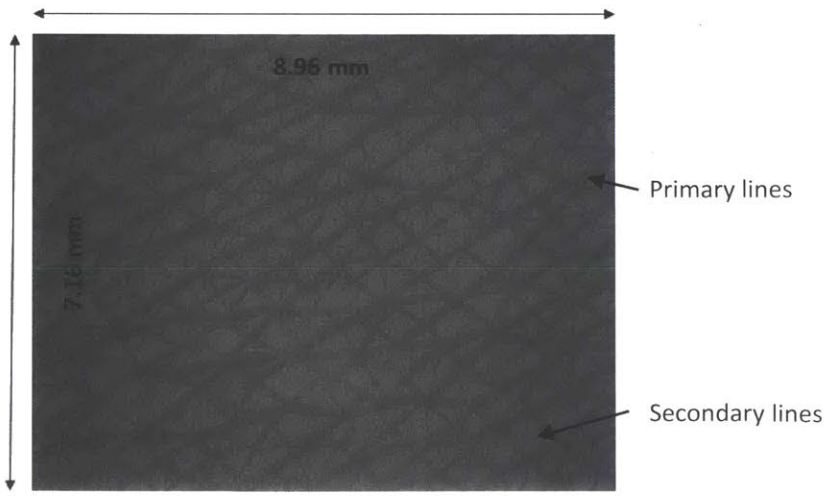

Figure 6: Sample Microrelief Image Obtained by the Mitutoyo Vision System: This sample comes from the underside of the forearm where the primary and secondary lines are clearly visible. The image resolution is 7μm/pixel, which gives an average ridge thickness of 0.175mm and an average plateau area of 0.1455mm^2. Image dimensions are provided in the figure.

A small image region, like that of Figure 6, is not useful as a standalone; we need a larger skin region to obtain useful information about the skin and its structure (i.e. say something about skin health or use skin structure for body positioning). Thus, the experimental process must be designed such that a large area patch can be imaged and analyzed. During experimentation, images are acquired with a certain amount of overlap between image frames to enable the later stitching process. Stitching images together with image processing provides the large area skin patch.

Figure 7 shows the motion of the camera required to image a 1 in^2 (6.45 cm^2) patch of skin. The operator controls the lens of the Quick Vision Active system with a joystick to move between image frames. Manually, the operator determines the amount of sufficient overlap and stops the motion of the camera. Typically, $^1/_4$ to $^1/_3$ of the image is used for overlap where there are enough microrelief features to match one image to the next. The skin image is acquired with the QVPAK 3D software as described previously. Twenty images are required to image the square patch, taking roughly twenty - thirty minutes per scan. These long scan times result from (1) the operator having to manually determine the amount of overlap, thereby moving the joystick (and camera) slowly across the ROI, (2) the camera having to autofocus and determine the appropriate illumination at each image, and (3) the operator manually saving each image in the appropriate folder.

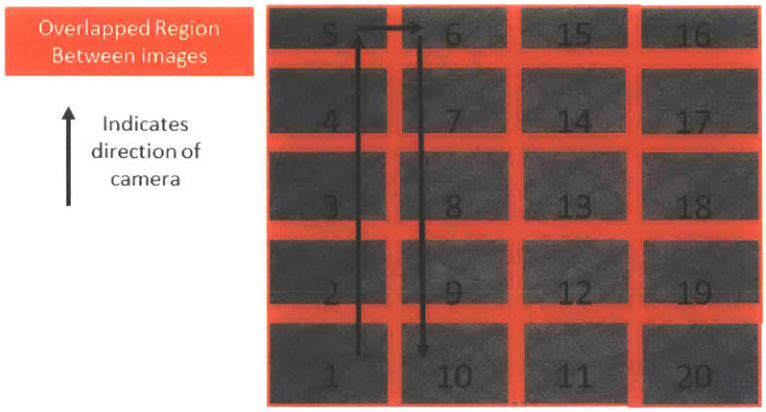

Figure 7: Camera Motion during Experimentation: The head of the Quick Vision Active system moves along the direction of the arrows towards increasing number of image frames, as indicated in the figure. The thick red borders indicate the amount of overlap between the frames. There are 20 images acquired in a 1 in^2 area on the skin.

2.1.2 Sample Images Analyzed

After acquiring the skin image, we seek to extract the microrelief structure. Figure 8 provides a sample image after processing. A Difference of Gaussians technique (DoG) binarizes the image by enhancing the contrast in the grayscale image [50]. DoG enhances features by subtracting a blurred version of the original image from a high contrast version of the original image to reduce random noise and high frequency detail. These different versions of the image are obtained by applying Gaussian kernels with different standard deviations to the entire image. Pseudo code is provided below. Note that while DoG is a powerful technique to enhance feature contrast, it also reduces overall image contrast, so we must be careful in using this technique.

Outline for applying the DoG technique to skin images:

1. Apply a Gaussian filter with standard deviation, σ_1, to obtain the high contrast image: a small standard deviation is used to smooth the image and get the high contrast version (here we use $\sigma_1 = 5$, a little less than the width of the microrelief)
2. Apply a Gaussian filter with standard deviation, σ_2, to obtain the blurred image: a larger standard deviation is used to blur the image, usually $\sigma_2 > 5\sigma_1$ (here we use $\sigma_2 = 30$. After experimenting with different σ_2's, we found this 6-fold increase provides the optimum skin feature enhancement, while preserving much of the contrast in the original skin images)
3. Subtract the blurred image from the high contrast image

After applying the DoG technique to the images, the skin microrelief is much more enhanced as shown in Figure 8. The blue lines are the extracted ridges of the thicker microrelief lines, which correspond to the primary lines shown earlier in Figure 6. These primary lines have a prominent angular direction, which corresponds to the primary direction of the underlying muscular tension and collagen fiber formation along the length of the arm as described in Section 1.2.1.

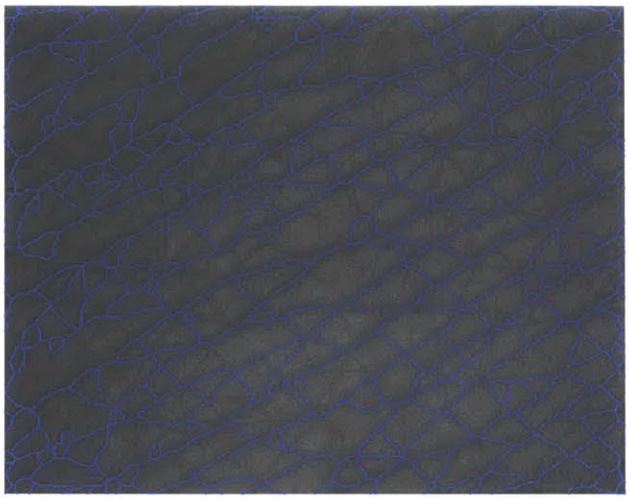

Figure 8: Extracting the Microrelief Pattern: The blue lines are the ridges of the microrelief extracted during image processing. The primary lines are especially prominent. This particular image was provided by a collaborator, Judy Beaudoin.

2.1.3 Challenges of the Microscope

Despite the high-resolution images captured, the Quick Vision Active 220 system has its drawbacks from both the technical and usability perspectives. With a high degree of automation, manipulating image settings through the commercial product is difficult even if the images are not optimal for our application of monitoring large area skin patches over time. A closer look at Figure 6 shows the edges of the image appear darker than the center (darker gray around the outer edges of the image compared to the more white center part of the image); this illustrates the difficulty of obtaining uniform lighting on a 3D human surface and presents a problem during later image processing. The darker edges have poorer contrast of the microrelief ridges against the skin. This makes it difficult to find the matching skin structure between images, since the image edges are used for overlapping and image stitching to get the large area skin patch. Additionally, the small physical region of interest makes image acquisition and processing computationally expensive since we have to process nearly 20 photos to cover 1 in^2 (6.45 cm^2) (compared to imaging a larger ROI at onset). Without sufficient overlap (which is error prone since amount of overlap is manually determined), image stitching of the large area also fails.

From the usability perspective, this microscope is not a viable solution for integration into clinics. Firstly, the device lacks ergonomics, making the long scan times very uncomfortable for

the subjects, as they must keep their bodies in a contorted position in order to keep the wrist normal to the camera. The custom designed armrest with the foam and contouring provides some relief and helps the ergonomics of the system, but the body is still twisted uncomfortably to keep the forearm orthogonal to the camera and body. It is also difficult for the patient to sit completely still for more than two minutes; the images become blurry if the patient twitches after the camera autofocuses the ROI. If the patient slightly shifts in their seat, attempting to keep the arm in place, there are still millimeter disturbances that prevent the later stitching process (i.e. the arm moved enough so that the micrometer level features cannot be matched between two consecutive images). Additionally, given the geometry of the microscope and small scan region, the microscope does not allow imaging other parts of the body (i.e. only forearm imaging is possible). Finally, because it is excessively large (weighing 265lbs) and costly (upwards of $20,000), the Quick Vision Active 220 system is not portable and has little use in the clinics. Clinicians are reluctant to pay for such costly and bulky devices without significant improvements over existing technology. Thus, we develop a custom imaging system as described next.

2.2 Handheld Skin Imaging Device Design

The handheld device consists of three critical components: (1) a camera with appropriate resolution, (2) a light source for uniform lighting, and (3) a housing fixture to provide appropriate working distances and focal depths. Each of these components must be appropriately selected or designed, as described in the subsequent sections.

2.2.1 Camera and Lens

A camera that has sufficient resolution to resolve the various skin features is required; mainly, we are interested in the camera sensor and lens resolutions. A number of potential subjects were imaged with various cameras; these initial experiments showed the minimum camera resolution to resolve the microrelief features on the wrist should be at least 1.3MP [16].

The camera must also have a manually adjustable focus lens to better estimate the focal length compared to an auto-focusing lens [51]. Lowering the degree of automation can help overcome some of the challenges seen in Section 2.1.3. For easy transitioning of the system between clinical and research settings, a common interface (like USB) is desired. A Basler color camera (model acA2040-90uc) is selected. Some key features are highlighted below:

- Camera resolution is 4 MP (more than 2x the desired resolution): image size = 2040 pixels x 2046 pixels; pixel resolution: 5.5μm x 5.5μm
- Simple, lightweight USB to micro-USB connection cable
- Small size compared to other scientific cameras: 29.3mm x 29mm x 29mm
- "DirectShow" compatible for use with LabVIEW's Vision Acquisition Module for image acquisition [52]

Simultaneously with camera selection comes lens selection. Magnification lenses of 1x, 1.5x, and 2x are considered since higher objectives give exceptionally distorted images with only a small focused region due to the lens geometry. Higher magnification lenses see a smaller ROI since the ROI is closer to the optical axis. If the ROI on the object is bigger than the image area (i.e. the wrist is a small part of the larger arm), the lens maps the wide object onto a finite image area, creating "barrel distortion" [53]. Barrel distortion makes it seem like the image is mapped around a barrel, instead of staying on the same plane. This is problematic for skin imaging since small patches of the skin (order of mm^2) are considered planar, but the high magnification lenses would make the mm^2 sections of the wrist look like little spheres.

In selecting the appropriate lens, the trade-off between image size and resolution is considered. Primary and secondary lines of the microrelief and hair have the same width under a 1x lens, but the 1x magnification provides a larger image area (i.e. larger field of view (FOV)). Imaging with the 1x and 1.5x lenses give the same ridge thickness for the microrelief, so we select the cheaper 1x lens for same image quality (i.e. microreliefs look the same with 1x and 1.5x lenses). Primary lines are more prominent under a 2x magnification, but the images acquired with the 2x lens have a smaller FOV and lower contrast between the microrelief ridges and surrounding skin. All these tradeoffs and experiments lead us to select a 1x C-Mount Mitutoyo lens from Computar (model M1620-MPW2).

2.2.1.1 Optical Parameters

Properly imaging the skin microrelief structure requires knowledge of a variety of optical parameters: field of view, working distance, and depth of field. Each is defined below.

***"Field of View" (FOV)*:** the viewable area of object under inspection (fills the sensor). In the setup, the FOV covers the scan region (i.e. the wrist). Across subjects, the square region (FOV)

varies in the range 38mm – 80mm [51]. We use this range as a benchmark for designing the camera-lens system. In the final imaging configuration, the FOV is 53mm x 53mm.

"Working Distance" (WD): the distance from the front of the lens to the object (i.e. the skin surface) at which skin features can still be resolved. For a particular clinical application where the camera is mounted to an ultrasound probe, the WD must be at least 50mm to prevent the camera interfering with the ultrasound gel on the ROI [51]. The WD cannot be so big that it cannot be accommodated on a handheld device (empirically determined to be no more than 305mm). Experimentally, using the Basler acA2040-90uc camera and M1620-MPW2 Computar lens, the WD to resolve the microreliefs on the wrist is 68mm.

"Depth of Field" (DoF): the amount an object can move while still maintaining focus. This is dependent on how much the scan region (i.e. forearm) rotates and the patient's ability to stay still. The forearm has a smaller diameter and therefore may rotate more than a region with larger diameter (i.e. the bicep). Imaging a variety of subjects and asking them to keep their arm in the same position, we find the arm rotates maximum 10° involuntarily. This corresponds to a DoF range of 5.5mm – 32mm, which is calculated based on simple geometry (Figure 9).

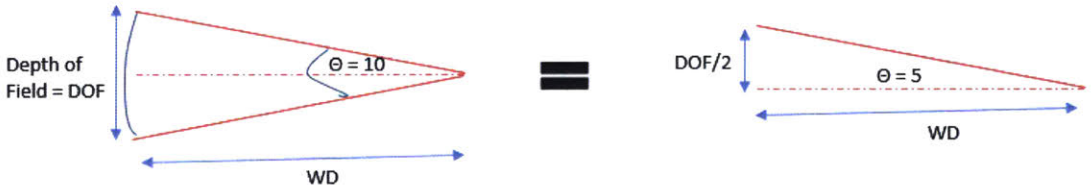

Figure 9: Geometry to Calculate Depth of Field (DoF): This geometry assumes a 10° maximum rotation of the image region (i.e. the forearm). The WD and its relationship to the DoF is also shown in this figure.

"Resolution": the minimum feature size that can be distinguished by the camera. With the 4MP acA2040-90uc Basler camera and the M1620-MPW2 1x Computar lens rated for a 5MP camera, the pixel resolution is found to be 26.6µm/pixel. Expressed differently, the camera lens system has a 955 pixels per inch (PPI) resolution, almost double the accepted FBI standard of 500 PPI for fingerprint imaging [17]. Approximately 2 – 4 pixels span the width of the smallest microreliefs captured across the wrists of 20 subjects in their 20s. The average ridge thickness is 108µm with the plateaus averaging 0.34mm^2.

2.2.2 Lighting

Ambient lighting greatly influences image quality and the ability to resolve skin features. Examples of ambient light include sunlight, fluorescent lights, and white lights in a room. However, to be a more robust system, the quality of the images should not depend on ambient lighting conditions. Therefore, a dominant, controlled light source is preferred to both enhance the skin features and reduce impacts of ambient lighting.

An Edmund Optics (Barrington, NJ) DC white high intensity ring light (model 88-484) with adjustable brightness from Advanced Illumination (Rochester, VT) is selected. The irradiances at a WD of 75mm are: 4.1mW/cm^2 (white), 3.0mW/cm^2 (blue), and 2.7mW/cm^2 (red). A ring light is superior to a confocal light when the scan region is not flat to provide more uniform lighting throughout the scan region; ring lights are often used in clinical applications, and hence used in the handheld device design [54].

2.2.2.1 Lighting Calibration

It is important to make sure the lighting does not cause oversaturation or under-saturation of the imaged area for later image processing since this will affect the number of feature points being detected. Feature points are the unique points that are extracted from the image and used for matching/monitoring over time; they can be found on areas of high contrast (i.e. microrelief ridges) or have different characteristics as described in Section 2.4. Oversaturation can lead to spurious feature points being detected (i.e. points selected from artifacts due to excess reflections rather than from the skin features themselves). Under-saturation can lead to missing feature points (i.e. skin feature points not detected because the lighting is too low).

For testing, a color card QP101 (B&H Foto & Electronics Corp, NY) is used. To obtain the spatial color distribution and avoid fidelity loss of tracked features, a histogram is plotted in real time. This is to ensure that the combined mean and standard deviation is not over 255 (i.e. images are not oversaturated) nor less than 0 (i.e. images are not under-saturated). For low light settings, the results are found in Table 4. With the appropriate intensity and exposure settings, the images are neither oversaturated nor under-saturated [55].

Table 4: Results of Light Calibration Using Color Card QP101

Target	Mean ($\bar{x}$)	Standard Deviation (σ)	Oversaturation? $\bar{x} + 3\sigma > 255$?	Under-saturation? $\bar{x} - 3\sigma < 0$?
Black	52.65	5.45	No	No
Gray	99.93	3.15	No	No
White	154.53	1.93	No	No

2.2.2.2 Light Invariance

An alternate method to ensure that lighting does not affect image quality is by finding the "true color" of the image [56]. This is accomplished by a technique known as "White Balancing." The white color card QP101 is used as a reference white. All pixels in the image are multiplied by the ratio of what is seen as white by the reference white pixel value. Note that the white pixel value may not be 255 since the white pixel value is dependent on the lighting conditions as shown in Table 4 (the mean for the white target was not 255). For poor lighting conditions, this is a powerful technique as the true color emerges once the images are white balanced as shown in Figure 10. Effectively, the system is light invariant as long as a reference white is always provided.

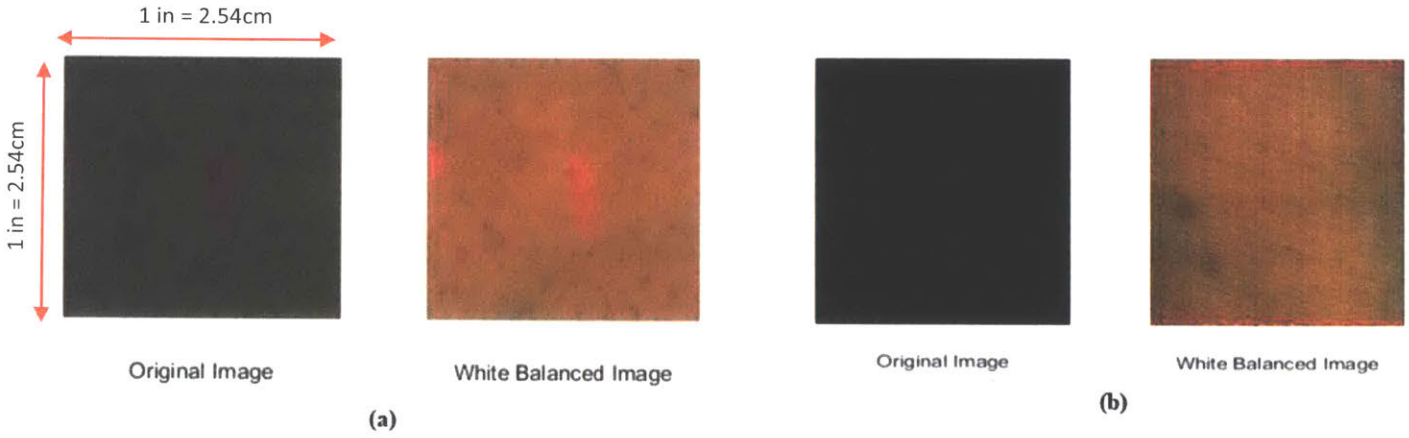

Figure 10: Effects of White Balancing in (a) Nominal lighting conditions and **(b)** Poor lighting conditions

2.2.3 Housing Fixture

The purpose of designing a handheld scanning mechanism which incorporates the camera and light source is to permit control of the parameters that influence image quality. Designing for clinical applications has an additional set of requirements, which were outlined in Table 3. To satisfy these

requirements, a camera mount was designed and 3D printed with ABS plastic on the Stratasys uPrint SE (0.01in resolution) (Stratasys, MN). The final device is shown in Figure 11 and Table 5 summarizes how various features of the device satisfy the design requirements.

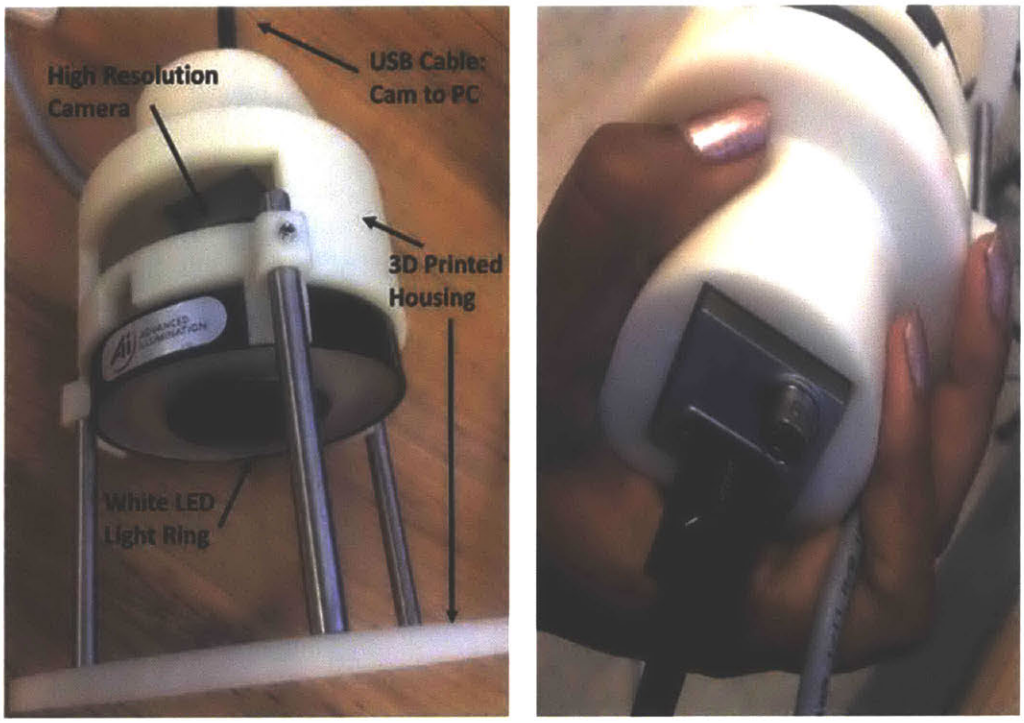

Figure 11: Custom Designed and Fabricated Camera Mount: **(a)** Mount with high resolution camera, frame, and LED light ring **(b)** Ergonomic hold and USB to micro-USB connector cable (for a "plug-and-play" system)

Table 5: How Custom Designed Device Satisfies Design Requirements

Requirement	Primary/Secondary?	How Met?
The system can image skin features on the body.	Primary	FOV is 53mm x 53mm to image the microreliefs on the body
The system allows image parameters to be varied.	Primary	Slot cuts to adjust the exposure and optical zoom in real time. Adjustable WD by connecting ring stand to the frame by stiff, opto-mechanical rods.
The system provides high quality images.	Primary	Resolution of camera is 26.6 μm/pixel
The system can take repeatable images.	Primary	Repeatable scans are achieved by (1) framing the scan region with the ring stand, (2) the experimental procedure, and (3) the device construction forcing the lens to be perpendicular to the scan region so that the scan region is always in focus.
The system prevents deformation of the skin surface.	Primary	Ring stand that provides an even surface and distribution of forces when the device is pressed against the skin.
The system is easy to use.	Secondary	Simple USB to micro-USB connection cable and a custom designed LabView user interface
The system can be used anywhere and at any time of day.	Secondary	The system is light invariant with (1) a dominant ring light source that is calibrated to prevent saturation, (2) a reflective polymer lining that traps the emitted light and reflects ambient lighting, and (3) white balancing the images before processing as discussed in Section 2.2.2.2.
The system is lightweight.	Secondary	Handheld device weighs 412 g
The system is ergonomic.	Secondary	Easy-to-hold system for operator Ring stand for patient
The system is cost – effective.	Secondary	Total cost of the device is $2300
The system is portable.	Secondary	Handheld device measures 14cm in length with a 10.5cm diameter front ring; the back is nearly half as large with a diameter of 5cm. It can image multiple body parts, which allows for integration into the clinics.

2.3 Experimental Procedure

A well designed experimental procedure and workflow is critical for repeatable image capture. The scanning device geometry and structure allow for little variation in how the images can be taken; the ring stand must always be flush against the skin surface to allow the lens to be perpendicular to the scan region before capturing an image (Figure 12a). Subjects have freedom during the scan, which introduces large variability in the data collection and affects repeatability. However, these effects are minimized by asking subjects to place their forearm on a hard surface in a way that is comfortable for them. It is expected that these comfortable positions will vary only slightly from one day to the next.

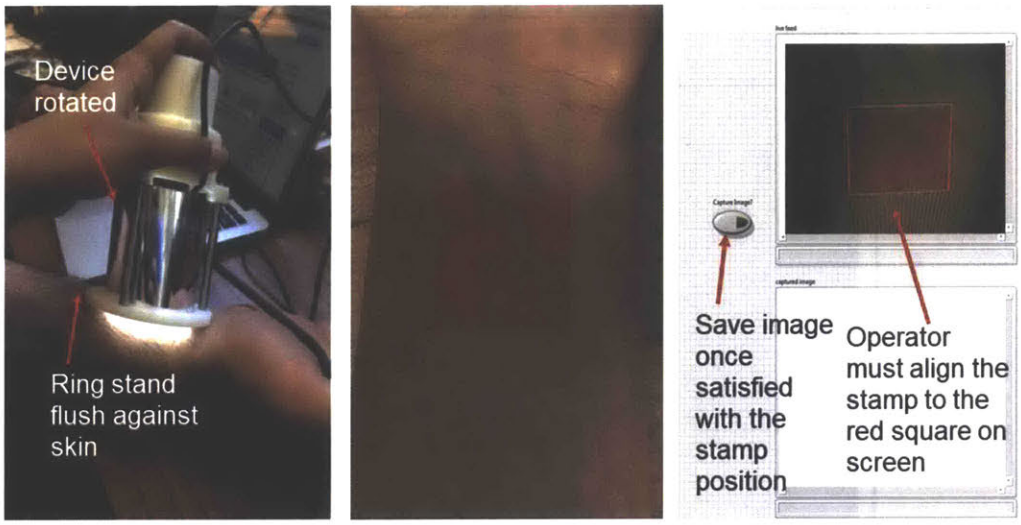

Figure 12: Skin Scanning Experimental Setup: **(a)** Subject places arm in a comfortable position on top of a solid surface. The device is rotated and aligned with the scan region, such that the lens is perpendicular to the skin surface and the ring is flush against the skin surface. **(b)** Red square stamp used for alignment purposes and to enhance the micorelief structure. **(c)** Custom designed user interface with LabView where the operator aligns the stamp with the on-screen red square before taking an image.

Once a comfortable position is found, a red square is stamped on the planar underside of the subject's wrist (Figure 12b). Marking the subject's wrist serves two purposes: (1) to enhance the microrelief structure (Figure 13) and (2) for alignment purposes during image capture and future processing. After experimenting with temporary tattoos (i.e. patterns printed on cardboard, paper,

and transparencies) and body-adhesives (i.e. body glue and ultrasound gel as a binding agent), we determined marking directly on the body would be better for image processing. The tattoos would move during the scanning procedure as the device scanned over the arm, so the features we used for tracking (the tattoo) were not in a consistent position between frames, making image processing difficult. Therefore, we needed features that could be tracked directly from the body and would not move during scanning (i.e. mark directly on the body). Food color and washable markers were considered, but for a cleaner setup, we settled on using hypoallergenic, commercially available body stamps. The red color of the stamp was selected after experimenting with other pigments; red is the most prominent pigment that enhances the microrelief features and has least reflection of the light source [16].

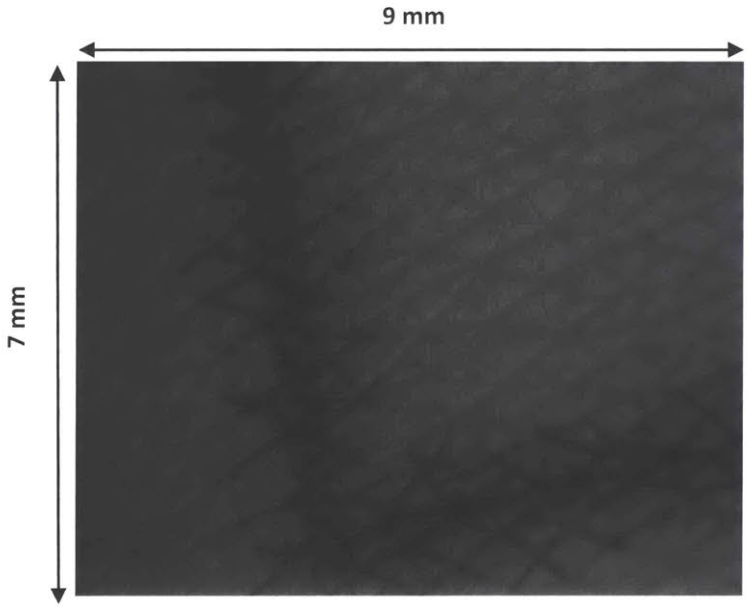

Figure 13: Enhancing Microrelief Structure with Ink: The stamp ink bleeds into the microrelief ridges, which enhances the contrast between the ridges and plateaus. This is contrasted with the other area of the skin surface (no ink), which has less of a contrast.

This stamp serves as an alignment mechanism, since the operator must align the stamp with the red square on the real time streaming display in LabView before taking an image (Figure 12c). Additionally, the corners of the stamp aid in later image processing to detect intersection features points (known as "junction points" described later). Note that the stamp was initially used to develop the matching algorithms, but was later excluded from experimentation since marking the skin is impractical for long-term monitoring and is not a viable solution in the clinics. Without the stamp, the computer contrived features are used for matching processes as detailed in Section 2.4.

2.3.1 Long Term Monitoring of the Skin

For long-term monitoring of the skin, we choose to study a region of skin that is easily accessible and has minimal distortion. As discussed above, we use the underside of the wrist for one patch of skin. The other patch of skin is further up in the forearm (closer to the elbow) where the arm is roughly planar. For lean arms, the location of the second skin patch is not as critical as with more muscular arms, where the pressure from the mounting surface can spread the tissue and distort the skin. Across subjects whose forearms are 7in – 10in long, the second skin patch is around 2in – 3in from the elbow crease, which is measured as shown in Figure 14.

Figure 14: Skin Patch Imaged for Long Term Monitoring: The part of the forearm that is roughly planar and has minimal distortion is used as a second monitoring point on the forearm (the first monitoring point is on the wrist). Across subjects with forearm lengths of 7in – 10in, this area tends to be 2in – 3in from the elbow crease.

A variety of subjects are imaged to better understand the microrelief structure variation (see the distribution of males and females in Table 6). The IRB approved study had 30 subjects ranging from 4 years to 45 years of age; 16 of the subjects were long-term (imaged over multiple days and months; 1 subject was imaged over 1.5 years). Subjects had varying skin complexions, pigment variations, moles, and other melanin variations. Some subjects had common skin conditions, such as keratosis pilaris, a common disease that enlarges the hair follicles, and psoriasis, where the skin cells build up and cause dry, itchy skin patches [57], [58].

More commonly, subjects had hair of varying thicknesses, densities, and color (i.e. men have thicker, denser hair compared to women, whose forearm hair is much finer). This presents an imaging challenge since the diameter of the hair often obscures the microrelief structure. Especially challenging are subjects with light colored hair on lighter skin complexions, since the skin and hair are similarly colored and have little contrast in the images; these subjects require some staining mechanism to distinguish the hair from the skin and microrelief. For the hairy subjects, the wrists are imaged multiple times with the hair in various orientations to get the underlying microrelief structure. Additionally, hair segmentation algorithms were developed to artificially remove the hair before registering the skin structure [59]. Figure 15 shows the workflow.

Table 6: Summary of Subject Distribution: The IRB approved study had a variety of subjects ranging in age from 4.5 to 45. Here is a summary of the 16 long-term subjects.

Subject ID	Gender	Age (years)
1	Female	23
2	Female	23
3	Female	23
4	Female	4.5
5	Female	22
6	Female	26
7	Female	24
8	Female	23
9	Male	22
10	Male	44
11	Male	7.5
12	Male	25
13	Male	26
14	Male	22
15	Male	22
16	Male	27

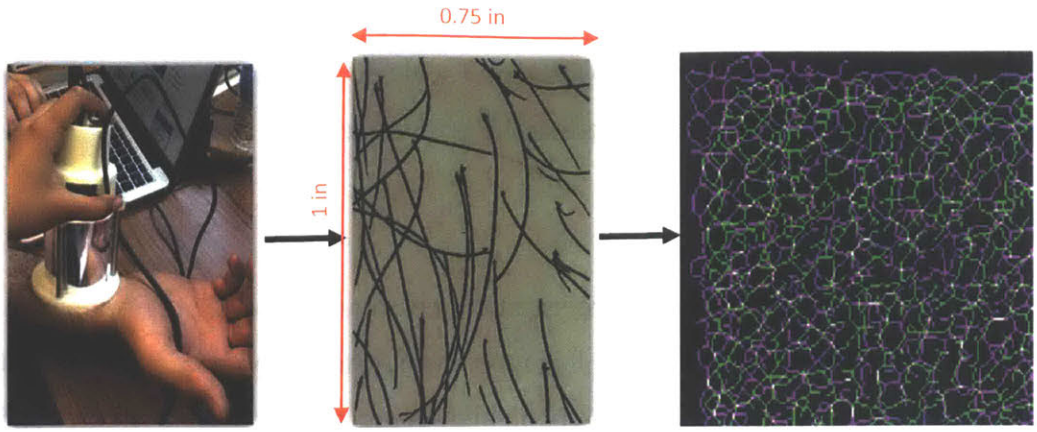

Figure 15: Skin Scanning Workflow: **(a)** Image acquisition with custom built handheld device **(b)** Hair detection and algorithmic removal **(c)** Image registration and matching: the purple and green networks are the computer contrived feature points that are detected from the pre-processed skin images of the same skin image at two instances of time. These features are what the computer determines are the intersection points (i.e. junction points) of the microreliefs. The white points are the matched feature points between the two networks obtained on different days.

To better understand the long-term stability of the skin structure, the same skin patch is imaged at several time intervals – same day (after a couple hours), couple days apart, couple weeks apart, couple months apart, and even 1.5 years apart. The younger subjects must be imaged over shorter time intervals (ideally, every couple of weeks) given their arm lengths grow quickly and registration is more challenging. For adult subjects, the images are taken anywhere between same day and 18 months later depending on subject availability. Samples of the registered images are found in Section 2.5.

2.3.2 Large Area Skin Patch

To get the large area skin patch, multiple images of the body part with overlapping areas are required as with the Mitutoyo Vision System. Since the FOV on the handheld device is larger, we are able to generate a stitch of the entire forearm with only 7 – 10 images per individual, depending on the forearm length. Again, the amount of overlap is manually determined, but the images now span 7in – 10in of the human body compared to the 1in by the Mitutoyo system. To have overlapping microrelief features between images, approximately ½ the image (0.5in, 1.27cm) is overlapped. This larger overlap region ensures there will be enough features detected from the skin structure that two consecutive images can be matched even with the coarser resolution of the

handheld device compared to the Mitutoyo system. The device is translated from the wrist to the elbow while monitoring the live feed on the LabVIEW interface.

2.4 Methodology[a]

As described in Section 1.2.3, deformable registration techniques have been developed to analyze and match the fingerprints and palm prints for biometric identification purposes [17], [60]. Most of these deformable registration techniques rely on high-contrast, macro-scale features and assume almost no skin stretching [17], [60]. However, the skin surface on the rest of the body (microrelief) has much lower contrast features (compared to the fingerprints) and noticeably stretches when strained. Thus, existing deformable registration techniques are not robust enough to be applied to the low contrast boundaries of the deformable and non-planar skin surface, so any solutions obtained by existing deformable registration algorithms tend to be far from the true solution.

An alternate approach is using homographies for rigid skin registration (SIFT keypoint matching method), which identifies a sparse set of landmarks between two images and aligns the images through a homography transformation [61]. Lowe's method performs the homography in three steps. First, keypoints are detected from each image after filtering and processing the original image (i.e. Laplacian of Gaussian) [61], [62]; these keypoints tend to be on edges of features or other areas of high contrast. Second, an affine-invariant local descriptor around each keypoint is computed using (i.e. shape context) [11]. Lastly, the correspondence between keypoints and correct global transformation is found by employing different variants of random sample consensus (RANSAC) to determine if the transformation is correct [6]. However, this rigid registration technique also requires high contrast patterns to extract salient features.

Inspired by existing fingerprint analysis, which rely on macro features, we develop algorithms to computationally analyze the skin based on microrelief features at the micrometer scale ([17]). The developed algorithms consist of two parts: (1) a global transformation that corrects for large-scale skin stretching and different viewpoints by using SIFT feature points [61], and (2) a local transformation which corrects for deformation due to body curvature and other nonlinearities using Voronoi segmentation [63]. Both are summarized below.

---

[a] This work is in collaboration with Professor Xian Du at UMass Amherst

2.4.1 Registration and Matching Overview

Mathematically, the registration of skin microrelief structures is formulated as an optimization problem to map junction points $x \in \mathbb{R}^2$ in a source image, I_B, to points $x' \in \mathbb{R}^2$ in the target image, I_A, with the cost function $C(\cdot)$ being minimized with respect to a transformation, $\mathbf{T}(x)$ [64].

Equation 1: Cost Function Minimized with respect to a Transformation

$$\underset{\mathbf{T}(x)}{\operatorname{argmin}} C(\mathbf{T}(x); x, x')$$

Here $\mathbf{T}(x)$ is the transformation: $\mathbf{T}: x \mapsto x'$. The minimization is solved in two steps: First, to account for differing viewpoints in a scene and large-scale skin stretching, a global transformation, $\mathbf{T}_{\text{global}}$, is applied. Second, to tackle deformation of the skin due to surface curvature and other nonlinearities, a local transformation, $\mathbf{T}_{\text{local}}$, is applied. Hence, the combined transformation is: $\mathbf{T}(x) = \mathbf{T}_{\text{local}}(\mathbf{T}_{\text{global}}(x))$. We solve $\mathbf{T}_{\text{global}}$ using SIFT key point registration and tackle $\mathbf{T}_{\text{local}}$ using Voronoi-based point-pattern matching (PPM) [23], [61], [63].

Figure 16 shows a flowchart of the registration and matching procedure whose inputs are a target image, I_A, and source image, I_B, and outputs the registered source image, I_B'. The first part of the procedure (illustrated in grey) finds a global transformation by employing the commonly used Lowe's method [19]: first, SIFT key points are detected in I_A and I_B, then RANSAC estimates a homography transformation that warps I_B such that the transformed source image I_B' is "close" (within a certain threshold) to the target image [6], [61]. In the second part (shown in blue), I_A and I_B' are segmented into Voronoi cells centered at the key point locations. Then, junction points are detected in each set of paired Voronoi cells and matched by a neighborhood constrained bipartite matching algorithm. Each of these are further explained below.

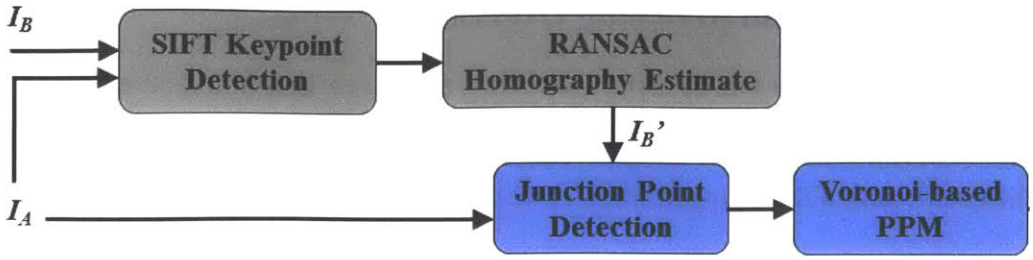

Figure 16: Flowchart of Proposed Algorithm for Skin Registration and Matching: Target image, I_A, and source image, I_B, are inputs to the registration and matching algorithm. The grey blocks are the global transformation, which aligns the images based on differing viewpoints and large-scale skin stretching. The blue blocks are the local transformation which corrects for deformation of the skin due to curvature and other nonlinearities.

2.4.1.1 Keypoint Detection

Reliable landmarks, or keypoints, need to be identified in skin patches based on stable physical features of the skin. For this purpose, SIFT is used as the keypoint detector and feature descriptor, owing to its success in detecting not only skin pigmentation and hair follicle openings, but also the fingerprints in existing literature. Similar to the pigmentation and hair follicle patterns, the skin surface exhibits a unique spatial distribution of physical features (i.e. the microrelief) that allow us to use SIFT keypoints for accurate skin registration. Note that the keypoints are not always physically connected to the microrelief pattern; the keypoints are detected from areas of high contrast and stable illumination [62], [65]. While the keypoints can be connected to the edges of the microrelief, the illumination and imaging parameters may find keypoints on the plateaus, within the ridge, or somewhere on the image completely unrelated to the skin structure. In the future, parameters can be fine-tuned to enable SIFT to be more receptive to detecting actual skin features.

Essentially, SIFT detects the local extrema of multiscale Difference of Gaussian (DoG) of skin images. Because physical skin features are small, micro-scale features relative to the image size, the DOG octaves are limited to the first 2. Since skin images have low contrast, the minimum contrast for the local maxima is set to 0.01 to accept any low contrast point. The threshold to eliminate edge response remains at 10. In a typical skin image, tens of thousands of keypoints are detected throughout the image; in the 1 in^2 red stamped region, nearly 10k SIFT keypoints are detected, of which only a fraction are useful and consistent between a pair of images (Figure 17).

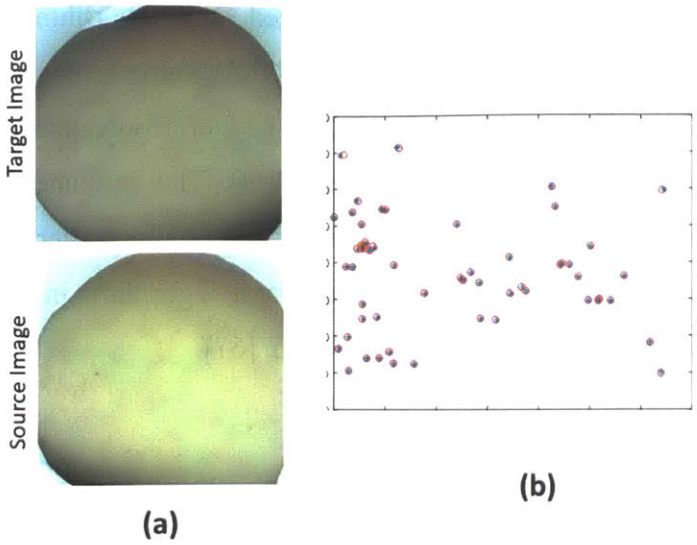

Figure 17: Sample Images and Detected SIFT Keypoints: (a) The target image, I_A, and source image, I_B, taken some time later **(b)** The detected SIFT keypoints that are consistent throughout the image between the target and source images.

2.4.1.2 RANSAC Homography Estimate

We assume that a small enough skin patch (1 in^2 within the thousands of square inches of the human body) can be approximated as a 2D plane. Then we can model the global transformation between keypoints, $\mathbf{T}_{\text{global}}$, as a 3 x 3 invertible homography matrix that transforms between viewpoints in projective space (Equation 2).

Equation 2: Transforming key points to the proper domain

$$s\mathrm{x}' = \mathbf{T}_{\text{global}}x$$

Here $\mathrm{x} = [x\ y\ 1]^T$ and $\mathrm{x}' = [x'\ y'\ 1]^T$ are homogeneous coordinates of a pair of corresponding keypoints, K_A and K_B, in images I_A and I_B, respectively; s is a scale factor. To estimate this transformation, the keypoints are first matched using approximate nearest neighbor (NN) search through a k-d tree on the 128-dimensional SIFT feature space in Euclidean space [61], [66]. For computational efficiency, a bin size of 50 is used. The NN ratio test (NNDR) proposed by Lowe is used to remove false matches between NNs; the NNDR threshold is set at 0.7 [61].

Next, an estimate of the homography is obtained by RANSAC [67]. During each RANSAC iteration, four random pairs of matched points are sampled by Gaussian sampling as inputs for the direct linear transformation (DLT) algorithm [68]. After the RANSAC iterations are complete, an

estimated transformation is found from the normalized DLT algorithm, considering all inlier matched keypoints as the large consensus set. The RANSAC outlier threshold used is four pixels given the size of the microreliefs to ensure that only 1 keypoint is detected per microrelief width (recall: 2 – 4 pixels span the width of the microrelief). The estimated homography and its corresponding inlier matched keypoints are inputs for the nonlinear iterative refinement of the homography parameters using the Levenberg-Marquardt algorithm, in which the sum of the Sampson error of the inliers keypoints is minimized [3], [67].

2.4.2 Skin Point Pattern Matching

Using the inverse of estimated global transformation, $\mathbf{T}_{\text{global}}$, we can warp the source image, I_B, to obtain pixel locations in the final, globally registered image, I_B'. The pixel intensities in I_B' are calculated by bi-cubic interpolation [66]. Figure 18 shows the flowchart of the microrelief structure matching procedure. Note that key points in the domain of I_B are transformed to the domain of I_B' by Equation 2, and are denoted by K_B'. Each step is further described below.

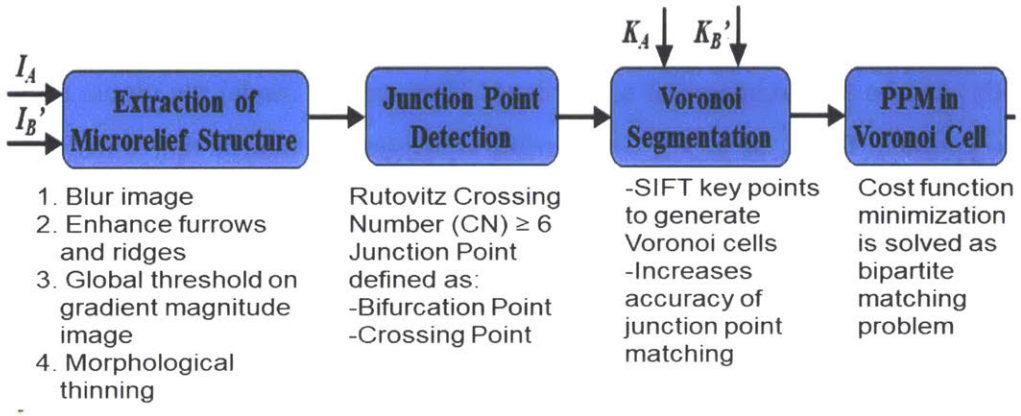

Figure 18: Algorithm Flowchart for the Microrelief Structure Matching Procedure

2.4.2.1 Extraction of Microrelief Structure

The purpose of this stage is to extract the ridges of the microrelief structure from the raw, noisy skin images, I_A and I_B. The following operations are applied on both images. First, background normalization is applied to reduce the gray level variations along ridges and furrows. A 13 × 13 box linear filter is applied iteratively 30 times to approximate a Gaussian blur. The resulting blurred image is subtracted from the original image. Second, the bottom of flat valleys and top of plateaus in the images are enhanced. The local standard deviation is calculated for each pixel, using a 5 × 5 window size. Then, the gradient and magnitude (using central difference) and discrete

Laplacian images are computed from the local standard deviation image. Third, a global threshold, the mean of the gradient magnitude image, is applied to the gradient magnitude image to find pixels that have smaller gradient magnitudes. Fourth, morphological thinning is applied to the binary image achieved in the third step to reduce the valley structures to pixel widths of one pixel. Note our image enhancement method is similar with that in [61], though we do not calculate orientation and frequency in this work.

2.4.2.2 Junction Point Detection

The result of the microrelief extraction is a network that is connected by junction points. Hence, matching skin patches is akin to matching two networks and their nodes. In the same vein as minutiae extraction in fingerprint analysis, the Rutovitz crossing number (CN) is used to extract junction points [17], [69]. At each pixel of the skeleton image, the eight neighbors of the pixel are scanned in a counter clockwise manner. We define "junction points" to be the bifurcation and crossing points of the microrelief edges. If $CN \geq 6$, pixels in the microrelief structure are retained and labeled as junction points.

2.4.2.3 Voronoi-Based Point Pattern Matching (PPM)

Matching more than 10k junction points in the target (I_A) and registered images ($I_{B'}$) is computationally expensive, requires lot of computer memory, and has a high degree of uncertainty. A Voronoi segmentation of images I_A and $I_{B'}$ and further clustering of K_A and $K_{B'}$ by the boundary of Voronoi cells is a better alternative [63]. The SIFT keypoints are used as seeds to generate the Voronoi cells; the junction points are matched within the paired Voronoi cells. This method assumes the skin surface is homogeneous with appropriate transformations, so sets of microrelief junction points in two Voronoi cells can be matched as the same junction points. Under this assumption, Voronoi segmentation and clustering solves the difficult task of finding appropriate borders between the subsets of junction points.

According to the definition of Voronoi diagram, the Voronoi cell for each seed consists of all points closer to this seed than to any others [63]. Voronoi segmentation allows for the proximity preserving constraint to be implemented in the junction point clusters. Given a uniformly stretchable target (such as a skin patch), the points within the Voronoi cell will have minimal changes after SIFT and RANSAC registration. The Voronoi clustering increases the dissimilarity

between junction points that do not belong to the paired group, which increases the accuracy and geometric fidelity of junction point matching.

We formulate the PPM in each Voronoi cell as a standard assignment problem. Let $P = \{ p_i \mid p_i \in \mathbb{R}^2, i = 1, \dots, m\}$ and $Q = \{ q_j \mid q_j \in \mathbb{R}^2, j = 1, \dots, n\}$ denote junction point locations found in a pair of Voronoi cells in images I_A and I_B, respectively. Without loss of generality, assume that $m \leq n$. The dissimilarity between points of p_i and q_j can be measured by a cost, c_{ij}. Then, a cost matrix $\mathrm{C} = (c_{ij})_{\mathrm{m}\times\mathrm{n}}$ denotes all the possible pairing costs between the two junction point sets. To deal with the missing points and outliers in the junction point sets, nonexistent dummy points are introduced in the pairing cost function. The dummy pairing cost is user-specified, denoted by ϵ; it is a constant set larger than the maximum value of the non-dummy pairing costs. Given a neighborhood constraint for each junction point, p_i, we model a one-to-one correspondence problem by assigning any point in P or dummy point to a point in Q such that Equation 3 holds.

Equation 3: Dummy point pairing to help with missing points and outliers in junction point sets

$$\underset{\pi(i)\in \mathrm{N}(i),\pi\in\Pi}{\operatorname{argmin}} \; c_{i,\pi(i)}$$

Here $\mathrm{N}(i)$ denotes the neighborhood of point, p_i. The above cost minimization can be solved as a bipartite matching problem using the $O(n^3)$ Hungarian algorithm [70]. We use shape context (CS) as a feature to calculate the dissimilarity between pairing points for cost [68]. Using only shape context information to evaluate the level of match can be error prone, especially when a large amount of missing points and extra points are present. Other factors, such as order preservation and proximity information, have been shown to effectively improve the matching results [11]. We use a proximity constraint to preserve the neighborhood for local search of correspondence. SIFT keypoint registration guarantees a proper neighborhood descriptor to sufficiently preserve the proximity information and we use K-NN to find the neighborhood in Q for each point, p_i. K values between 3 and 6 are used for matching; the algorithms have not been optimized to find the optimal value of K for best matching. The result of the final step (PPM) is a matching list with three components providing information about the i-th Voronoi cell. The first component is the correspondence index for junction points within the cell. The second component is the junction

point coordinates within the cell of I_A. The third component is the junction point coordinates within the cell of $I_{B'}$. Sample Voronoi-based junction point results are shown in Figure 19 with the correspondences overlaid on the original, raw images provided in Figure 20.

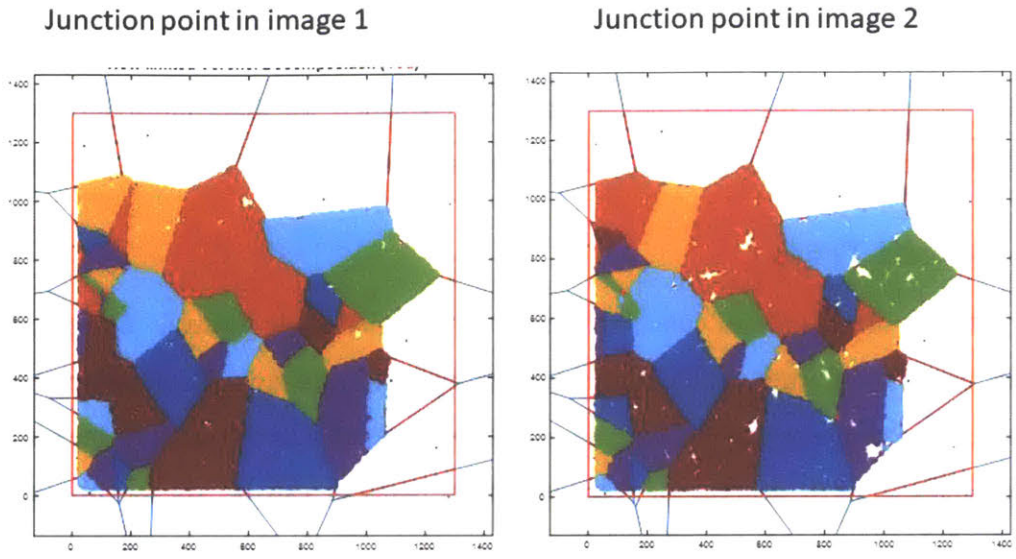

Figure 19: Voronoi-Based Junction Point Matching Results: Each Voronoi cell is constructed around the SIFT keypoints. Junction points within the cell are matched. Corresponding cells have the same shape and are denoted with the same color across a pair of images.

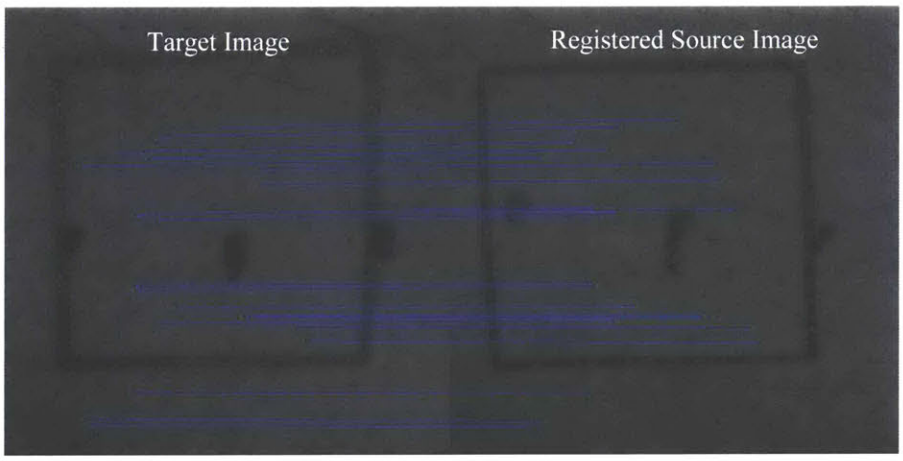

Figure 20: Correspondence Points Overlaid on Raw Images

2.5 Microrelief Results

Before using the algorithms on the experimental images, we need to evaluate the developed algorithms. The registration and matching algorithms are tested and evaluated using MATLAB 2016b on a laptop with Intel Core i5 (4th Gen) 4210M/2.6GHz. To evaluate the accuracy of the matching procedure, the true junction point pattern (ground truth) must be known with which to compare the output. Once the algorithm accuracy is quantified, the algorithms can be used on the experimental images and conclusions made appropriately after. These steps are detailed below.

2.5.1 Ground Truth

Manually labeling thousands of junction points in the microscale features for ground truth is error prone. For ground truth evaluation, three synthetic skin images, I_B, are generated for each target image, I_A. Assuming that the original camera viewpoint is orthogonal to the surface at the center coordinates, the 6 degrees of freedom of the camera can be set to simulate different viewpoints of the image plane using a projective warp. The camera rotation parameters are randomly perturbed up to 10° for the three possible rotation axes (along the plane of the arm, orthogonal to the arm, and along the contour of the arm) to capture the maximum real life rotation of the forearm. Distortion due to camera translation is trivial and arbitrary values are set to keep the red square approximately centered. To simulate a stretching effect of the skin, the image is warped by randomly scaling the x and y coordinates by a factor up to 1.2, which would account for a skin expansion due to gaining weight. These steps simulate global transformation of the image. To simulate local distortion of skin features, random displacements up to 5 pixels are applied to the mesh grid of the image every 15 pixels, which would simulate a stretch of 0.13mm at any one point on the skin, a realistic distortion caused by the friction between the device and ROI during scanning. Finally, Delaunay triangulation and bi-cubic interpolation are used to generate a distorted image.

2.5.2 Evaluation Criteria

Two matching algorithms are used on the synthetic images: (1) our developed registration and NN matching algorithm and (2) existing CS matching algorithm, which serves as the benchmark to compare our custom algorithms.

The accuracy of registration and matching is evaluated based on the root-mean-square error (RMSE), $\mathbf{RMSE} = \sqrt{\frac{1}{N}\sum_{k=1}^{N}\|\hat{y}_k - y_k\|^2}$, where N is the number of matching points, $\hat{y}_k$ is registration and matching result (given in pixels), and y_k is the ground truth. The mean and standard deviation of RMSEs for all matching junction points are calculated. Figure 21a shows that the developed NN matching algorithms are accurate to 1 – 3 pixels (26μm – 80μm), which is more accurate than the existing CS matching methods. Since junction point locations may not always be precisely detected because of the multiple pixels across the ridge of the microrelief, this accuracy of 1 – 3 pixels is acceptable.

The computation efficiency is calculated by $t = 1000n/t_C$, where t_C is the computation time for matching. Figure 21b shows that the NN matching algorithm can reach speeds of about 500 points per second, though it is little slower than the CS matching algorithms. Since all ROIs used for these results have more than 10k junction points, matches are made in less than 50 seconds, which is acceptable as long as the application does not require real-time analysis.

The true junction points can be measured by the ratio $J_{r1} = N/n$ (inverse of missing and extra point ratio) against the ratio $J_{r2} = m/n$ (where m represents the number of points in the target image and n represents the number of points in the registered source image). Figure 21c shows that most of the data is matched using more than 70% of the junction points. This indicates there are 20-30% missing points, which could have occurred during image acquisition or preprocessing. The algorithms are tested across 16 data sets; there are no observable differences in the matching accuracy and computation results among genders or ages.

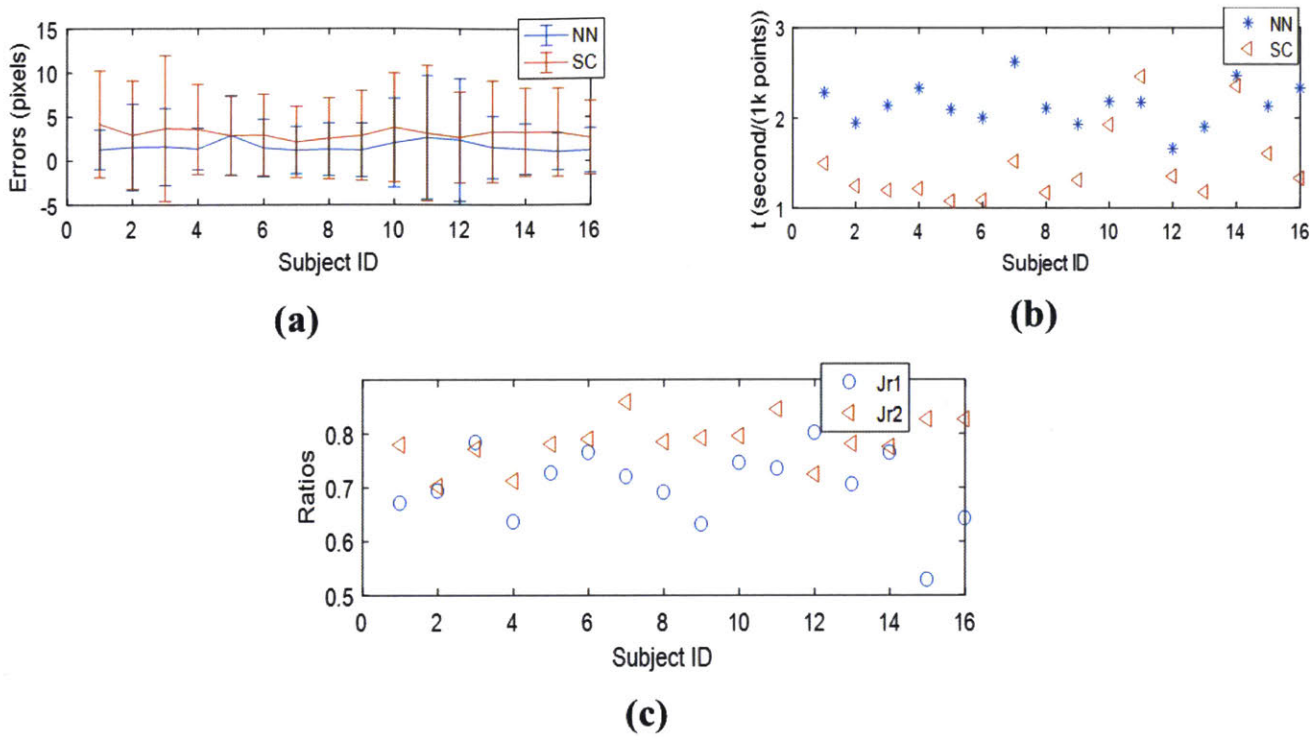

Figure 21: Evaluating the Developed Registration and Matching Algorithms (NN) to Existing Shape Context Matching Algorithms (CS): **(a)** Matching Accuracy – developed NN algorithms are accurate within 1-3 pixels, existing CS algorithms are less accurate (7 – 12 pixel accuracy) **(b)** Computation Time - NN algorithms take approximately 2 seconds to match 1000 junction points; CS algorithms take a little over 1 second for 1000 junction points **(c)** Missing Point Ratios – nearly 70% of the junction points are used for matching between two images, this suggests nearly 20-30% missing points

Figure 22 shows the workflow of the registration and matching processes. Matching of the skin microrelief network is evaluated in two ways: by (1) synthetically distorting the images and evaluating the results against ground truth (described above), and (2) visually evaluating the target and source images (discussed more in Section 2.4). The latter is much easier when there is a permanent feature (i.e. mole, scar, etc.) on the ROI with which to compare the images. Figure 22e shows the skin junction point networks align well based on the developed registration process.

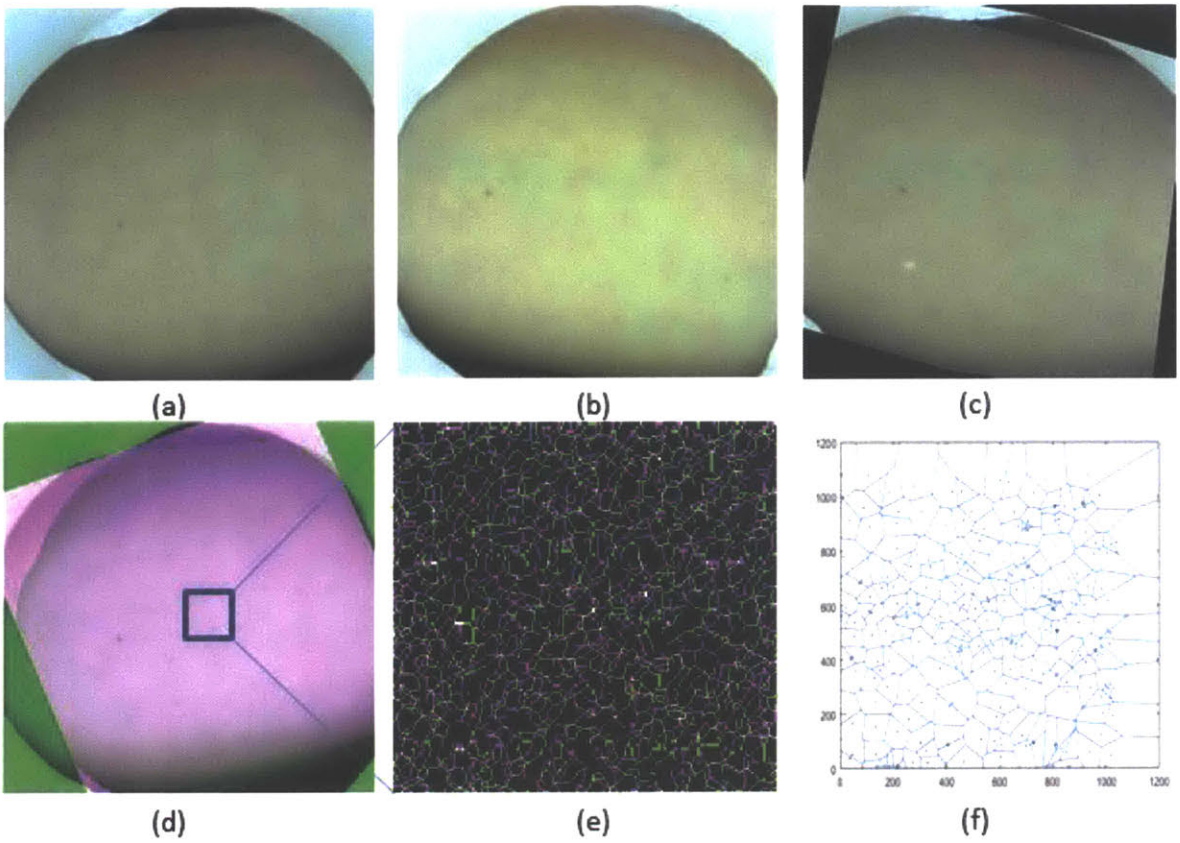

Figure 22: The Registration and Matching Process Illustrated: **a)** Target image, I_A, taken at the initial visit **(b)** Real source image, I_B, taken some time later **(c)** Synthetic source image with rotation and translation, $I_{B'}$, **(d)** Registered target and source images, **(e)** Highlight of registered SIFT keypoint structure, **(f)** Voronoi cells for matching the registered images

2.5.3 Algorithms Used on Experimental Images

Once the registration and matching algorithms are evaluated against ground truth, they are used on the experimental images. There are 16 sets of wrist images, each consisting of a target image (acquired at the first visit) and a source image taken some time later. A variety of subjects are imaged with variations in skin pigmentation, presence of features (i.e. hair and moles), and of differing ages with no degradation of algorithm performance. Sample target, source, and registered images are provided in Figure 23, Figure 24, and Figure 25. The images demonstrate algorithm performance over a diverse set of subjects and imaging conditions (varying viewpoints, different ages, variety of pigmentation, and different features). We notice that the extracted SIFT keypoint structure looks denser for younger subjects as expected (since the primary and secondary lines are more orthogonal at younger ages) and that hair can be distinguished in the network patterns.

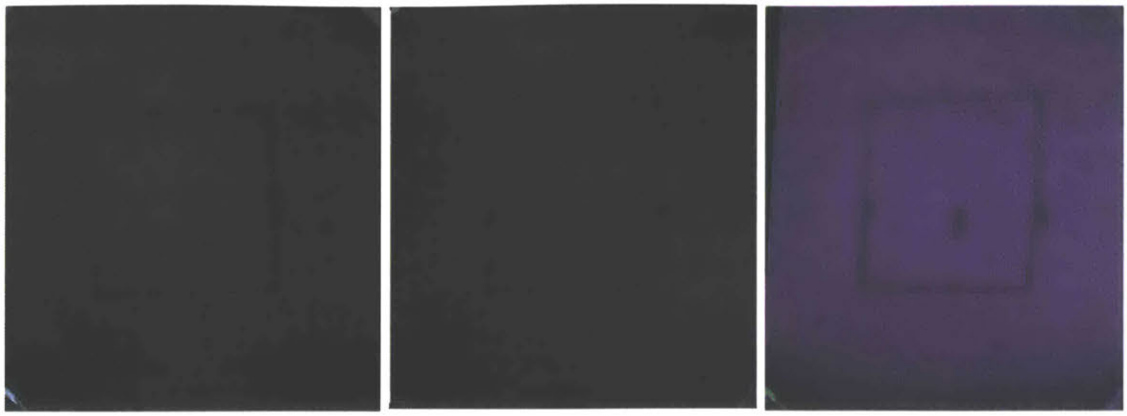

Figure 23: A Sample Set of Experimental Images and Registration Results over Time (1.5 years): **(a)** Target image **(b)** Source image acquired after 18 months **(c)** Registered target and source images overlaid; ROI in red rectangle is used for matching

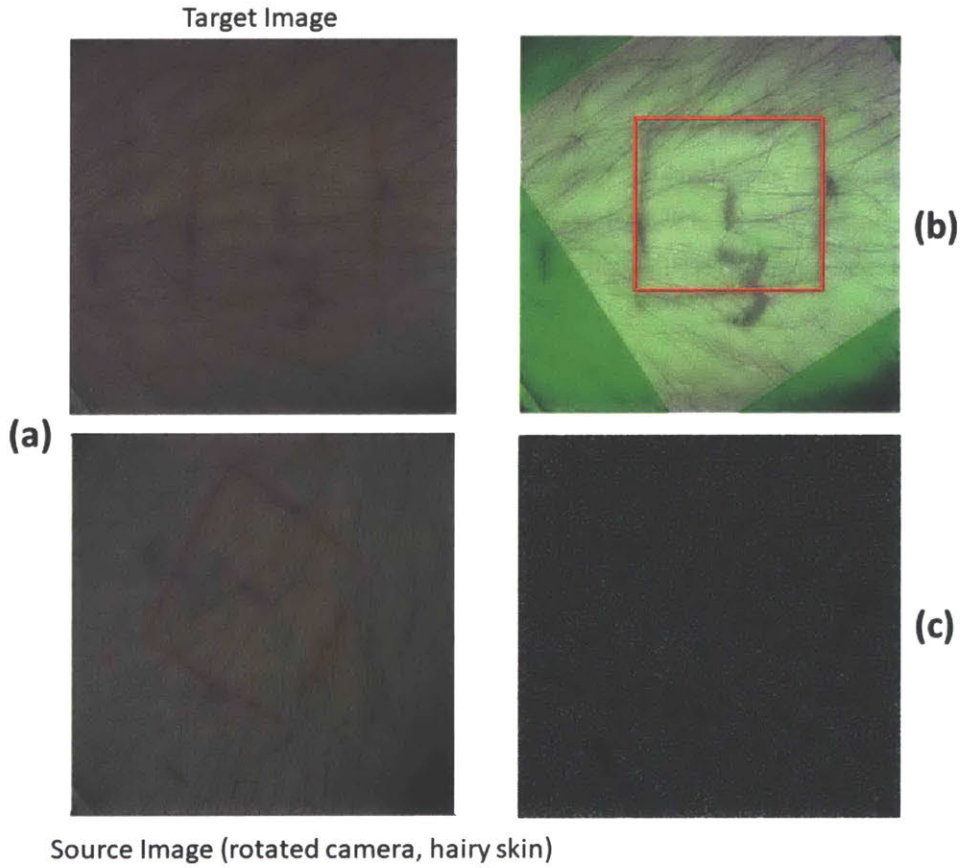

Figure 24: A Sample Set of Experimental Images and Registration Results on Subjects with Hair: (a) The target and source images of a ROI with hair. The camera is also rotated, significantly altering the viewpoint. **(b)** The registered target and source images overlaid; the red rectangle is the region used for matching. **(c)** A close-up view of

the SIFT keypoint patterns of the target and source images where the hair is clearly discernible. The green points are the SIFT network from the target image, pink points are the SIFT network from the source image, and the white points illustrate the overlapping locations between the target and source images.

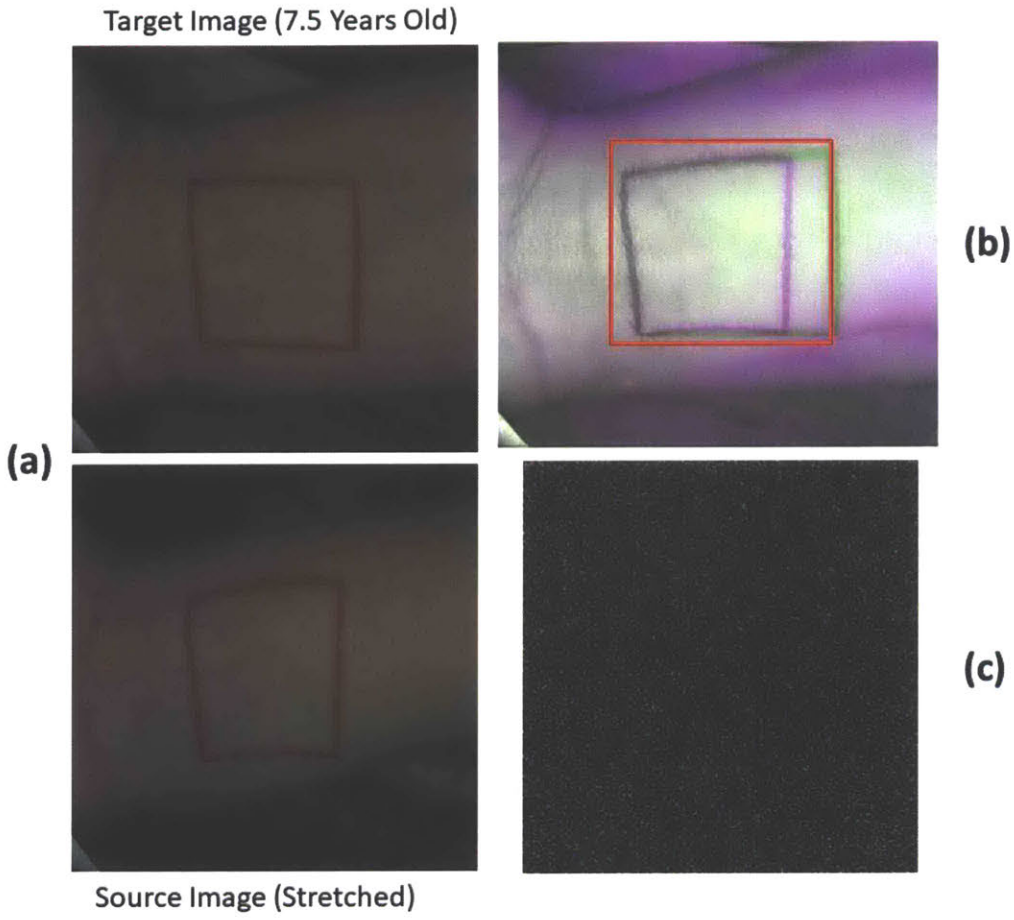

Figure 25: A Sample Set of Experimental Images and Registration Results on a Young Subject: : (a) The target and source images of a ROI on a child. The ROI is stretched to significantly alter the viewpoint. **(b)** The registered target and source images overlaid; the red rectangle is the region used for matching. **(c)** A close-up view of the SIFT keypoint patterns of the target and source images. The green points are the SIFT network from the target image, pink points are the SIFT network from the source image, and the white points illustrate the overlapping locations between the target and source images. The SIFT keypoint network appears much denser than in other subjects (primary and secondary lines clearly distinguishable).

2.6 Summary of Microrelief Work

A custom-designed handheld imaging device was fabricated as a low-cost, lightweight, ergonomic solution to image the skin surface texture, the "microrelief." This device enables studying the long-term stability of the skin, especially in healthy individuals over time, a clinical area that has not yet been explored. The high resolution of the device is comparable to state-of-the-art fingerprint technology and satisfies clinicians' needs with its portable size and ease-of-use, allowing for seamless integration in clinics. For long term skin monitoring, repeatable image capture is possible with the design of experiments and real time LabView image capture. The developed system is benchmarked against comparable state-of-the-art technology, the PRIMOS system (Table 7). PRIMOS lite is a handheld, skin measuring system that provides high resolution images of the skin, specifically for measuring crow's feet (wrinkles around the eyes) [71]. Other versions of the PRIMOS technology are not handheld, but can provide high resolution images of the skin texture on other parts of the body.

Table 7: Handheld System Benchmarked Against Comparable Technology

System	Sensor Size	FOV	Cost	Weight
PRIMOS	32 cm x 31 cm	0.94" x 0.55"	$20,000	4000 g
Handheld System	1.12 cm x 1.13cm	1.58" x 1.77"	$2500	412 g

Non-rigid registration and matching algorithms were developed to study the stability of the skin junction point features without necessitating use of physical markers on the human skin. The algorithm functionality was found to be comparable to existing shape context matching algorithms.

We found that the computer contrived features can be matched after 1.5 years. Since these features are extracted from the skin images we provide to the algorithm, it suggests the skin structure is also stable over a period of 1.5 years. If this is true, the microrelief structure can be used as a mapping system for the body; in other words, a position on the body can be found by looking at the skin structure, which could change the future of the medical profession. For example, during post-operative care, the surgeon will only have to look at the skin from where they took a tumor sample rather than having to perform costly imaging procedures (i.e. ultrasounds) to find

the exact location. Additionally, changes in the microrelief structure could indicate a skin or other health condition; thus, observing the microrelief over time can aid non-invasive diagnostics.

2.6.1 Potential Design Changes

The handheld device is modular, allowing changes to aspects of the design for robust imaging as described in Section 2.2. Current configuration of the device allows imaging flatter areas of the body (i.e. exposed limbs, the back, and torso); for more curved regions, the ring stand shape can be modified to keep the camera normal to the ROI. To make the device more robust and individualized, a spring-loaded ring stand could be designed to contour different arm sizes. This would help maintain the camera orthogonal to the ROI. Imaging the head would require a more pliable ring stand for scalp comfort, which could be achieved by changing the manufacturing material or covering the stand with foam to ensure correct camera configuration in a continuously curving region.

Imaging the microrelief structure in other parts of the body may require modifying the WD, which is easily done with the adjustable opto-mechanical rods, since the microrelief size varies depending on body location. A linear polarizer may help to enhance the harder to see microrelief structure by filtering out backscattered component reflected from the skin tissue and only keep the surface texture information [72]. However, doing so would require directional lighting to image the polarized light and regular reflectance from the skin surface, which is uncommon in clinical practice.

2.6.2 Limitations and Future Work

This work discussed the results we obtained from the forearm, specifically, the wrist where the microreliefs are more prominent than in other parts of the body. We use the wrist for developing the algorithms since we can manually annotate the junction points for ground truth validation. However, the device is capable of imaging other areas of the body. In the future, we plan on imaging the rest of the body so that we can further verify the microrelief structure is unique to an individual and body part. If we can prove the structure uniqueness, we can use the skin structure as a form of person identification and use it for body positioning. Additionally, a more diverse subject population (in age, ethnicity, and variety of skin conditions) will further enable us to understand the normal variations in microrelief structure to better assist diagnosis.

CHAPTER

3

SUPERFICIAL VASCULATURE

Studying the vasculature has many important clinical and biometric applications as detailed in Section 1.3. It can be used for person identification, body mapping, and health monitoring (disease progression) among other applications. Looking at veins can also be useful if the skin surface is diseased and the structure is not discernable. As with skin imaging, monitoring the superficial vasculature requires hardware and software innovations, which are driven by clinical and technical needs and constraints.

The designed imaging technology must allow for high contrast, repeatable image capture of the superficial vasculature. For pervasive use in clinics, the system must be technologically superior to existing technologies (listed in Section 1.3.5), inexpensive, and easy-to-use. A handheld form factor is desired for increased portability and full-body access. Ambient light noise is less of a problem than with microrelief imaging since vasculature is imaged in the NIR spectrum; however, the imaged region of interest (ROI) must still be uniformly illuminated and robust algorithms developed for proper image analysis. The system design requirements are summarized in Table 8.

This chapter describes the image capture system and associated algorithms developed to characterize, quantify, and measure veins in high resolution. With a compact handheld form factor, the developed system enables large area scanning and, in the future, could be used to determine if veins are unique among individuals and distinct in each part of the body. Additionally, we developed algorithms to locate a small image patch taken from a random location on the forearm within the full forearm map. By finding this small patch over time, we can start to understand vascular stability over time.

Table 8: System Design Requirements to Image the Superficial Vasculature

Requirement	Specification/Design Parameter	Primary/Secondary?
The system can image the superficial vasculature of the body.	Image features on length scales from 0.2 – 4mm in thickness, with depths up to 8mm from skin surface.	Primary
The system allows image parameters to be varied.	Change camera exposure, lighting parameters, and optical zoom.	Primary
The system provides high quality images.	Image has uniform lighting. User can resolve all the superficial vasculature.	Primary
The system can take repeatable images.	Can return to same imaged region multiple times.	Primary
The system prevents deformation of the skin surface.	Minimize contact area.	Primary
The system is easy to use.	"Plug-and-play" system.	Secondary
The system can be used anywhere and at any time of day.	System is light invariant and images in NIR spectrum.	Secondary
The system takes images that can be used to get a large area patch on the human body.	The FOV is between 1cm and 20 cm.	Secondary
The system is lightweight.	System is less than 4 kg.	Secondary
The system is ergonomic.	Operators do not have to use extra attachments during imaging. Subjects do not have to rest body parts on hard surfaces or hold body in uncomfortable positions for long periods of time.	Secondary
The system is cost – effective.	System costs less than existing state-of-the-art technology at $20,000 (Ideally, system should be <$2500).	Secondary
The system is portable.	System is handheld.	Secondary

3.1 Handheld Vein Imaging Device

The vein imaging device has similar components as the handheld skin imaging device. In particular, there is: (1) a light source (now in the NIR spectrum) to uniformly illuminate the ROI,

(2) a camera sensitive to NIR wavelengths to clearly distinguish the superficial vasculature (Chapter 1), and (3) a housing fixture that encompasses all the components in their proper configuration and in an ergonomic form factor. Each component selection and design is described below [73].

3.1.1 NIR Camera

Clinical needs and technical requirements in the NIR regime drive the camera selection process. Clinicians require a small, lightweight system with flexible positioning and a variable FOV that ranges from 1cm – 20cm to image various parts of the body where the veins are clinically important (i.e. the smaller regions, like the elbow for blood draws, and the bigger regions, like parts of the leg for diagnosing DVT) [45]. Additionally, it must be easy-to-use, requiring only a simple PC/laptop connection. For static vein imaging, camera resolution and frame rate are not as important as long as the quantum efficiency (QE) at 800nm is at least 30%. QE describes how sensitive the sensor is during low-light conditions. Veins are discernible even in images with low resolution given the centimeter scale features.

Based on these specifications, the Manta G145B-NIR camera with gigabit Ethernet (GigE) connection is selected. The Manta G145B-NIR camera is lightweight, weighing 200g, and is small, measuring 86.4mm (L) x 44mm (W) x 29mm (H) [74]. Each pixel measures 6.45μm x 6.45μm on the CCD sensor, with overall picture size of 1388 pixels x 1038 pixels (1.6MP camera). At a resolution of 0.01cm/pixel, the image size is 13.88cm x 10.38cm. A lower resolution is compensated with a smaller WD. Depending on how deep and how prominent the veins are, the WD is variable between 5.5in (14cm) and 7in (17.8cm).

Despite having a slow frame rate 15.0 frames per second (fps), we choose the Manta G145B-NIR because of its high QE (~37%) at 800nm (an important clinical requirement) as shown in Figure 26a. The peak QE occurs at ~625nm, which is on the border of the visible and NIR spectra. A 1x M1620-MPW2 C-mount lens from Computar (same one used for skin imaging) is connected to the camera. As seen in Figure 26b, the lens has more than 50% transmission in the NIR range (700nm – 100nm). With a length of 47mm, this lens satisfies the minimum 8mm focal length requirement to prevent shadows on the image edges and prevent barrel distortion on the ROI.

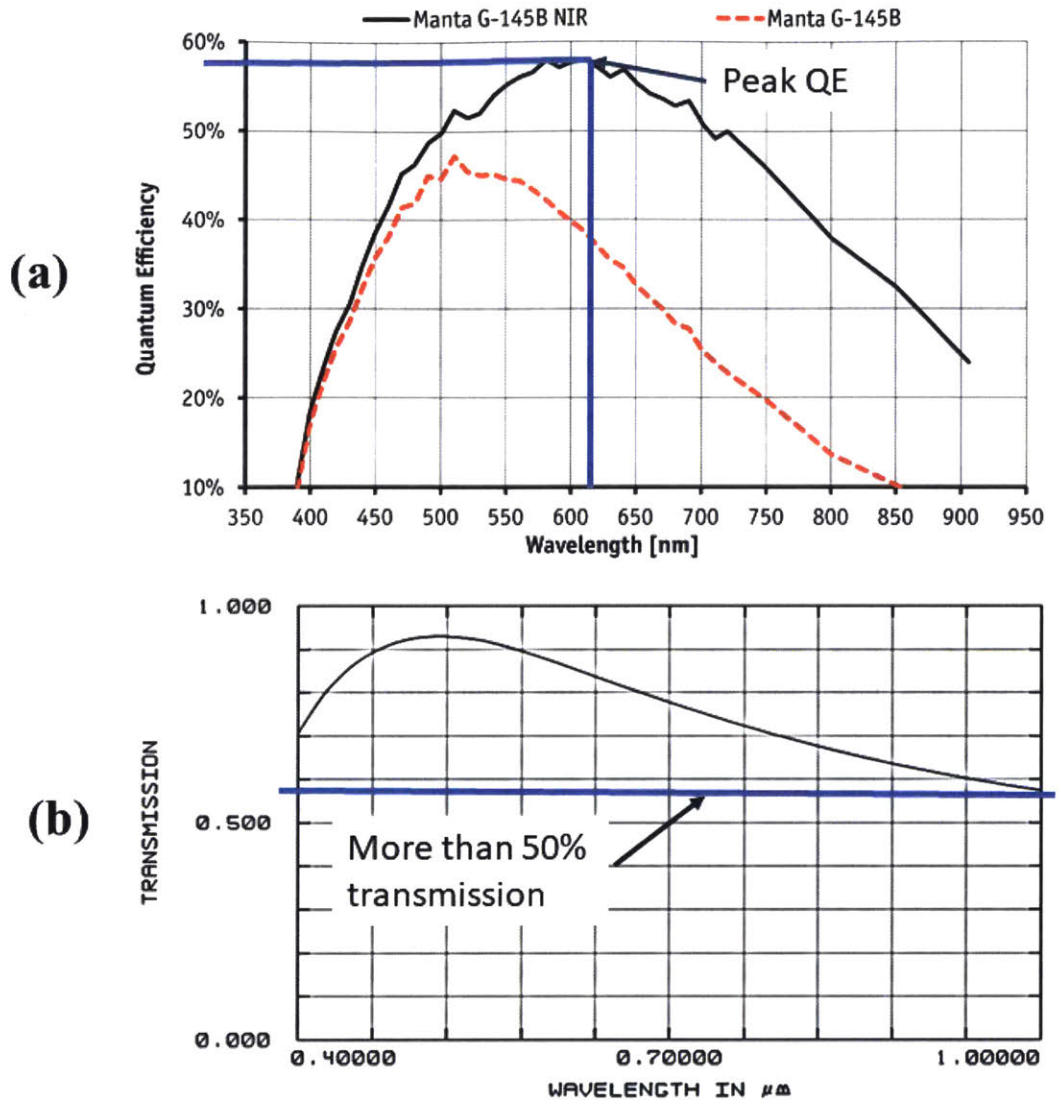

Figure 26: Technical Specifications for the Manta G145B-NIR camera and the M1620-MPW2 Lens: (a) Quantum efficiency curve for Manta G145B-NIR camera shows the camera meets the minimum clinical requirements of more than 30% QE at 800nm. **(b)** Transmission curve for the M1620-MPW2 lens shows it is transparent in the NIR range of 700nm – 1000nm.

3.1.1.1 NIR Camera Control

Camera control must be easy-to-use and intuitive for clinical applications. The camera should be compatible with software in which various camera parameters can be controlled, such as LabVIEW. The Manta G145B-NIR camera is controllable with Vimba Viewer, a software from Allied Vision Technologies (AVT, MA). Vimba Viewer allows various parameters to be

optimized, some of which are highlighted below. Specific values for experimentation are found in Section 3.2.

NIR Boost Modes: Vimba Viewer allows the NIR cameras to increase NIR sensitivity while sacrificing frame rate. Since we require only static image capture (not video) for our application, a decreased frame rate is not concerning. (We will be stitching the static images together to obtain a full map of the forearm as detailed later in Section 3.3.)

Exposure: defined as the amount of light entering the lens. Vimba Viewer allows manual exposure control to vary from 20μs - 60s depending on NIR mode. Experimentally determined, an exposure time of 2000μs – 5000μs is required for blood vessel imaging.

Binning: a method in which multiple pixels are combined into one for higher quality, better pictures.

Gain: for CCD imaging, gain is defined as the magnitude of amplification for an image, or the number of electrons/ADU (analog-to-digital unit). Vimba Viewer permits manual gain control between 0dB – 33dB, of which 0dB – 3dB is used during experimentation for optimized vein images.

3.1.1.2 Other NIR Cameras Considered

Two other NIR cameras were considered with various specifications in order to ensure the proper camera was selected for design and experimentation. The alternatives were selected based on technical specifications (is NIR imaging possible?), ease-of-use (is it controllable with accompanying or custom-designed software?), portability (what are the camera dimensions?), and cost (all ranged in $1500 - $2500). Considering all four metrics in aggregate, the Manta G145B-NIR camera proved superior and was selected as described in Section 3.1.1.

Also controlled with Vimba Viewer, the Mako G419-NIR was a natural alternative. The Mako G419-NIR camera is rated as clinical grade with a higher resolution (4MP) and smaller dimensions (29mm x 60.5mm x 29mm) than the Manta G145B-NIR. Despite the higher QE at 800nm (~45%), the peak QE occurs at <600nm; the camera is more sensitive in the visible region and not able to capture the superficial veins despite using a dominant NIR light source. Additionally, it requires one Ethernet cable to power the camera and stream from it (compared to the two cables required for the Manta G145B-NIR). However, having only one cable makes it difficult for portability; connecting to a laptop was not possible since Wi-Fi did not produce enough bandwidth to power

the camera and allow streaming from it simultaneously – an Ethernet port would always be required.

The PCO Pixelfly USB was considered as a camera with USB connection, but the same resolution as the Manta G145B-NIR. Sized at 39mm x 71.5mm x 39mm, this option has similar portability as the Manta G145B-NIR. The accompanying software for the PCO Pixelfly allowed for manipulating parameters (such as bin size and NIR boost mode) that would enhance the images in the NIR region. However, even with the boost mode, the QE at 800nm was merely 25%, substantially lower than that of the Manta G145B-NIR. The peak QE occurs at 500nm, once again illustrating the Pixelfly's superiority in the visible spectrum.

Magnification lenses of 1x, 1.5x, and 2x were considered to see if deeper veins and/or smaller veins are visible under different magnification. The idea was to increase the resolution of the imaging system to see the smaller vessels. Experimentally, no difference was found. Using a NIR filter (715nm – 1095nm) also did not enhance the vascular imagery since the camera is already filtered to the NIR spectrum. So the cheapest and simplest solutions were incorporated in the final design, which meant having a 1x lens and no filter.

3.1.2 Light Source

Once again, clinical needs and technical specifications drive the selection of the light source. High quality images require even, distributed lighting on the ROI with light sources that can be very expensive. However, clinicians seek a low-cost solution. Additionally, the light source must properly illuminate the ROI such that the veins are discernable in the NIR spectrum. Heat is known to enhance NIR images (since heat causes blood vessels to expand to bring the blood closer to the skin surface), but is clinically uncomfortable to apply heat to the patient's body for imaging. Thus, selecting the light source requires a balance between clinical and technical needs.

The next consideration is where to place the light source with respect to the ROI. Placement of the light source is dependent on the imaged area. For imaging the veins in smaller areas (i.e. fingers), the NIR camera must capture the transmitted light through the ROI by placing the light source behind the ROI [34]. For larger, thicker areas (i.e. arm and hand), the light source is placed in front of the ROI and the reflected light is imaged to see the vasculature. Since the forearm is being imaged for first data collection, the light source is placed in front of the arm and the light

reflected off the surface is imaged (Figure 30). With this light source-ROI configuration, we need a ring light that can be integrated in a compact form factor as discussed in Section 3.1.3.

A concentric LED ring light is used to provide even, distributed lighting on the ROI. To determine the appropriate wavelength, we consider the wavelengths as which blood vessels absorb light and determine the light source wavelengths must be greater than 580nm to image the vein instead of the arteries at which point the vein absorption is greater than artery absorption (Figure 27). Readily available ring lights of 850nm and 940nm were selected to obtain better images with more narrow wavelengths. At 940nm, long exposure times are required to see the veins clearly, but this also blurs the image since subject breathing causes motion in the ROI, making it impractical for use in a patient centered device. An 850nm light source provides uniform lighting and clearly discernible veins across a variety of subjects, which matches literature reports of using 760nm (for pale skin) and 920nm (for darker skin) [48]. However, the geometry of these ring lights are not compatible with the existing camera and lens since the rings lights were too small to fit around the camera-lens system. Finally, an intensity adjustable 880nm ring light from Edmund Optics (Part 66-783) is selected since the wavelength is within the operating range and the dimensions are appropriate (WD: 4in, diameter: 100mm).

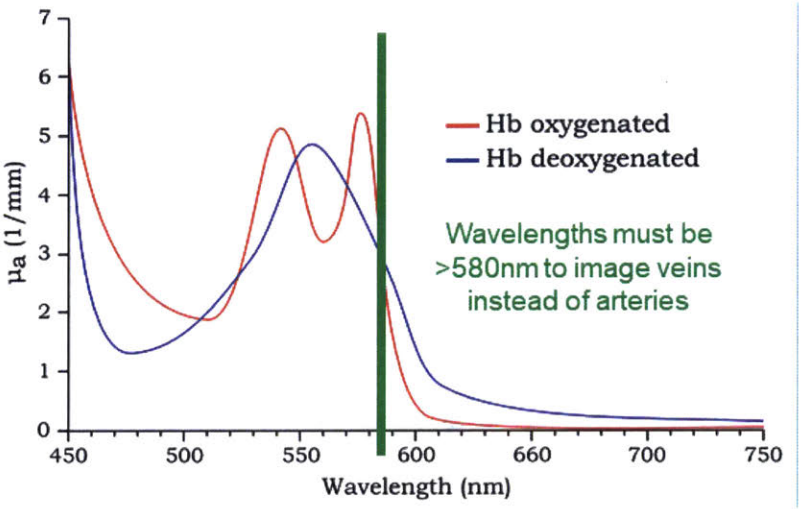

Figure 27: Blood Absorption Based on Wavelength: Veins carry deoxygenated blood from the tissues back to the heart, so we care about the blue line of the graph. We must image at wavelengths >580nm to image the veins instead of the artery where the absorption of the blood vessels is greater than the absorption for the veins [75].

3.1.2.1 Alternate Light Options

For first data collection, a broadband light source (500nm – 9000nm) (ThorLabs SLS203L, NJ), with a peak wavelength of 2400nm was used. This was selected to confirm that veins on human subjects are visible in the NIR spectrum since the camera could only capture wavelengths up to 900nm (Figure 26a) despite the broadband light emission from the source. The light source enabled us to see veins, but because of the large geometry and high heat generation during use, it was impractical to use this in the final device prototype. Additionally, the housing of the device (with plastic components in front of the light source) caused reflections and shadows on the ROI, which affected future image processing (Figure 28). One final drawback of this light source was the high price point; at $1600, this light would not satisfy the requirement of being inexpensive as outlined in Table 8.

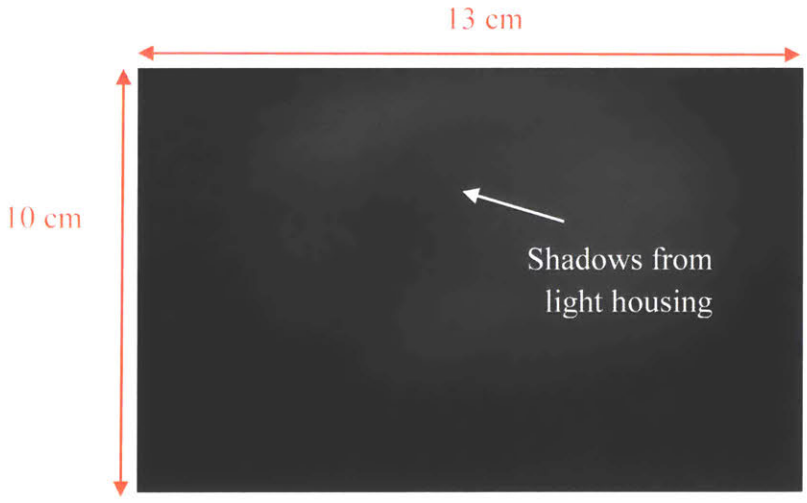

Figure 28: Reflections on ROI from Broadband Source

A next step was using readily available 40W tungsten bulbs, which are inexpensive and have low heat dissipation (i.e. do not generate much heat when turned on). While these bulbs primarily operate in the visible spectrum, veins were still discernable (Figure 29), which tells us that tungsten bulbs have some NIR emissions as was verified by a spectrum analyzer. The round housing for the bulbs provides better, diffuse lighting on the ROI. These provided better quality images for later image processing, but again, could not be incorporated into the final prototype given the need for additional sockets to plug in the bulbs and a large bulb head.

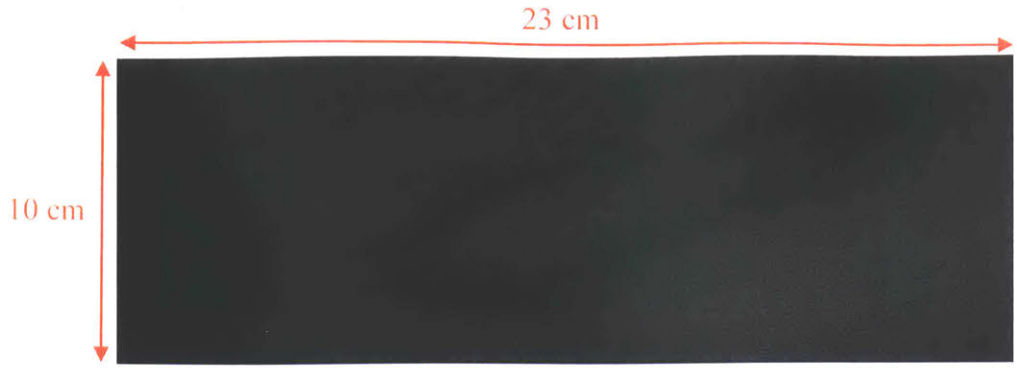

Figure 29: Uniform Lighting and Visible Veins in ROI using a Tungsten Bulb for Illuminating the ROI

3.1.3 Housing Fixture

The housing fixture was designed after the configuration of the light source, camera, and ROI were determined from a benchtop setup as described in [73]. Preliminary experimentation confirmed that the light source must be in front of the ROI (i.e. the forearm) so that the reflected light is imaged. In other words, the camera and the light source must be on the same side of the forearm as described earlier in Section 3.1.2 and shown in Figure 30. This configuration leads to a similar design as the handheld skin imaging device with a ring light flush against the camera lens (Figure 31) and the camera encased in an easy-to-hold housing. The light-camera subsystem is kept at a set WD away from the ROI, which is accomplished by adjustable opto-mechanical rods and a ring stand.

Figure 30: Light, Camera, and ROI Configuration for High Quality Vein Images: The light and camera must be on the same side with relation to the ROI (i.e. the forearm) in order to image the reflected light from the forearm, which makes the veins more prominent.

Figure 31: Ring Light Flush with Camera Lens for a Convenient Form Factor and Maximum Portability

3.1.3.1 Iteration 1

The first iteration of the device was 3D printed with ABS plastic on the Stratasys uPrint SE with sparse density settings to save fabrication time. Despite the 0.01in resolution of the printer, the intricacies of the device made this version of the fixture very weak. To hold the heavy light source in place, the light holder was designed as a press-fit and dimensioned to keep the light source hidden from view (more aesthetically pleasing) and keep a small form factor (Figure 32). The slot cuts to adjust the lens parameters (exposure, optical zoom) made the light holder less rigid and more compliant, which allowed the light to slide in easily. Additionally, the light source was kept in place with its cable mount since the cutout for the light cable was appropriately dimensioned and incorporated into the mount design.

Ergonomics and design for assembly (DFA) were other considerations in this iteration. Minimal material (enough to protect and secure the components) was used for maximum comfort since more material would make the device bulky and difficult to hold (Figure 33). Other ergonomic considerations are in adjusting lens focus and exposure without removing the lens from the device, which is made possible with the slot cuts (Figure 33a), and in holding the device, which is made possible by contouring the surface of the mount with the hand (Figure 33b). Finally, the ring stand of the handheld skin-imaging device is replaced by a more ergonomic stand, which contours the ROI. In this iteration, the base was slightly too big for ergonomic comfort, a flaw which was modified in iteration 2 (see Section 3.1.3.2).

Figure 32: Camera and Light Fixture: By keeping the light hidden from view, we keep a small form factor to make it handheld and more aesthetically pleasing.

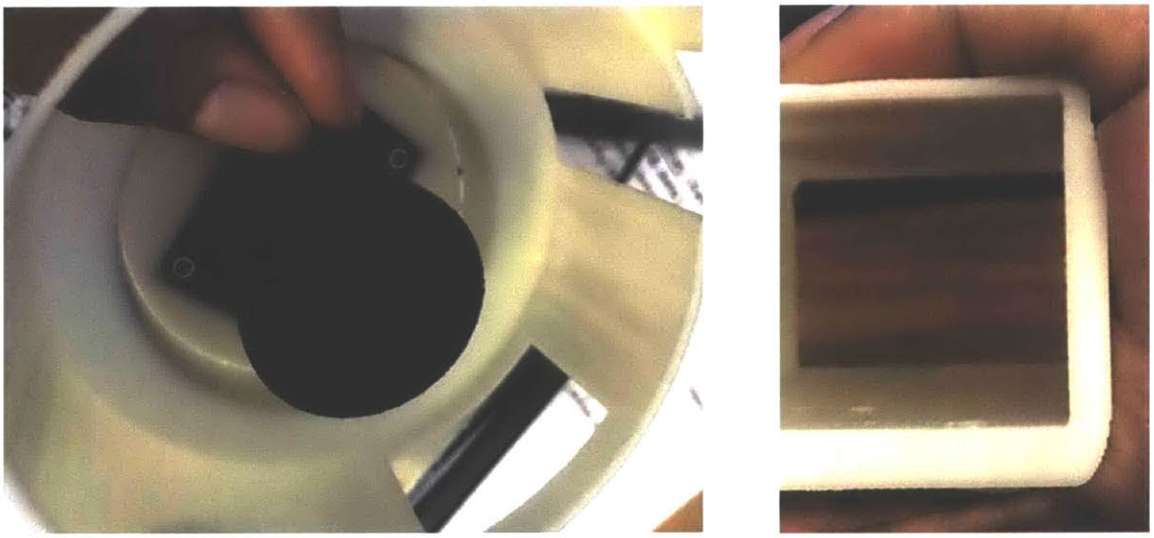

Figure 33: Ergonomics of the Handheld Vein Imaging Device: **(a)** Slot cuts to adjust the focus and exposure of the lens **(b)** Contoured housing surface for a more comfortable hold. There is just enough material to encase and secure the components to the mount.

To easily attach the camera to the mount, a camera stop was designed to fit the front face of the camera. This prevents the camera from moving while it was being screwed into the mount (Figure 34).

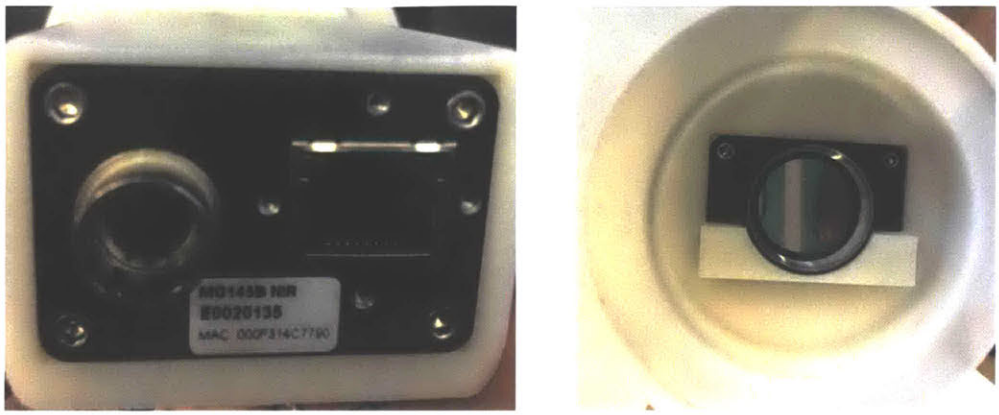

(a) **(b)**

Figure 34: Ergonomic and DFA Considerations on the Mount: The camera aligns in the **(a)** back and **(b)** front with the properly dimensioned mounts.

3.1.3.2 Iteration 2

From the portability, size, and ergonomic perspectives, iteration 1 proved adequate. However, the device was not fully stable because of the sparse density printer settings and the excessively large base to frame the ROI; these issues were modified in iteration 2. Now printed with high density settings, the two-pronged system could not break as easily, despite the intricate features. A more contoured base (Figure 35) prevented rotation about the arm axis, which makes the overall system more stable. The full device is shown in Figure 37.

Figure 35: Contoured Base along the ROI: This base helps increase device stability during experimentation

3.1.3.3 Future Iterations and Design Changes

Future iterations of the device could include improvements in the light source or device design. The tungsten bulb (Section 3.1.2.1) showed the power of having a light source that incorporates visible and NIR wavelengths since obtaining vein images required low exposure times with the visible spectrum components and the veins were visible with the NIR components. A custom designed light source is a solution where LEDs of various wavelengths are integrated together in a circular pattern. Figure 36 shows an initial attempt incorporating visible and NIR LEDs with wavelengths of 660nm, 680nm, 780nm, 850nm, 870nm, 910nm, and 940nm. Unfortunately, the LEDs were much too low power to properly illuminate the ROI. More convenient form factors could be custom manufactured, but were not pursued due to long lead times and high price points.

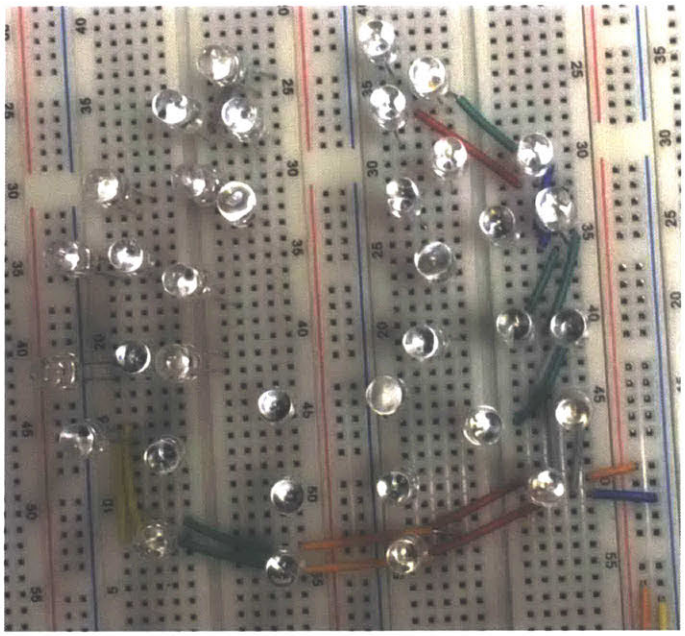

Figure 36: Breadboard LED Ring Light: This breadboard prototype incorporates visible spectrum and NIR LEDs with wavelengths of 660nm, 680nm, 780nm, 850nm, 870nm, 910nm, and 940nm.

From the design perspective, several modifications could make the device more ergonomic. The base, though improved in iteration 2, is still large for subjects with small arms. Designed for the largest 5% of subject forearm widths [76], this stand could be designed to be appropriate for a larger population. One possibility is making the ring stand spring-loaded to hug the arm curvature. Alternatively, the large base could slide along rails on either side of the forearm, in which case accounting for all forearm widths would not be necessary. Another design change to make the

device more stable is using three prongs (similar to the skin-imaging device) instead of the current two-pronged configuration. The two prongs are used in conjunction with the new base design and for aesthetic purposes.

To image other regions of the body, the base design would have to change. Currently, it contours the limbs, of which the arms tend to be narrower than the legs. For increased flexibility, the spring-loaded base suggestion from above might be a suitable alternative. With a camera more sensitive in the mid-IR to FIR wavelengths, we can see the deeper veins on other parts of the body as they will penetrate deeper than the 1cm depths of the superficial veins. This would require objectives with different magnification and filters tuned to the appropriate wavelengths. Except when imaging the fingers, for which transmitted light is imaged to see the veins, the lens and camera will always be on the same side with respect to the ROI since reflected light is imaged to see the veins on the thicker parts of the body.

3.2 Acquiring Vein Images (Experimental Procedure)

The image acquisition procedure and workflow is designed with the intent of capturing a map of the superficial vascular structure. Thus, the experimental procedure must facilitate repeatable image capture to determine if the vasculature is stable over a period of time. This means selecting the camera settings (exposure and gain) such that high quality vein images (with uniform lighting on the ROI and vein structures visible) are acquired consistently across multiple sessions. Images are taken in a room with no ambient light; the only light source is the aforementioned 880nm ring light. After experimenting with various exposure settings and continuous gain, the optimal exposure is set to 2000μs - 5000μs and the gain is set to 0dB – 3dB, both of which depend on the subject's skin pigmentation and vascular prominence. The exact settings are selected by the operator by varying the parameters and determining which setting provides focused vein images and uniform illumination (without oversaturating the ROI). Images for most of the subjects in our data set (healthy individuals in their 20s with varying skin pigmentation and vein prominence) were acquired with an exposure of 3312μs and a gain of 0dB.

The subject is asked to keep their forearm flat on a hard surface with the handheld device placed on the forearm such that the camera is always normal to the ROI as shown in Figure 37. This configuration minimizes variability in the data collection, since the device will always be perpendicular to the arm regardless of arm placement, making the skin mostly planar to simplify

the future image processing. The WD can be adjusted for different individuals, if needed, with the opto-mechanical rods adjusted by the set screws on the device.

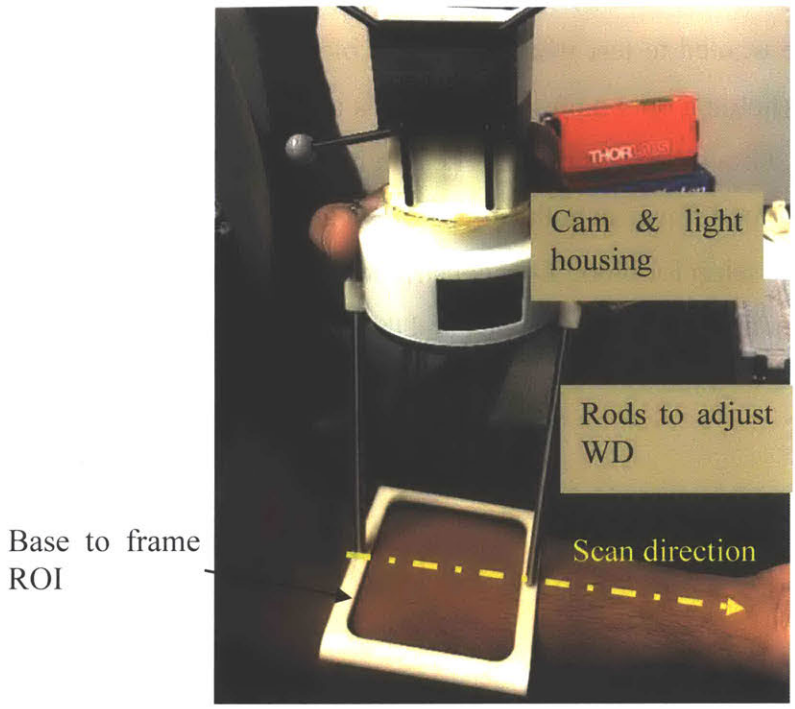

Figure 37: Experimental Setup for Acquiring Vein Images: The forearm is kept flat on a hard surface with the handheld device on top such that the camera is always perpendicular to the ROI as shown. The device moves along the length of the forearm from elbow to wrist, as indicated with the dotted arrow.

To obtain large area vein images representing the entire limb, we use an image stitching process as described in Section 2.3.2. The first image is acquired at the elbow crease. The device is moved along the arm as indicated in Figure 37 and an image is captured every few centimeters, which ensures sufficient overlapped areas between images (i.e. 2cm – 3cm overlap to have enough vascular features that can be matched across pairs of images). Again, the overlap helps with later image processing. A total of 5-10 images per forearm are obtained and the stitch of the arm is processed as detailed later in Section 3.3. Note that only one stitch of the arm is required for baseline data (i.e. have only one map). To find a small image patch from a random location on the forearm within the full map, we keep the ROI perpendicular to the camera at a fixed WD before capturing an image. When the subject comes in for repeat imaging (so we can monitor the long term stability of the veins), only a small image patch is captured from the forearm (i.e. we do not generate a map at each visit).

3.2.1 Experiments

Experiments were performed to see if the blood flow in the superficial veins could be increased enough to induce a change in the vessels, which could be measured from a visible difference in imagery. Specifically, we wanted to test what happens if blood flow is increased or constricted [77]. A forearm exercise (holding onto a pressure ball) was used to increase the blood flow in the veins of the forearm [77]. Gravity effects (letting the arm hang for extended periods of time) and using weights to increase blood flow can both enhance vessel prominence when the vasculature is difficult to image [32]. The setup for blood flow constriction was similar to the clinical practice of phlebotomy where the area above the elbow is tied and the subject makes a fist [77]. These setups are found in Figure 38.

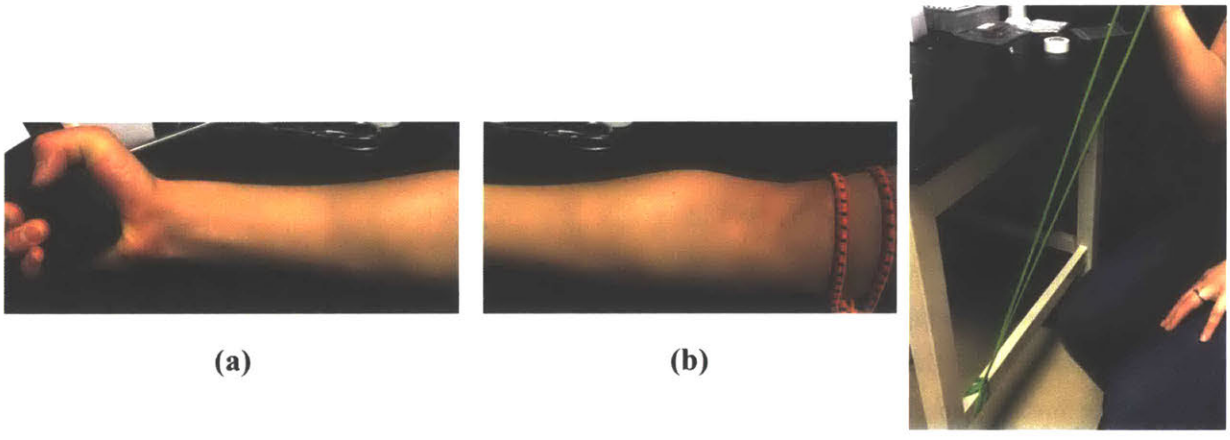

(a) **(b)** **(c)**

Figure 38: Setup of Controlled Experiments: **(a)** Forearm exercise to increase blood flow in the forearm veins. **(b)** Blood vessel constriction above elbow to allow blood pooling in the veins at the elbow as in phlebotomy. **(c)** Using weights to increase blood flow in the forearm for subjects with veins that are hard to see.

3.3 Processing the Vein Images (Image Processing)

Once the vein images are acquired, they have to be analyzed in order to understand the variation in dimensions across the body, the stability of the vascular structure, and the usability of the superficial veins as a map for the body. Figure 39 summarizes the steps involved with processing the images. Each step is detailed below.

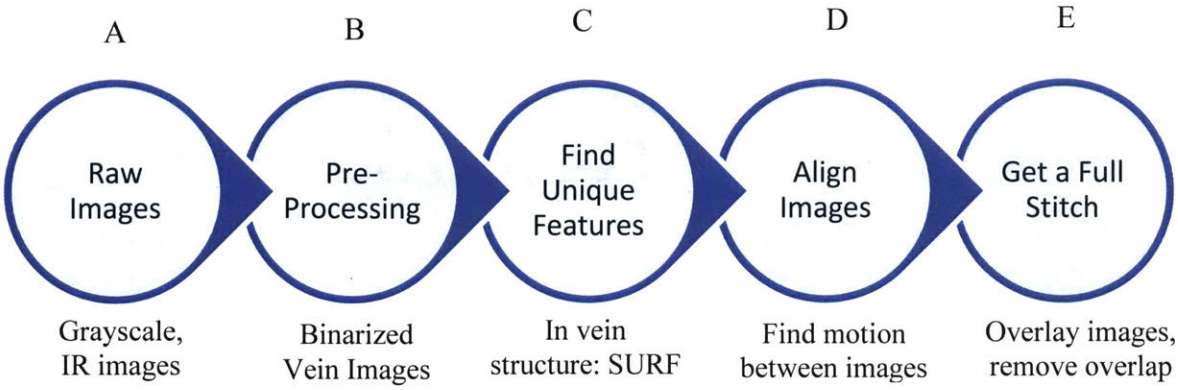

Figure 39: Overview of Image Processing Steps to Get a Vein Map of the Body

The raw images (obtained during experimentation, corresponding to Step A above) must first be pre-processed to extract the vascular structure from raw images and to find unique features of the vein network that can be used for registration (unique features are described later). Pre-processing is an important step that gets rid of other surface information (i.e. hair and lighting effects) that are present in the image (Step B). Through contrast enhancement (with the DoG technique outlined in Section 2.4), thresholding, filtering, and binarization, the raw, grayscale images are transformed to binarized vein images as shown in Figure 40.

Outline for segmenting vasculature from raw forearm images:

1. Apply a Gaussian filter with standard deviation, σ_1, to obtain the high contrast image: a small standard deviation is used to smooth the image and get the high contrast version (here we use $\sigma_1 = 7$, the size of the smaller vessels)
2. Apply a Gaussian filter with standard deviation, σ_2, to obtain the blurred image: a larger standard deviation is used to blur the image, usually $\sigma_2 > 10\sigma_1$ (here we use $\sigma_2 = 80$. After experimenting with different σ_2's, we found this 10-fold increase provides the best segmentation, while preserving much of the original network)
3. Subtract the blurred image from the high contrast image
4. Apply a filter (median filter) to eliminate speckle noise
5. Use adaptive thresholding to binarize the image (a sensitivity of 0.4 provides best results as determined through multiple iterations)
6. Clean the image through morphological processing, eliminating small patches of hair or other non-vascular features

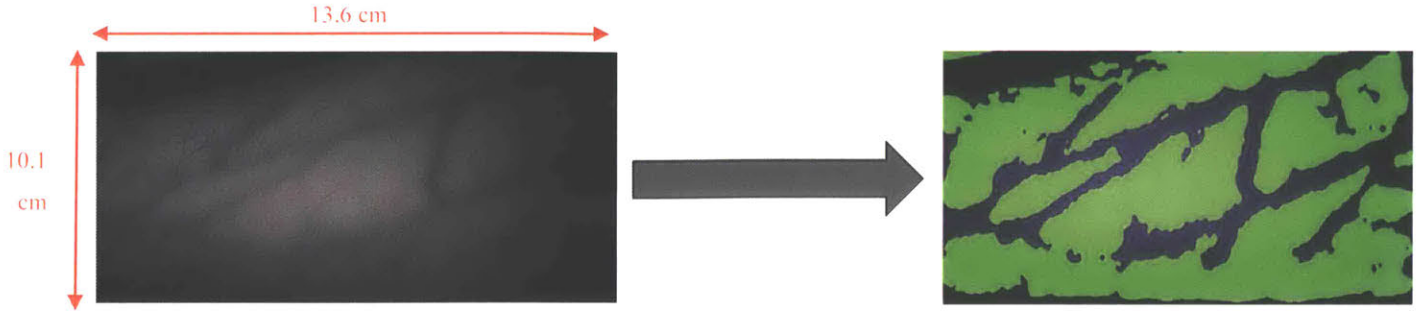

Figure 40: Pre-Processing Raw Images (Left) to Enhance the Vasculature and Eliminate Surface Effects. The result is the binarized, vein segmented image (right)

A closer look at the binarized vein images (Figure 41) shows that there are high frequency textures on the image edges that are artifacts of the image processing. Although efforts were taken to ensure uniform illumination in the ROI, the image edges may still have had some shadows. These shadows are enhanced during image processing because they appear darker than the surrounding skin, which leads to binarized regions that are separate from the vascular network. Therefore, it is important to look at the raw images to know which is the vascular structure before analyzing the vasculature (Figure 40).

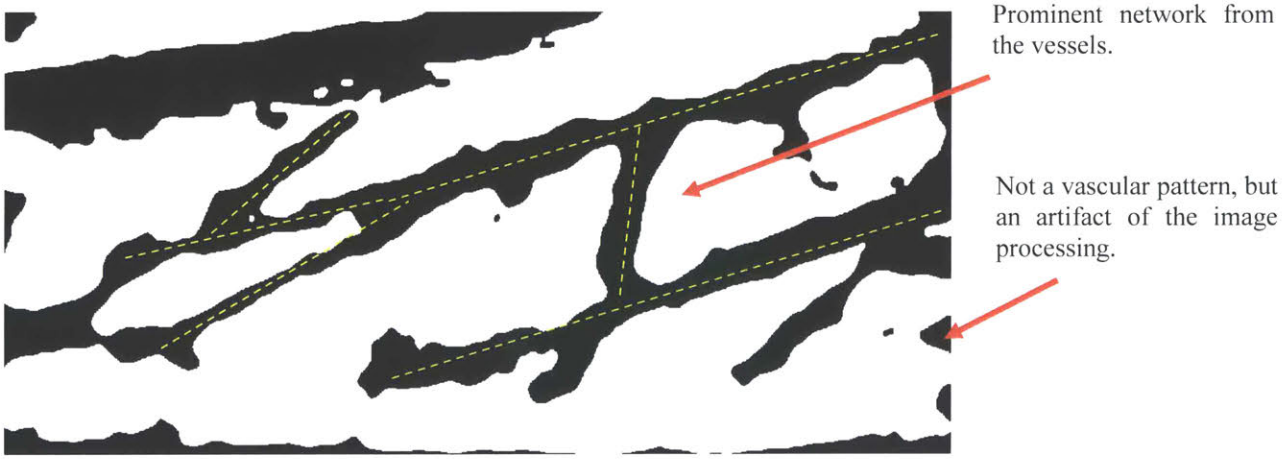

Figure 41: The binarized vein image shows the prominent vascular network structure along with some artifacts from the pre-processing.

To create a panorama (or stitch/mosaic) from several individual images, it is important to find local features of the images and match those features (Step C). Local features are regions of pixels which are distinct, robust to occlusion and clutter, can achieve real-time performance, and may number

in the thousands in a single image [62]. Unique features invariant to geometric changes (translation, rotation, scale) and photo quality (brightness, exposure) are desired. The area around the features (called the "feature descriptors") must also match. There are a number of image processing tools that can be used to find appropriate features and their associated descriptors – examples include Harris, FAST, SIFT, SURF, MSER, and BRISK [65], [67]. Features that are scale independent (such as SURF, BRISK, and MSER) are desired (Table 9), of which the Speeded-Up Robust Features (SURF) proved most reliable and robust over a variety of imaging and lighting conditions.

The salient features of the vascular network are found by extracting SURF features, which are used to find blob features and are a fast approximation of the more commonly known Scale Invariant Feature Transform (SIFT) [78]. SIFT features are commonly used in image processing, but SURF features are better for vein segmentation because they require less computation time during extraction than SIFT and are equally robust. Though fewer SURF features are found in an image compared to SIFT, the SURF features are robust to rotation, scale, noise, illumination, and viewpoint changes. This allows for a more robust algorithm since unique features can still be found with minor variations in image acquisition.

Table 9: Possible Features to Extract from the Vein Images for Matching

Feature	Type	Scale Independent?
FAST	Corner	No
Min Eigen	Corner	No
Harris	Corner	No
SURF	Blob	Yes
BRISK	Corner	Yes
MSER	Region	Yes

Note that there are no extracted vein features on the raw images from Step A since the grayscale images have too much surface information (i.e. hair, skin texture, illumination changes, etc.) as shown in Figure 40; the features must be extracted from the pre-processed binarized vein images. Features on the detected edges and skeletonized versions of the raw images are not stable enough over time (i.e. the features are not matched from the vasculature, Figure 42), so we use the pre-processed, binarized images as described above to extract features from the segmented vein images

(Figure 40). Each image has more than 1500 SURF features, of which 100 are important and/or unique (Figure 43).

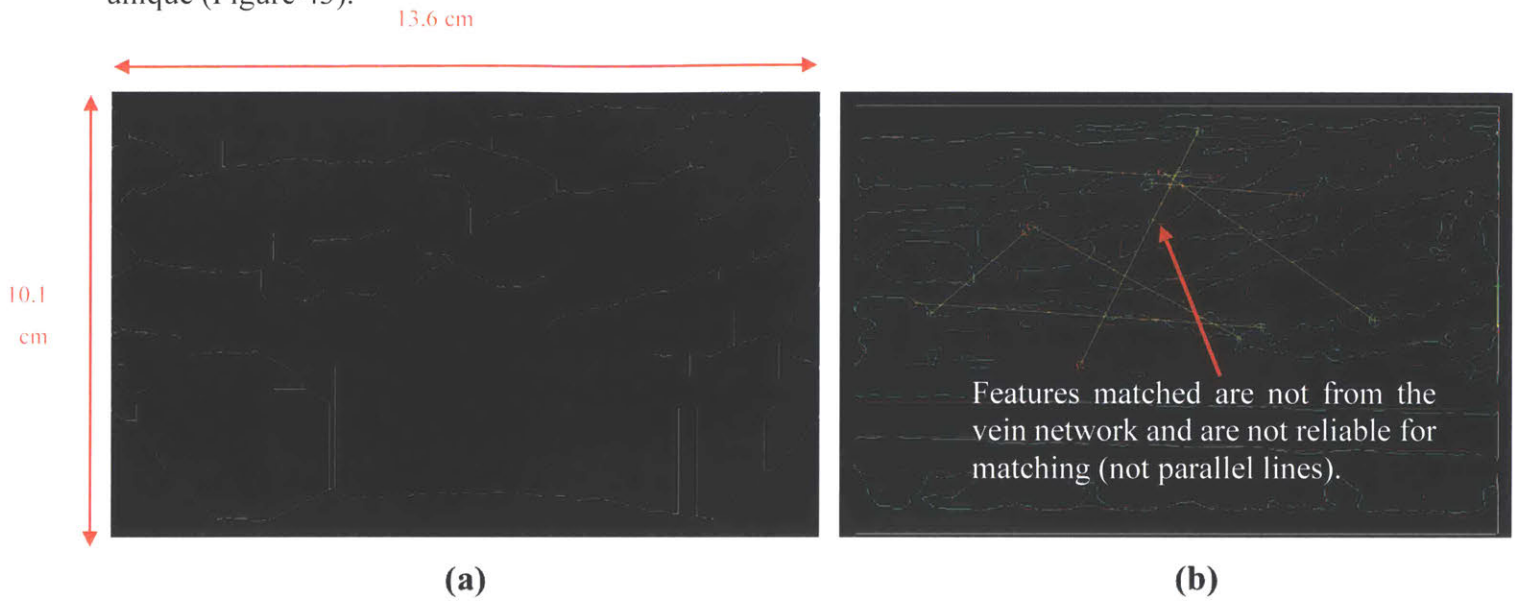

Figure 42: Alternate Pre-Processing Options: (a) Skeletonizing the image: the network is visible, but the lines do not resemble the vasculature visible to the human eye. **(b)** Edge detection makes the vessel structure more visible, but the features matched from these images do not result from the vascular features.

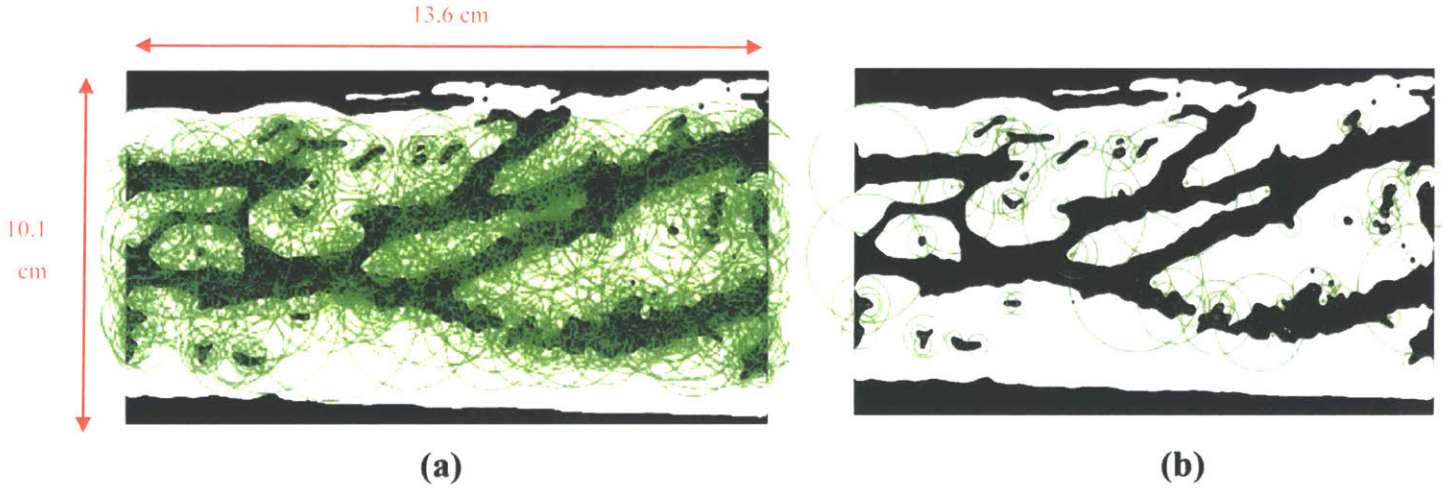

Figure 43: SURF Features detection on the segmented vessel images: (a) There are 1500+ detected SURF features on the binarized vessel images, **(b)** Only approximately 100 of the detected features are unique and can be used for matching.

After finding the unique features of the vein extractions, the next step is to match those features and align the two images in the same reference frame (Step D). Also known as "registration," this process looks at the common features between two subsequent images to find the motion between

them (referred to as the "homography" between two images [67]). Though hundreds of feature points are found between any set of images, there are less than 100 inlier points, which are used to find the transformation between images. Inlier points are the strongest matches, which are scale invariant and consistent despite illumination and viewpoint changes. For the vein images, these inlier points are usually found on the edges of the most prominent vein structures (i.e. on the bigger, thicker veins and not on the smaller veins) since those veins will be in the images regardless of viewpoint or lighting variation (Figure 44b). To solve the homography matrix (i.e. finding the amount of rotation and translation between images), a minimum of 5 unique points are required. A.1 shows there are 9 unknowns, so 5 points gives 10 equations (2 equations for each x, y point) with which we can solve the homography matrix. More points are redundant and may also lead to unreliable results since we require the strongest matches throughout the pairs of images; fewer points are likely to be consistent through images (hence we use only the minimum number of points required to solve the system). An example registration between two images is shown in Figure 44.

Once the images are registered based on unique feature points, the next step is to "stitch" the images together (Step E); in other words, overlay the images at the location of the inlier points so that both images have the same reference point. We assume the feature points can be identified with minimal deformation, which we explore later in Section 3.4.1. Individual pairs of images are stitched together (Figure 45a) before they are all stitched together to get the full arm stitch, which serves a full arm map of the vasculature (Figure 45b).

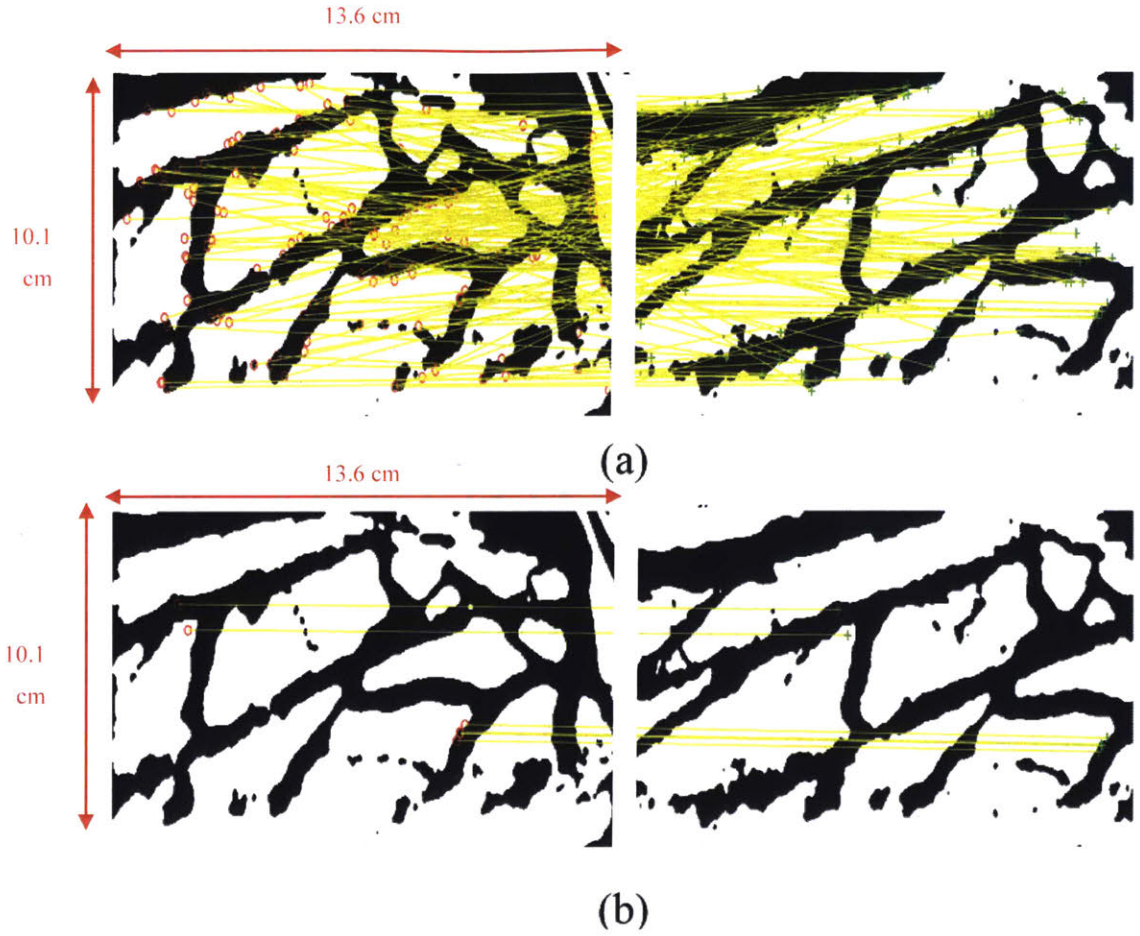

Figure 44: Registration Process Between Two Images: **(a)** Matched feature points between two images are shown with the corresponding yellow lines; there are 100+ matched feature points between two images. **(b)** Inlier points are the strongest matches from (a) that are used for registering the images. 5 inlier points are required for registration to solve the homography matrix; many more points would be redundant to solve the system and may lead to detecting unreliable feature points.

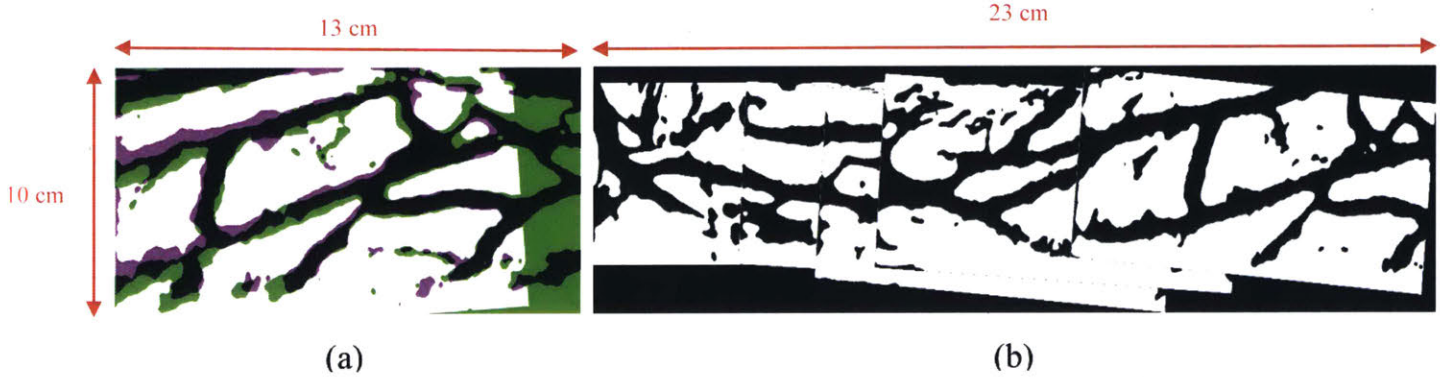

Figure 45: Stitched Images: **(a)** Two images are overlaid and matched at the locations corresponding to their inlier points. The green shows the areas of vasculature in the first image and non-vasculature in the second image; the pink lines show the vascular structure of the second image, but not in the first image; the black lines in the white space show the overlapping vascular network that is present in both images; the white space are the regions of no vasculature

in both images. **(b)** Multiple images stitched together get the full stitch of the arm, which serves as the "vascular map" of the arm.

3.4 Results

The images are analyzed with three applications in mind, which are further outlined in the subsequent sections: (1) using the veins as a map for the body to know the physical location on the body, (2) using the veins as a biomarker to aid in early diagnosis of various vascular conditions (i.e. DVT), and (3) using the veins as a unique biometric identifier. Successful implementation of the above goals requires answering two questions: (1) how unique is a pattern of local vasculature (i.e. is it possible to find a random image within the "map" of the arm that was created) and (2) how stable is the superficial vascular structure over time (i.e. can an image be re-localized if it is taken some time after the map was created?)? These questions motivate the analysis described below.

3.4.1 Re-Localization (Vascular Body Map)

To find a small image patch within the full stitched map, feature based re-localization is used. Feature based re-localization registers the images based on feature points as described in Section 3.3. It is more robust than shape matching techniques since feature matching looks at the strongest representative features of the vascular network instead of looking for exact shapes within the vasculature which may appear different with slight viewpoint shifts. Thus, if there are slight variations during image acquisition, the unique features of the vascular network should still be present and the small local image can still be placed within the full map.

Viewpoint variations can arise if the device is not perfectly normal to the body (assuming normality was maintained during image capture used to create the full map, as described in Section 3.2). Lighting variations can easily occur (i.e. different ambient lighting conditions in different clinics). These variations can affect the visualization of the vascular structure – if the arm rotates and the viewpoint changes, the veins may look thicker or thinner from one viewpoint to another.

To determine how much viewpoint variations affect the re-localization capabilities of the system, we keep the device normal to the body to capture the initial images and create a full forearm map (experimental procedure outlined in Section 3.2). The subject is then asked to minimally rotate their arm while maintaining forearm contact with the table surface

(approximately 30° rotation) and an image acquired at a random location on the forearm. This image is then found within the two maps acquired with up to 30° viewpoint shifts. As shown in Figure 46, a small image patch (10cm x 13cm) can be re-localized if the arm has minimal rotation when using feature-based techniques. Note that smaller patches of vasculature are likely unique and can be found within the stitch, but have not been fully quantified yet. Initial analysis shows that patches 1/8th the size of the original, small image patch (1.25cm x 1.625cm) can still be found within the full map as long as the unique vascular features used for matching are present in the small image patch.

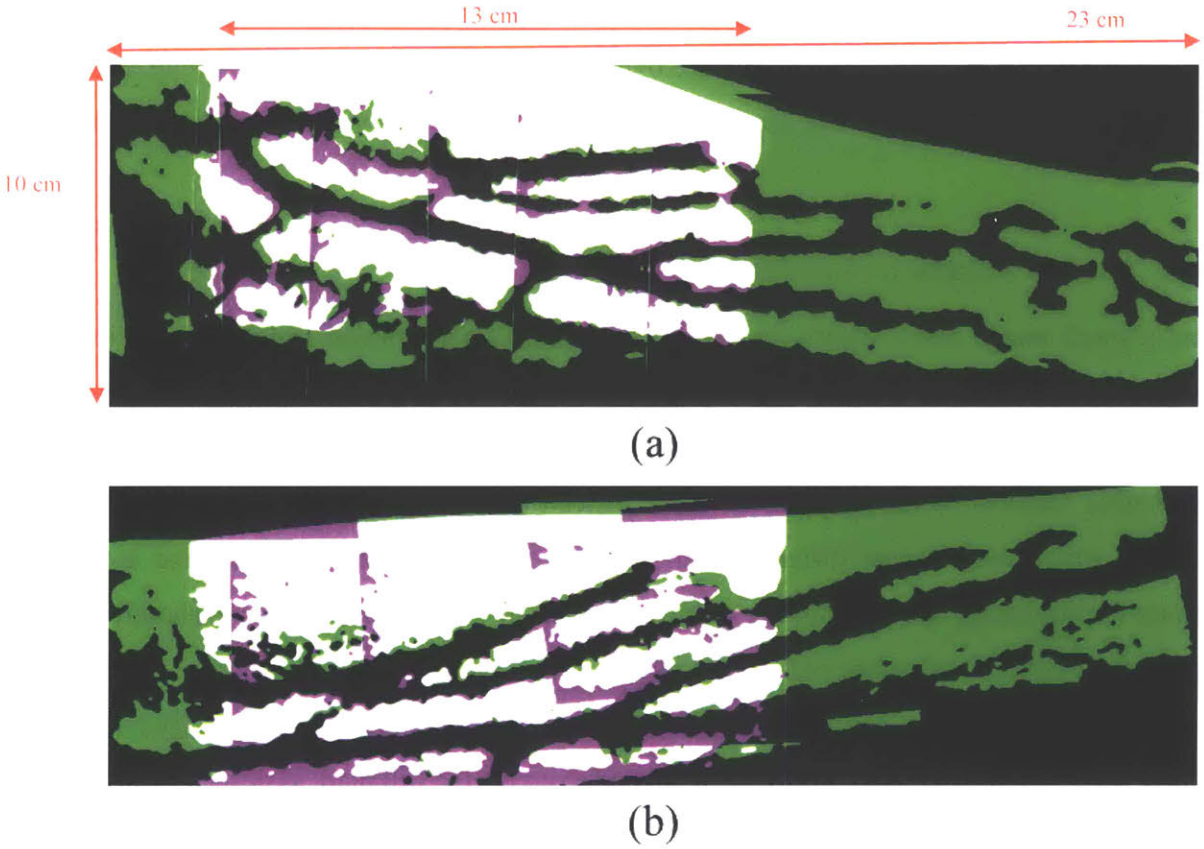

Figure 46: Re-Localization of a Random Image within an Arm Stitch: With feature-based re-localization, small viewpoint changes (up to 30°) do not affect the ability to find a random image within a map. The same random image can be found within a stitch from two different viewpoints, (a) and (b).

3.4.2 Vascular Stability over Time

To test the stability of the vasculature, a small image patch (size of the image obtained with the device: 10cm x 13cm) is taken some time after the forearm stitch is created. Subjects are imaged

the same day as the full forearm map is created, 1 day later, a couple weeks later, and a couple months later. Not all subjects could be imaged over long time intervals; most subjects were imaged over the course of two months, one subject was imaged over a period of 8 months. Using the same feature-based registration techniques as described in Section 3.3, the strongest vein features from the small image can still be matched in the full map after some time has passed. New local images are taken from a random location on the subject's forearm at intervals of 0 days (same day), 1 day, 60 days (2 months), and 240 days (8 months). The small images acquired at these different time intervals are then matched on the full forearm map using the unique features from the vasculature; the location of the small image patches relative to the full map for one subject are found in Figure 47. Note again that the small image is the size of the image that our device outputs (10cm x 13cm) and that the smallest image size at which the unique vascular features can be extracted is still an area of investigation.

The amount of overlap, indicated by the black networks in the white background, illustrates overlapping vasculature between the two images where the green is the stitch (or "map") of the forearm. Note that the original stitch and first small image patches were acquired with the benchtop setup described in [73] (before the vein imaging device was designed). The small image patch acquired with the benchtop setup and vein imaging device is found within random places on the forearm map acquired with the benchtop setup at the initial visit (in the middle of the map (Figure 47a), near the bottom of the map (Figure 47b), near the top of the map (Figure 47c), and near the right end of the map (Figure 47d)). The different positions illustrate the noticeable viewpoint changes observed over time. Despite the minor viewpoint changes, there are still overlapping features in the vasculature that can be used for finding a small image within the full forearm map. Since partial vascular re-localization is possible after 240 days (8 months), there is good reason to believe that superficial veins are stable and can be used for tracking location on the body by looking at the vascular structure.

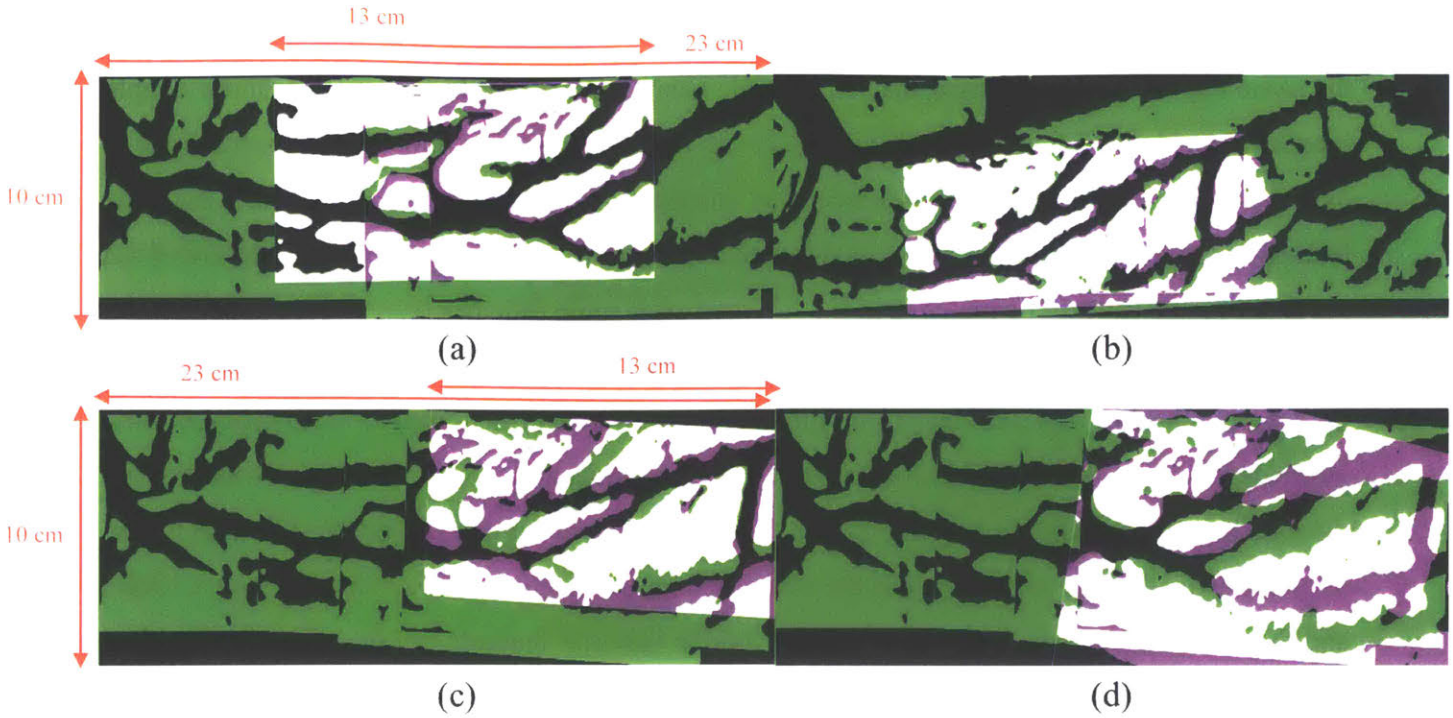

Figure 47: Re-Localization of a Small Image (Local Vasculature) within an Arm Stitch over Time: The prominent features of the vascular network for this subject can be re-localized over time as shown with the black lines overlapping in the white region. **(a)** Small local image taken same day as arm stitch is generated. **(b)** Small local image taken 1 day after arm stitch is generated. **(c)** Small local image taken 60 days (2 months) after arm stitch is generated. **(d)** Small local image taken 240 days (8 months) after arm stitch is generated.

Presented above is a qualitative method to understand vascular stability over time. One approach to quantify stability is to compare the amount of pixels in the image that represent vasculature to see if it changing over time (i.e. is the amount of vasculature the same over time). We care about the percentage of black pixels over time – since black pixels are the vasculature that are the same between two images, decreasing proportions of black pixels indicate less accurate matches. However, since veins are constantly restructuring and there is no published value in literature about the amount of expected change over time, we must consider all possible combinations to understand biological phenomena like: dilation/expansion of vessels, contraction/shrinking of vessels, twisting/restructuring of vessels, and any vessel growth [79]. We do this by looking at the different pixel colors (pink, black, white, and green) in the registered images as described next.

If the vessels are stable over time and assuming perfect acquisition and registration with no observable biological phenomena (i.e. no deformation), the percentage of black and green pixels (representing the vessels of image 1) and black and pink pixels (representing the vessels of image 2) must be the same. With perfect matching, the percent of black pixels should stay constant over

time. The information about the percentage of vessels in an image should be used in conjunction with the amount of matching vessels in order to understand the evolving nature of the superficial vein network. For example, if the proportion of vessels in one image is greater than the other but the percent of black (matching) vessels is constant, some vessel growth must have occurred.

From the overlapping image patch, the pink, green, and black pixels are segmented and counted as shown in Figure 48. Table 10 and Figure 49 give the values obtained when performing the analysis described above on one subject over time; this data corresponds to the pink, green, black, and white pixels of the images shown in Figure 48. While this shows the amount of vasculature over time for one individual at an instance of time, the same analysis can be performed for multiple individuals as long as the overlapped image patch has black, green, pink, and white pixels.

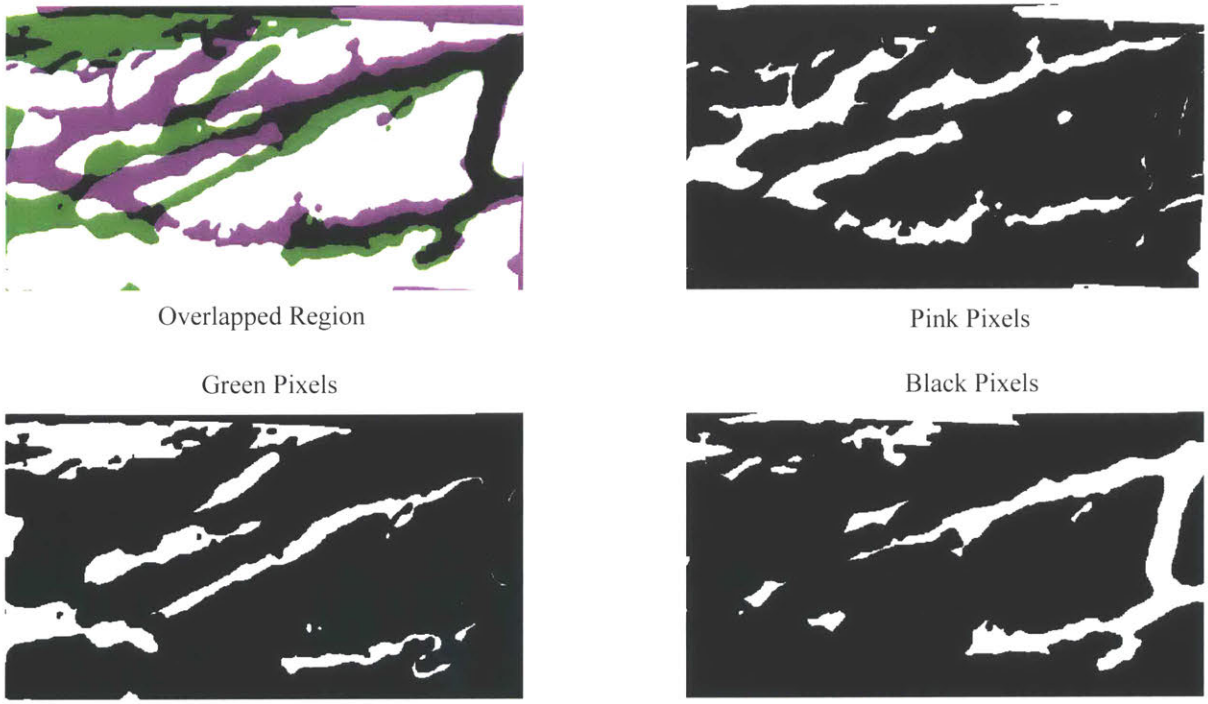

Figure 48: Segmenting the Various Colored Pixels to Understand Vascular Stability Over Time (Data for one subject at one instance of time.): We care about the amount of pink + black and green + black pixels over time to understand if the amount of vessels is changing over time.

From Table 10 and Figure 49, we see that there is only partial matching over time in this individual as the proportion of black vessels decreases over time. However, since the proportion of vessels is roughly consistent over time (blue and red lines in Figure 49), we confirm that the decreasing

amount of match (less black pixels over time) results from the viewpoint shifts overtime due to the inconsistent experimental process used to obtain this data set.

Table 10: Vein Matching Over Time: Comparing proportion of vasculature present over time. Corresponds to **Figure 47** and **Figure 49**.

Day Interval	% Black Pixels in Image	% Black + Green Pixels in Image (veins of image 1)	% Black + Pink Pixels in Image (veins of image 2)
0	27	34	35
1	25	34	34
60	19	34	34
240	24	40	35

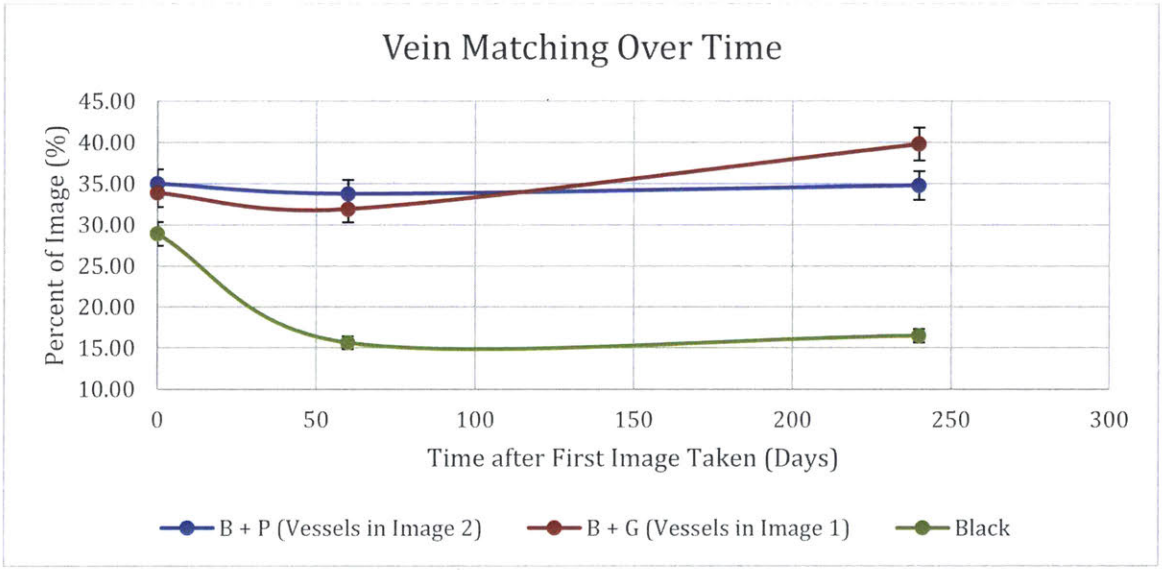

Figure 49: Vein Matching over Time: Proportion of vasculature present in images over a period of 8 months. Corresponds to data in **Table 10**. Error bars at 5% illustrate the data is consistent over a number of data sets.

Unfortunately, we were not able to monitor many subjects over time and therefore cannot confirm if the trend shown in Figure 49 is typical over long periods (more than 2 months). So we use the data we have to check the stability over short periods (less than 2 months) for three subjects. Again, we segment and count the black, pink, green, and white pixels of the overlapping image for each individual at each instance of time to get the vascular proportions in each image (like Figure 48). Averaging the findings over the subjects, we can generate a table like Table 10 and plot the matching vasculature over a short period of time. Figure 50 shows the percentage of the image covered by veins (black and pink pixels or black and green pixels) is roughly constant for intervals

up to 1 month. Over short time, the proportion of black pixels is also relatively constant, indicating the viability of using veins as a body positioning system since the vein structure matches are constant over short periods of time with controlled image capture.

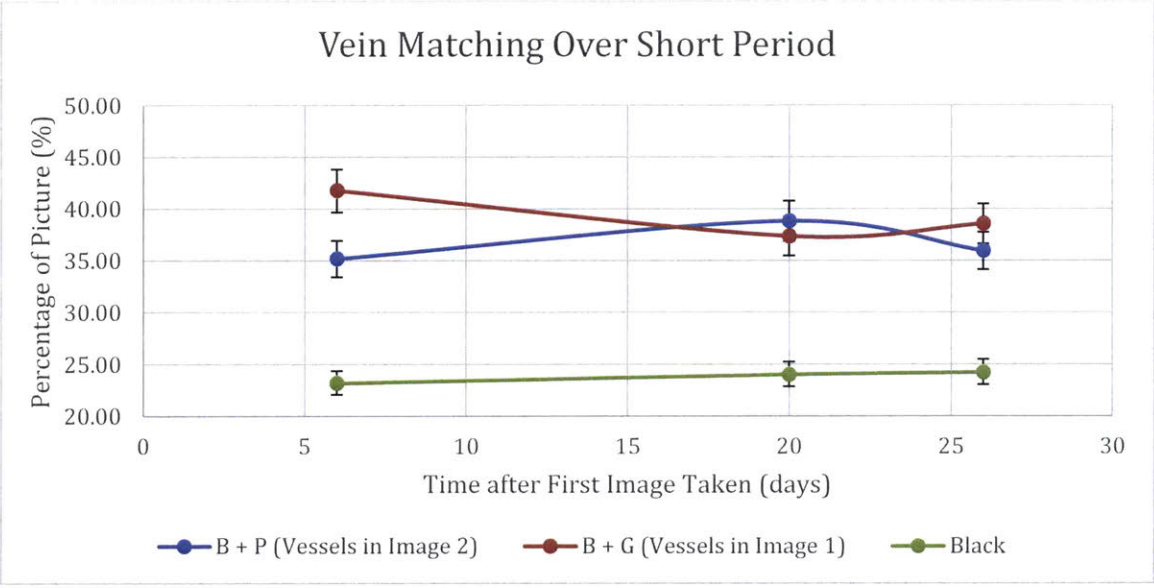

Figure 50: Vein Matching over Short Time Periods: Proportion of vasculature present in images over short period (2 months). The proportion of vessels in the image and the percent of vessel matching stay constant in the short term. Error bars at 5% illustrate the data is consistent over a number of data sets.

3.4.3 Sensitivity Analysis

Sensitivity analysis is required to understand how robust the device and developed algorithms are. If the system can observe small changes in structure, it can be used for non-invasive diagnostic purposes.

3.4.3.1 Algorithm Robustness

In order to evaluate system variability, particularly algorithm robustness, imaging parameters are varied. With slightly differing viewpoints, the small image patches can be stitched and re-localized as detailed in Section 3.4.1, where minimal forearm rotation still allowed a small local image to be found within the stitch. Additionally, different light sources were used over time (a period of 8 months) to acquire the small images (Section 3.1.2) and we can still localize the small image patch from a random part of the forearm within the full forearm map. Since the images acquired with different light sources can be found on the same map (the handheld device and EO light ring for

images taken at 8 months of Figure 47d and the benchtop setup with broandband light source used for the full map and images taken at 0, 1, and 60 day intervals), we believe the developed algorithms make the system somewhat light invariant.

To test if the developed vein segmentation and matching algorithms can be used when the vascular size is different from the size of the vessels at the time the stitch is created, we use synthetic images. Vascular variations can result from illness (i.e. blood clots can expand the vessels; dehydration can compress the vessels) and are important to study for clinical applicability. The sensitivity analysis presented here is performed with synthetic images that simulate stretching (expansion) and compression (contraction) of the blood vessels. Synthetic images were generated by re-sizing (expanding or shrinking) the binarized images along the length and width of the image by appropriate distances (0cm, 0.5cm, 1cm, 1.5cm, 2cm). Since we empirically measured that natural skin stretches at most 1.5cm when deformed along the length of the arm (could be a result of the image scanning process), we use this value as a benchmark to determine appropriate amount of distortion to generate the synthetic images (expansions up to 2cm and contractions up to 2cm). Sample synthetic vessel image patches within the full arm map are found in Figure 51 (stretch) and Figure 52 (compression). Note that rotations are not synthetically generated since vasculature does not change angle on its own; any angular shift would result from viewpoint changes, which have been discussed in Section 3.4.1.

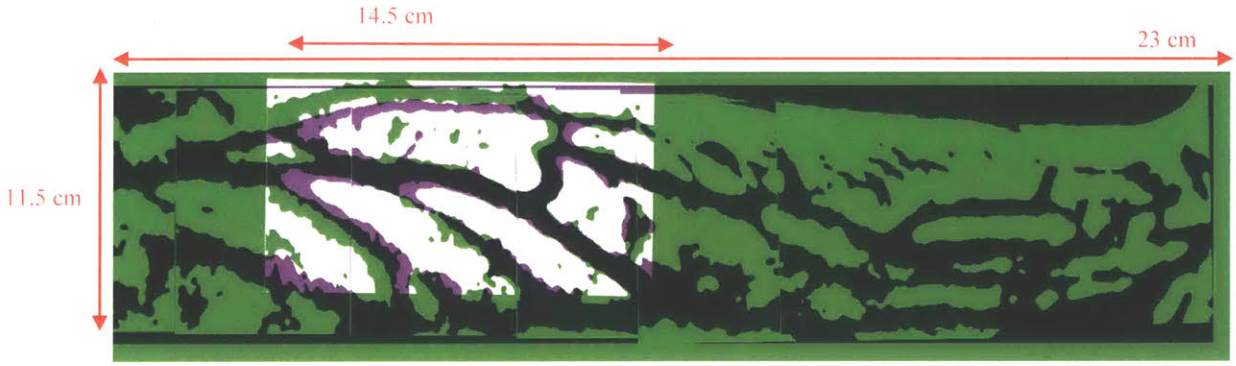

Figure 51: A synthetically stretched image patch is found within the full forearm map. A stretch of 150 pixels along the length and width of the binarized image correlates to a 1.5cm stretch of the vessels, which can still be found within the original forearm map. Black indicates matching vascular pixels as before.

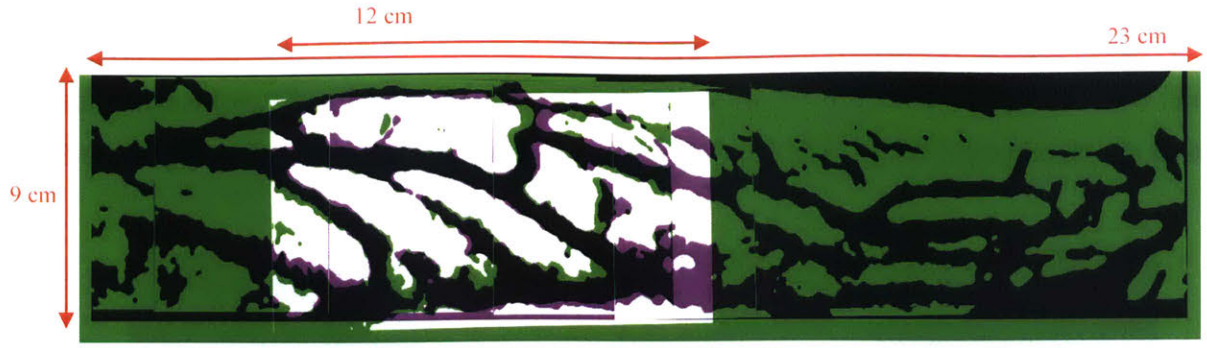

Figure 52: A synthetically compressed image patch is found within the full forearm map. A compression of 100 pixels along the length and width of the binarized image correlates to a 1cm compression of the vessels, which can still be found within the original forearm map. Black indicates matching vascular pixels as before.

From Figure 51 and Figure 52, we qualitatively notice that more areas of mismatch (i.e. more green and pink pixels) are present when the vessels expand compared to when they contract. For vascular disease (i.e. DVT), we expect the vessels to expand more when blood clots are present, so matching when vessels expand is important. Since matching is still possible with 1.5cm expansion, we believe this method and approach for matching vein regions can be used to aid in diagnostics for clinical use and vascular disease. We can use the distortion and normal vein sizes to aid in diagnostics. Superficial veins on the forearm in this experimental data set range in diameter from 0.13cm – 0.35cm. The results from the expansion and contraction experiments are found in Table 11.

Table 11: Sensitivity Analysis with Simulated Expansion/Contraction of Blood Vessels

Image Distortion [cm]	Simulates?	Localization Possible?
2	Expansion	No
1.5	Expansion	Yes
1	Expansion	Yes
0	Nothing	Yes
-1	Contraction	Yes
-1.9	Contraction	Yes

3.4.3.2 Device Robustness

Under certain constraints, the algorithm can correctly re-localize an image to a stitch with simulated stretching of the superficial vein network (Section 3.4.3.1). Now, we want to see if the system can detect changes in vein size due to changing blood flow. Inspired by the clinical practice of phlebotomy where blood flow is constricted above the elbow [77], 18 sample image sets are

obtained with the experimental process as outlined in Section 3.2. Specifically, we use the device to look at the blood vessel width (Median Cubital Vein) before and after constriction (Figure 53).

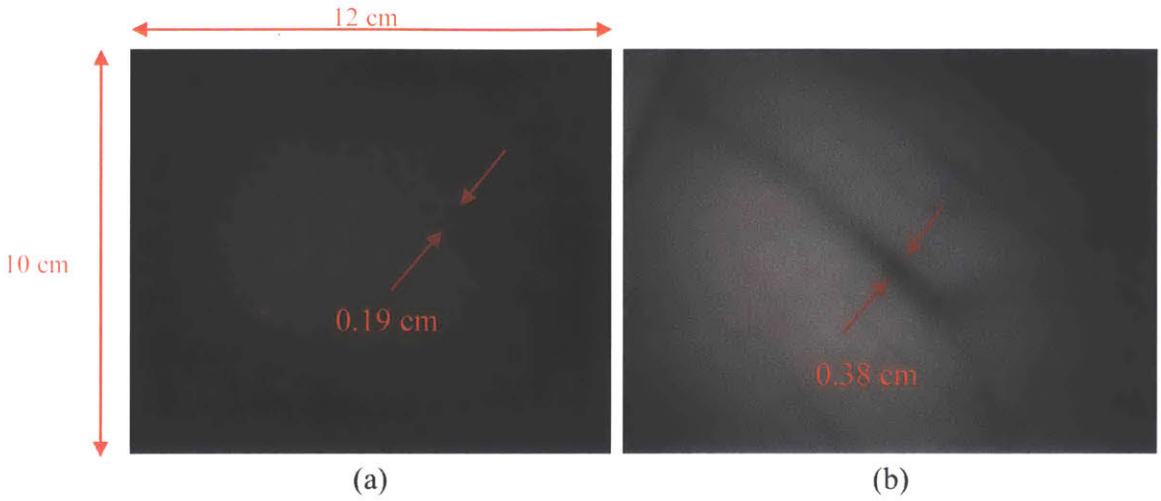

Figure 53: Experimental Images to Test Device Robustness: The median cubital vein is more prominent after constricting flow above the elbow **(b)** compared to **(a)** since the constriction allows the blood to pool in the vein.

The area around the elbow is imaged for 18 subjects before and after constriction so that the median cubital vein is prominent. We use this vein to understand the impact of restricted blood flow in vessel size variation as it is the most prominent in the images and used for blood draws [77]. Smaller vessels are also seen after constriction (Figure 53b), but not used for evaluation since these veins are not as clinically important.

Using a paired t-test at 95% confidence for the data, we find a significant, observable difference in the median cubital vein width before and after constricting blood flow ($t = 3.89 > t_{crit} = 2.11$). Specifically, we find that constricting blood flow increases the blood vessel width, which agrees with clinical observations where constricting blood flow enlarges blood vessels to make it more prominent [77].

We image the vessels in the rest of the forearm to suggest a range of normal blood vessel size variation in healthy individuals, which is currently missing in existing literature. The imaged population consists of nearly 20 individuals in their 20s and 40s with varying skin pigmentation, muscle definition, and different lifestyle habits (i.e. weight lifting, coffee habits, etc.). The median cubital vein, ulnar artery, and basilic vein were all prominent in the sample forearm images and could be measured to understand normal variation (Figure 54). Blood vessels ranged in size from 0.17cm – 0.71cm with no external manipulation. Using this data set of nearly 30 healthy image

samples, we noticed a mean increase in vessel width of 0.16cm is expected with a standard deviation of 0.17cm (Figure 55). Significant deviations from this baseline could indicate a more serious health condition.

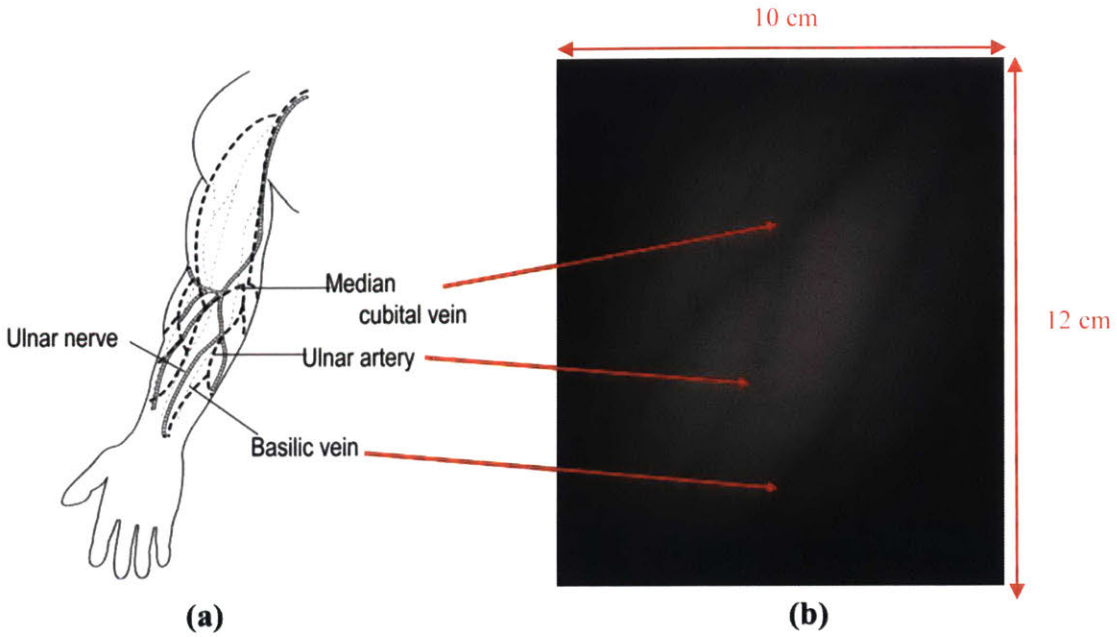

Figure 54: Vessels along the length of the forearm: The median cubital vein, ulnar artery, and basilic vein are prominent in the vein images acquired. They can be measured to understand normal vessel size variation across a population.

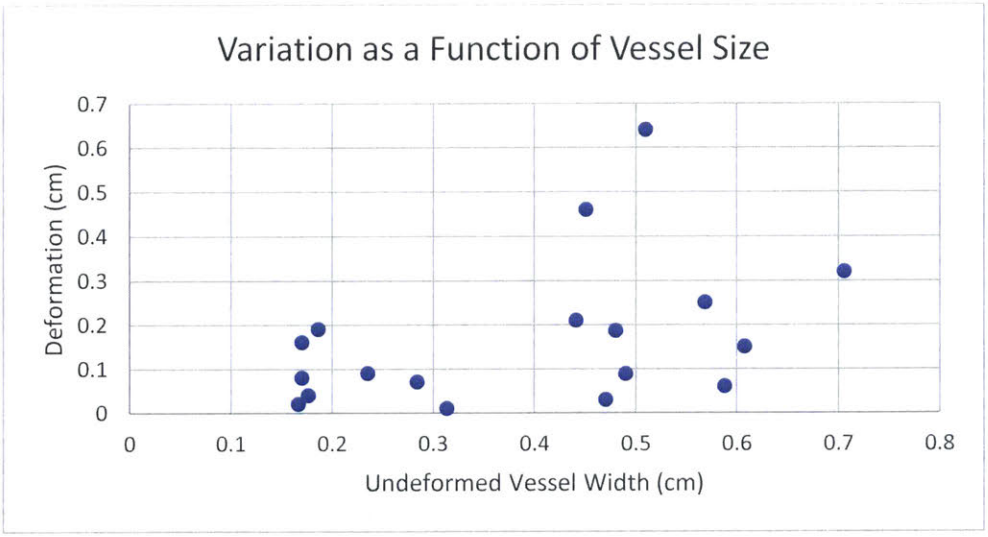

Figure 55: Variation as a Function of Vessel Size: This graph illustrates the amount of vessel deformation correlated to the undeformed width of the median cubital vein. With this sample set, we find that the data is not normally distributed, but can determine the range of variation in vessels across our healthy volunteer population.

3.4.4 Use as a Biometric

Prior work suggests the vasculature is unique among individuals, especially in the fingers and palms [30], [31]. Little work has been done to determine if the vascular structure on the rest of the body is also unique. There are a number of methods that can be used to characterize the vascular network. Examples include texture analysis (such as Local Binary Pattern), fingerprint analysis (shape context matching techniques), image based analysis (feature based techniques, Fourier transforms, independent component analysis/singular value decomposition), and other quantitative metrics (graph theory, network theory). Here, we use the qualitative image based analysis and quantitative network based characterization to determine if two vascular networks are similar.

3.4.4.1 Qualitative Approach

As a first demonstration, the forearm vasculature on a pair of identical twins (call them Subject 1 and Subject 2 for anonymity) is used to demonstrate how to approach visualizing uniqueness; their full arm vasculatures are found in Figure 56. The experimental setup was consistent between image acquisitions of the subjects and a small local image obtained from their forearms can be found within each subject's respective stitches (not pictured, but using the same techniques as detailed in Section 3.4.1).

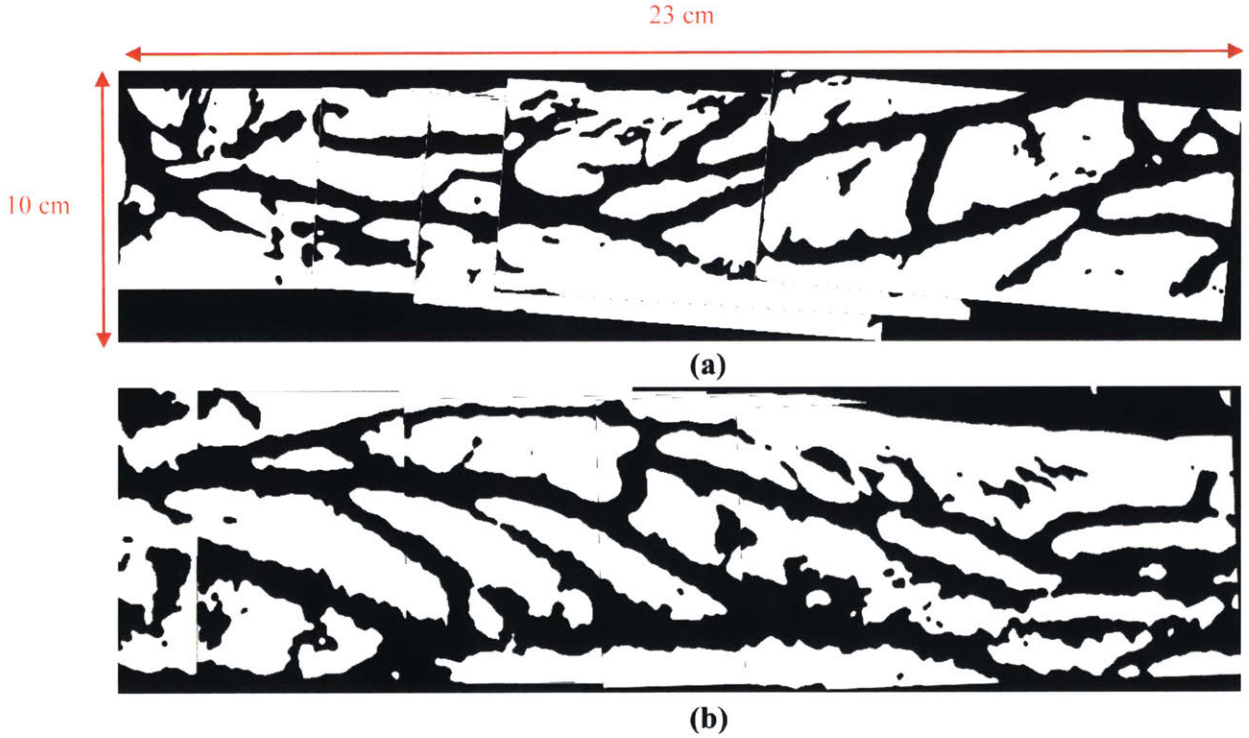

Figure 56: Vasculature Maps of the Forearm for a Pair of Identical Twins: (a) Subject 1 **(b)** Subject 2

Using the feature-based matching technique on the full vascular networks detailed in Section 3.4.1, we tried to match each sub-image (10cm x 13cm) in the map of Subject 1 to Subject 2's map and vice versa, but failed. Even when looking at the larger forearm images (i.e. the completed forearm maps of Subjects 1 and 2, 10cm x 23cm), there are not enough matching vascular features between the subjects to reliably register the two images (Figure 57). If we reduce the networks to a single line (for example, looking at only one section of a vessel between the intersection points) and disregard the differences in length, width, and angle of the vessel, we believe the veins should look similar, though it has yet to be validated.

An alternative qualitative approach is to look at the dominant directions of the superficial vascular structure for the two sets of images. The dominant directions would provide information about the way the vessels were aligned (i.e. are they parallel along the length of the arm?). However, this qualitative approach is not distinct enough as images can be rotated to have the same dominant direction. Regardless, we check the dominant directions of the vasculature in the two maps since qualitatively Subject 1 seems to have more parallel veins compared to Subject 2. By performing a Fourier transform on the entire map (thereby analyzing all images at once) and obtaining the magnitude plot, we find that the dominant directions of the vasculature of Subject 1 do not align well with the aggregate directions of the vasculature of Subject 2 (Figure 58). The pink and green lines again show areas of mismatch – the veins of Subject 2 are aligned along an angular direction from the horizontal axis of the forearm as illustrated with the green lines whereas the veins of Subject 1 are more parallel to the horizontal axis. Once again, this suggests that the vascular networks are unique amongst individuals.

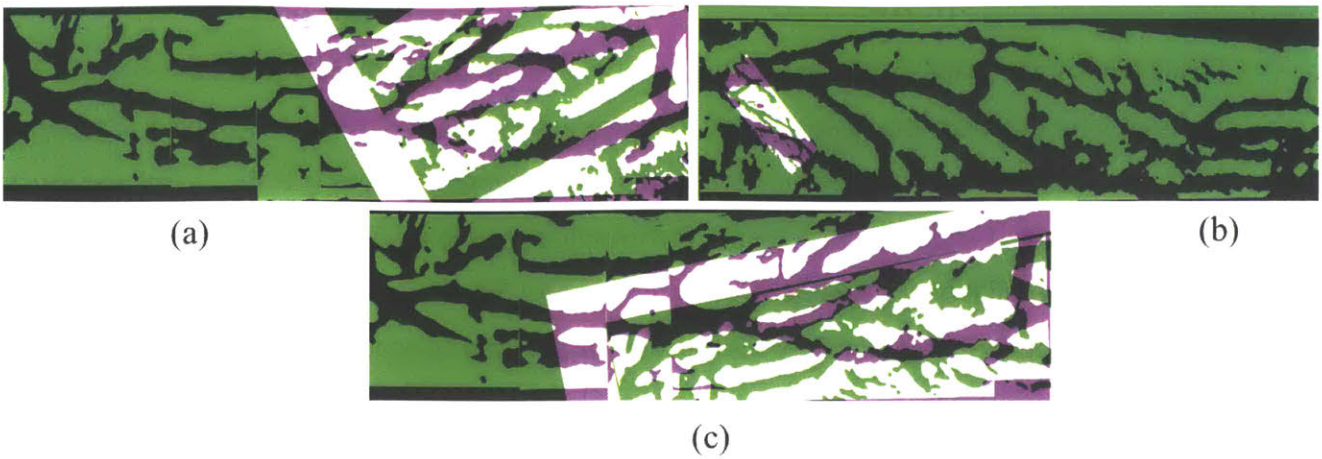

Figure 57: Demonstration of Uniqueness of Superficial Vasculature: Forearm vascular images taken from a pair of identical twins. **(a)** A failed registration attempt of an image from the forearm of Subject 1 in Subject 2's forearm stitch. **(b)** A failed registration attempt of an image from the forearm of Subject 2 in Subject 1's forearm stitch. **(c)** A failed registration attempt of the forearm of Subject 1 with the forearm of Subject 2.

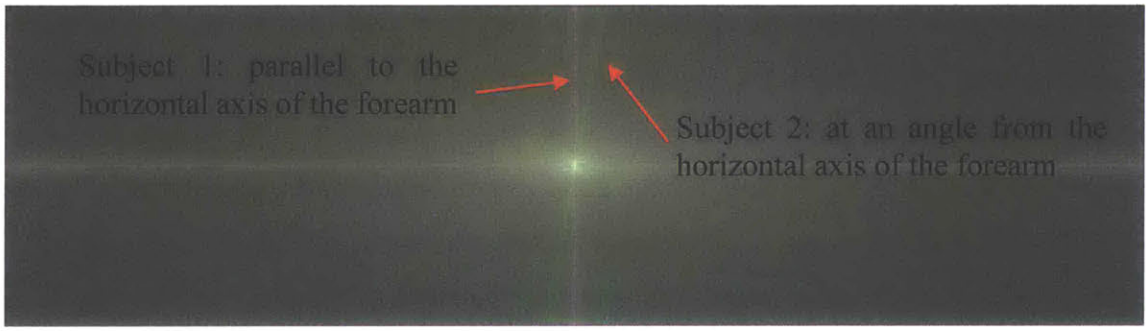

Figure 58: Magnitude Plot of Fourier Transform of Vascular Images: The aggregate directions of the vasculature between subjects 1 and 2 do not align as noticed with the lack of overlap between green and pink lines.

3.4.4.2 Quantitative Approach

Image based techniques are often not robust to viewpoint and scale changes. Thus, we attempt a qualitative approach, which reduces the vasculature to a network of nodes (process shown in Figure 59). Note that to obtain the linear network of vessels, we use morphological thinning instead of simply skeletonizing the network since the thinning process robustly reduces the thick veins into lines and branch points and can provide consistent number of branch points regardless of image scaling and viewpoint shifts (Figure 60). Branch points are the intersection and crossover points and are extracted from thinned vein networks just as junction points were extracted from skin images as described in Section 2.4.

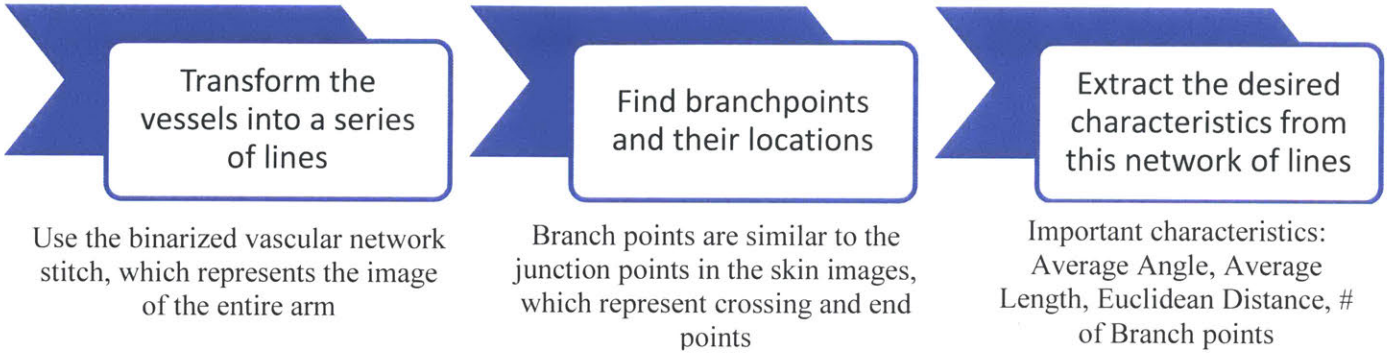

Figure 59: Process Overview to Extract Desired Features for Characterizing Vein Images

Outline for characterizing the vein networks as a series of lines and branch points:

1. Morphologically thin the binarized vein networks to get Figure 60
2. Find the number of branch points and their locations
3. Directionality, θ: find the location of each branch point with respect to the horizontal axis (Figure 61)
4. Size, l: get the distance between branch points from the known locations of branch points
5. Euclidean Distance/Smallest vessel size, l_s: get the smallest distances from Step 4
6. Spread, C: calculate the distance from a branch point to all its surrounding branch points

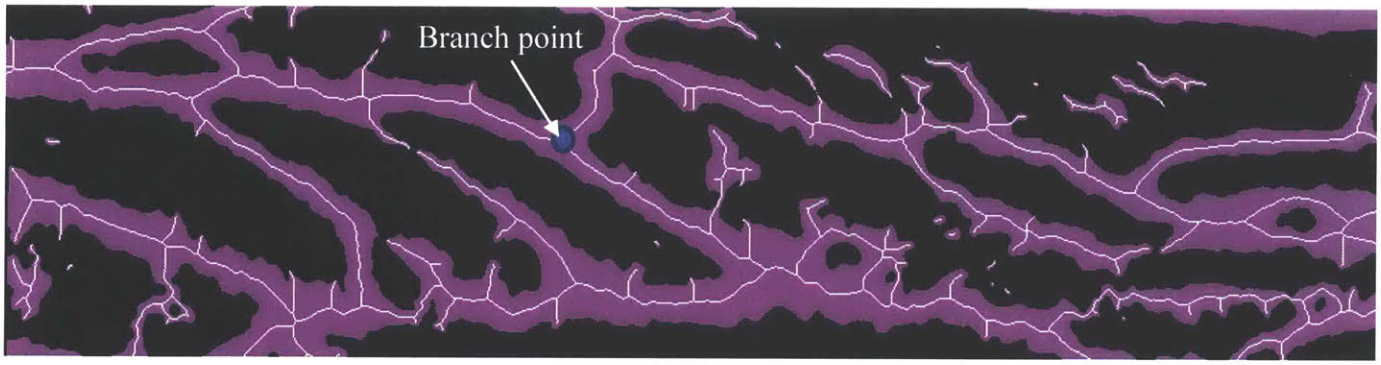

Figure 60: The forearm map of the vasculature reduced to a series of lines and branch points: The white lines in the pink background shows how the vessels are reduced to single pixel lines; the branch points of the network are the intersection and crossing points, similar to the junction points in the skin microrelief images.

Once the vessels of the forearm are reduced to a network of lines and branch points, we can analyze the network through principles of graph theory. Graph theory suggests there are a number of features that uniquely describe a network if the nodes and edges are known [80]. Since we have a distribution of branch points, we compare only certain characteristics. Specifically, we are interested in the directionality (average angular tilt of the veins, θ), size (average length of the vein segments, l), spread (size of branch point clusters, C), and expansiveness/proximity (length of smallest vessels, l_s) of the vein networks. These characteristics are summarized in Table 12 and compared for the networks of Subjects 1 and 2.

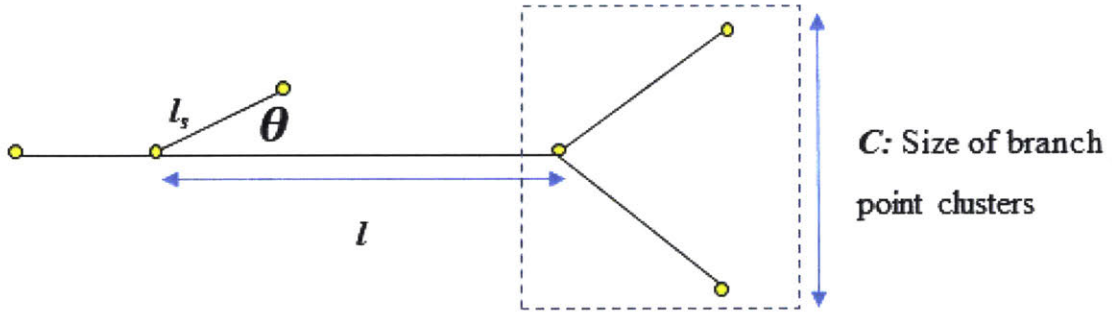

Figure 61: Characteristics Extracted from the Vein Network: The angle of the vessels with respect to the horizontal, the average length of the vein segments, the length of the smallest vessels, and the size of the branch point clusters can be extracted from the network of lines and branch points to characterize the network.

Once the networks are characterized, these characteristics can be used to determine how similar two networks are. If the networks of Figure 56 are not unique, then there should be no difference in the characteristics extracted from the networks of subjects 1 and 2 (null hypothesis).

Null Hypothesis: There is no difference in the network characteristics of Subjects 1 and 2.
Alternate Hypothesis: There is a difference in the network characteristics of Subjects 1 and 2 (i.e. the vascular networks are not the same).

Table 12 shows that most characteristics of the two networks of Figure 56 calculated with the outline above are not identical despite coming from a pair of identical twins. Using the two-sample independence t-test, we find that the null hypothesis is not supported; the networks at this scale

are actually unique despite some similarities. The average angular direction of the branches and the number of branch points are not statistically different. Given that the data comes from a pair of identical twins, it is expected there will be some similarities. However, 5 of the 6 characteristics are statistically different and we conclude that the vascular networks for the pair of identical twins are not the same. This further confirms that characterizing the networks in different ways is necessary to compare vasculature uniqueness.

Table 12: Network Characteristics for Quantifying Vasculature

Characteristic	z score	$z_{crit} = 1.64$	Accept Null?
Average Angles: direction of the branches from the horizontal midline of the arm (in aggregate)	0	<	Yes
Average Distance: average length of the branches when looking at the arm as a whole	2.17	>	No
Branch points: the location where the veins intersect or end	0	<	Yes
Euclidean Distance: shortest distance between nodes (i.e. the smallest vessels), gives the amount of branching/bifurcation in network	1.72	>	No
Diameter: size of cluster of the branch points (are the branch points close or far apart from each other?)	3.49	>	No
Center of mass: where do the vessels meet? Describes the distribution and thickness of the network	100.8	>	No

Both the qualitative and quantitative results suggest the superficial vascular structure on the body is unique among individuals. Thus, the vasculature can potentially be used as a biometric identifier and as a unique map of the body.

3.4.4.3 Future Work for Characterizing the Vasculature

Vasculature can be characterized qualitatively and quantitatively. A number of qualitative methods exist, as described above, and the robust feature matching method was pursued (Section 3.4.4.1). However, this requires proper pre-processing (i.e. no hair or visible spectrum artifacts in the binarized images). The pre-processing algorithms described in this thesis attempted to eliminate extraneous features, but some unwanted features remained in the binarized networks. Robust matching algorithms were developed to combat these errors, but the unwanted features make

qualitative network comparisons challenging. For qualitative approaches, the pre-processing must be improved to get only the vessel structures.

Quantitative methods to characterize the vasculature were also presented (Section 3.4.4.2). However, the work can be expanded for graph and network analysis as is being done with other biological networks [80]. This analysis included extracting only the branch points; a natural extension is extracting branch edges. By having information about the edge connections, we can better understand the connectivity/interaction of the network and number of pathways for each node. This will help determine if there are independent clusters separate from the main vascular network or if there are particularly dominant vessel directions (i.e. along the length of the forearm or at an angle to the horizontal from the forearm). We also need to investigate how small of a vessel patch is unique before the vascular networks of different individuals start looking the same.

3.4.5 Error Analysis

The developed algorithms have been qualitatively verified since stitching and re-localization are possible as described in earlier in this section. This means the algorithms can be used to identify relative pose of the camera with respect to the ROI as long as the camera is orthogonal to the body, the imaged regions have uniform lighting, and the binarized images have only the segmented veins for proper registration. Even with differing viewpoints or vasculature size, the extracted features on the vein images are unique enough to enable registration of the images (Sections 3.4.1 and 3.4.3). Here the algorithms are compared to a second measurement system.

Quantitative validation compares the expected position with the experimentally obtained (ground truth) position. Expected position comes from the homography matrix of the developed algorithms to get the x and y rotations and translations (see A.1 for more detail). To get the true position, a measure of ground truth is required. Here, the OptiTrak Trio (NaturalPoint,Inc., OR) is used for ground truth; with sub-millimeter accuracy (0.0001cm resolution), it is assumed to be error free. The OptiTrak Trio is a 6 degrees of freedom optical tracking system; it comes with three cameras and an accompanying software (Motive) that outputs the rotation around and translation in the x, y, and z axes. The experimental setup to use the OptiTrak Trio in conjunction with the developed device is shown in Figure 62 and the generated output for one scan along the forearm is shown in Figure 63. To get the relative position for a single image, the (x, y, z) coordinates of the desired image are subtracted from the (x, y, z) coordinates of the initial image, which is the

camera motion in all three axes and can be used to compare to the homography output from the algorithms.

It is important to note that the expected position from the algorithms (i.e. the homography matrix) is 2D and the true position from the OptiTrak is 3D, so we must analyze the data accordingly (Equation 4 and Equation 5). This is because the homography matrix can only show (x,y) position by definition; any z motion is captured in the xy plane, since the homography predicts 2D projection only. The homography provides the pixel transformations in the x and y directions (last column of the homography matrix as shown in Table 13). Using the resolution (0.01cm/pixel), the motion in physical units is calculated.

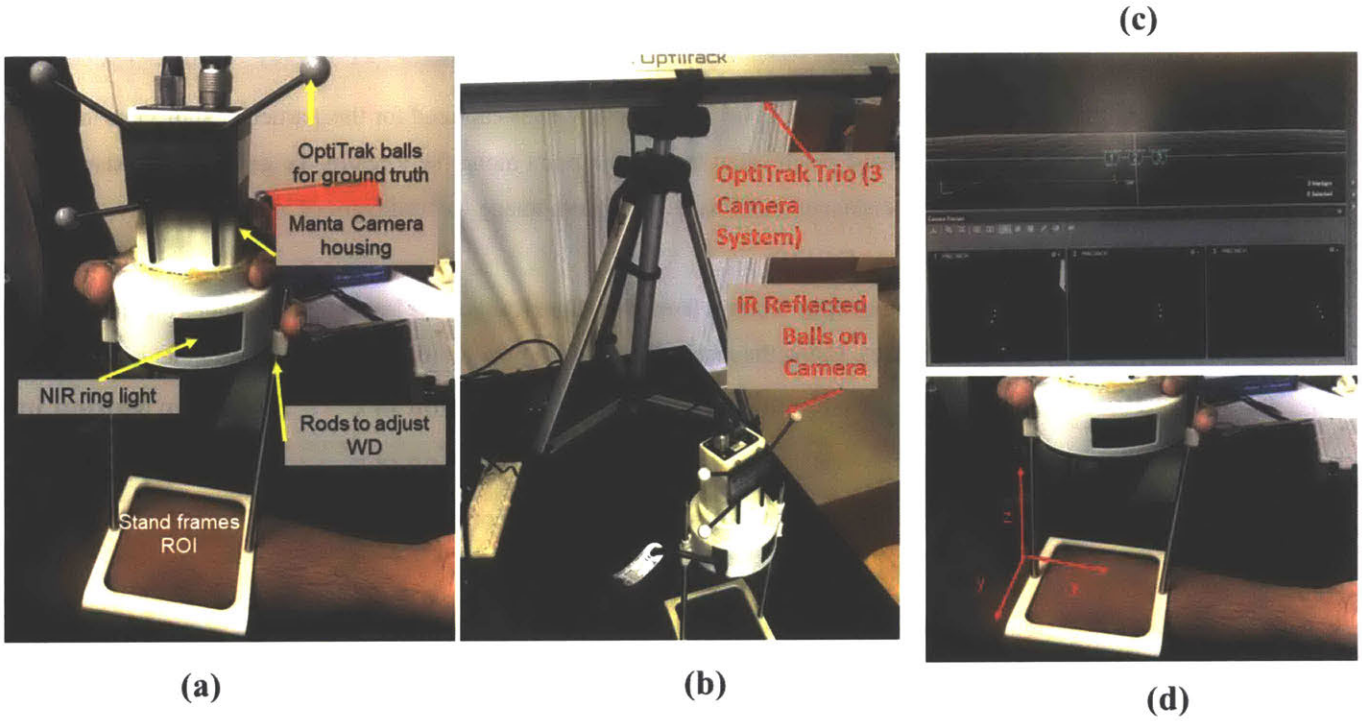

Figure 62: OptiTrak Setup for Determining Ground Truth: (a) The experimental process is the same as described in Section 3.2 with the device orthogonal to the ROI. **(b)** The OptiTrak Trio looks at the IR reflective balls, which are placed on the camera to track camera motion. **(c)** Motive (OptiTrak's accompanying software) looks at the motion of the 3 balls through the 3 cameras. **(d)** The camera oriented along the ROI: x is along the scan direction, y is the width of the scan region, and z is the distance of the ROI from the camera.

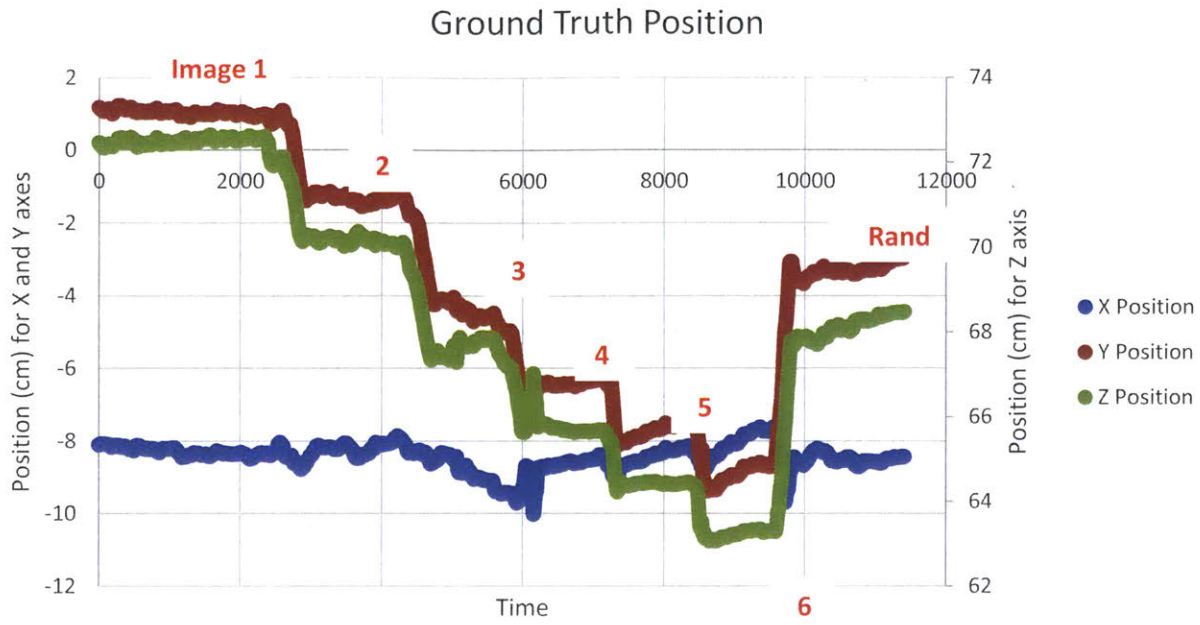

Figure 63: Output from the OptiTrak Trio: There are 6 images captured for this particular subject as labeled with "Rand" indicating the small image patch taken from some point along the forearm. To get the true distance, we use the coordinates of the relative distance (coordinates of random image – coordinates of image 1).

Table 13: Output of the Homography Matrix from the Algorithms: The last column provides the linear motion in the x and y axes with pixel values. Using the resolution (0.01cm/pixel), the motion in physical units is calculated.

Rotation in x	Rotation in y	Rotation in z	**Linear Motion in x**
Rotation in x	Rotation in y	Rotation in z	**Linear Motion in y**
Rotation in x	Rotation in y	Rotation in z	**1**

Equation 4: Calculating the Expected Distance from 2D Homography

$$Expected\ Distance = \sqrt{x^2 + y^2}$$

Equation 5: Calculating the True Distance from the OptiTrak Output

$$True\ Distance = \sqrt{x^2 + y^2 + z^2}$$

Equation 6: Calculating Percent Error between the Homography and OptiTrak Predicted Positions

$$Percent\ Error = \frac{|Expected\ Distance - True\ Distance|}{True\ Distance} \times 100$$

However, z motion is still captured with the homography matrix despite only 2D output. This is because there is always a projection of the z axis onto the xy plane. Consider moving the camera 1.5cm purely in the z direction (i.e. away from the arm). The last column of the homography matrix should be [0; 0; 1] since there was no xy motion. However, we get the final column to be [value; value; 1]. The first entry in the final column of the homography matrix (linear x motion shown in Table 13) captures the x translation and the projection of z motion onto the x axis; the second entry in the final column of the homography matrix (linear y motion shown in Table 13) captures the y translation and the projection of z motion onto the y axis. So we see that moving further from the ROI (i.e. a shift in the z axis) can be represented as a change in (x,y) coordinates and captured by the homography matrix.

Despite not independently capturing the true z, the algorithms can still pick out and align salient features of the vascular network. For each subject, we scan along the forearm and acquire a small image region at a random point in the forearm with the OptiTrak measuring camera position as shown in Figure 62. We then calculate the expected and true distances the camera moved by using Equation 4 and Equation 5. To get the percent errors, we use Equation 6. For one forearm scan on a particular subject, the errors are tabulated in Table 14. Note that there is some inherent error in obtaining the true motion from the OptiTrak - it is difficult to figure out relative motion precisely; given the high frame rate of the OptiTrak, there are nearly 16k points per scan, which have to be manually sorted to determine the location of each image capture.

Table 14: Error between Predicted (Developed Algorithms) and True (OptiTrak) Motion

Motion Axis	Expected Motion	True Motion	Percent Error [%]
Along Arm (x)	2.779 cm	2.956 cm	5.98
Arm Curvature	0.348 rad	0.367 rad	5.34
Rotation about z	1.066 deg	1.849 deg	73.47
Rotation about y	0	5.1 deg	-
Rotation about x	0	0.09 deg	-

3.4.5.1 Discussion about the Errors along the Axes

There are a few axes about which the expected and true motions are significant. To understand the axes orientations, refer to Figure 62. Most important is the translation in x (scan direction), since this is the axis of interest for the experiments. All rotations result from the experimental scanning

process while the camera moves along the scan direction. Rotation about the x axis signifies the camera is not moving in a straight line along the arm. y axis rotations result from the camera not being perfectly perpendicular to the scan region during the scan, which could result from experimenter error (not keeping the camera perfectly perpendicular) or from the camera cable pulling on the camera during the image collection. Lastly, rotation about the z axis captures the friction between the device and the forearm during translation.

The percent error for translation is less than 10%. A potential explanation for this error is the 3D arm curvature. To keep the ROI in focus and compensate for the arm curvature, the camera adjusts along the z axis. However, the homography matrix assumes a 2D, flat scene as described previously and assumes all motion occurs only in the xy plane. This is verified noticing that the percent error for the arm curvature is approximately equal to translational x error as predicted with the homography. Note that the error resulting from arm curvature was measured.

The rotation errors are significantly larger and explained here. Given that the arm is not frictionless, some rotation about z is expected during a scan. Although the percent error initially seems large, the motion itself is so small that the error for rotation about z is acceptable (~73% error for a ~2° measurement).

The percent errors for rotations about x and y are undefined because the homography expects no motion. This is a valid assumption for rotation about x, since the ring stand forces the device flush against the arm. The true 0.09° motion tabulated could result if the camera was not flush against the arm during the image acquisition, which is possible because of the friction between the arm and device. Thus, the 0.09° true rotation in x is acceptable. The homography assumption that the y axis rotation is zero is incorrect. Ideally, there should be no rotation and the camera should always be perpendicular to the ROI, but experimentally some rotation about y is expected since external forces act on the camera (i.e. cable pulling on camera and investigator moving the camera in freehand motion). Besides knowing that some nonzero rotation is expected, there is no way to know if the true motion is acceptable. However, the sources of error from the OptiTrak output described above and the relatively small magnitude of the rotation (5° is relatively small compared when considering the large potential range of motion), the y rotation is deemed acceptable. Further experiments (i.e. different investigators to keep the ROI perpendicular or a lighter camera to PC Ethernet cable to prevent the cable pulling on the camera) may be carried out and the average true motion captured to see if a smaller rotation is possible.

A note about the homography values: Although the expected motion values are reported to the same accuracy as the OptiTrak, homography values are not as precise as the sub-millimeter accuracy of the OptiTrak. This reduced accuracy is due to machine precision and 2D limitations of the homography. Additionally, the high resolution of the Manta camera far exceeds the motions that the homography can predict, so the homography predictions are not exact. Since the OptiTrak values are also not exact (as described above), the reported percent errors must be taken cautiously. Lastly, it is known that homographies have increased uncertainty for large image sequences, as is the case here [81]. Thus, the true values are within uncertainty, not error, and the deviations are acceptable.

3.4.6 Characterizing the Overall System

Section 3.4.5 showcases the error of the algorithms. However, the handheld device has been designed and developed to be used over time and for a variety of individuals, so the system must be characterized for this use case. We obtain 15 subjects of different genders with various skin tones and workout habits/muscle definition for subject diversity (information obtained through a questionnaire during consent). Imaging these 15 subjects serially gives the registration errors per individual. The imaging is carried out 3 times per individual on the same day as described in Section 3.2, with the OptiTrak tracking ground truth motion. To understand if there is a significant difference in finding a small image patch within a larger forearm map (i.e. device performance) based on individual characteristics, the ANOVA test is used on the registration errors per individual. At 95% confidence, $p = 0.3621 > 0.05$, so we ascertain there is no significant difference in the errors from the homography prediction of camera location compared to the true camera location (from the OptiTrak) (i.e. no difference in registration errors). In other words, the performance of the imaging system (comprised of device and algorithms) is the same despite subject variation in gender, ethnicity, workout habits, and other variables affecting vein performance.

We average the registration errors to get the overall system error after determining the system performance is the same across subjects. Thus, for controlled rectilinear image capture, the system can robustly image a variety of individuals and find a position on the body within 5% error (or 0.22cm of true position). Any angular shifts are obtained within 3% error. This characterization is

for the short term (same day imaging); long-term monitoring of these subjects would be required to characterize the errors over time.

3.5 Summary of Vein Imaging Work

Considering clinical and technical requirements, a NIR imaging system was designed. It is a low-cost, lightweight, and easy-to-use system that can image the underlying vascular structure across large areas of the human body. Given its portability, it can easily be integrated into clinics. The experimental procedure and device design enable repeatable image capture, which is necessary to study the stability of the vasculature over time. Algorithms were developed to extract and analyze the superficial vein structure; the robustness of the overall system was tested and the deviations quantified.

Non-invasively imaging veins has many applications: from understanding the state of hydration levels to being used as a form of identification. The developed hardware and algorithms allow further exploration and deeper understanding of the vasculature (i.e. vein structure stability over time and uniqueness across the body and amongst individuals). Primarily, the system allows us to characterize normal blood vessel variation in healthy individuals over time. Quantifying changes in vasculature over time may prove to be a useful tool for early diagnosis of venous disease (i.e. DVT and strokes are caused by blood clots). Additionally, using salient features of the vascular network, we were able to register images onto a vein map of the arm over a period of eight months, suggesting the vasculature is stable and can be used for re-localization. In other words, we can find a location on the body by looking at the underlying vein structure. Finally, a variety of methods, both qualitative and quantitative, were described to characterize the superficial vascular structure in an individual. Using feature matching techniques and network-node analysis to analyze the superficial veins on a pair of identical twins, we started demonstrating the uniqueness of the vasculature and its potential use as a biometric.

3.5.1 Limitations of Current System

The designed system (hardware and algorithms) has been tested and validated for imaging the superficial veins. For linear motion and rotation along a single plane, the system can correctly identify the location on the body within 5% error. Even with small out-of-plane rotations, the system can correctly identify the location on the body (Figure 64).

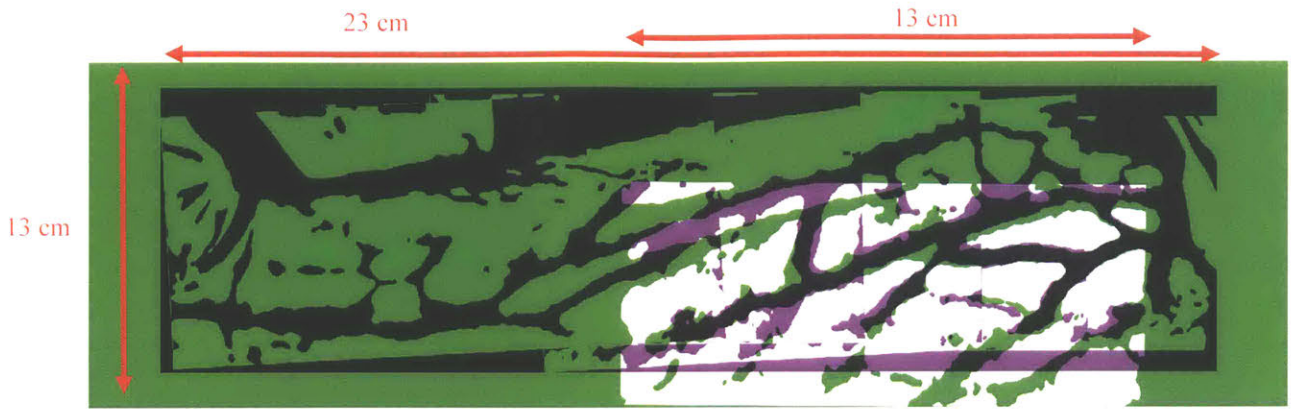

Figure 64: Random Image Correctly Positioned after Rotating and Translating the Arm: Controlled experimentation to showcase the current limitations of the algorithm and hardware setup given that the body is 3D. However, we are still able to find the image within a larger image patch.

However, the system is unable to retain stability under excessive 3D rotations (i.e. arm rotations greater than 30°). Since the computer cannot distinguish between rotations and translation, many small out-of-plane rotations are seen as many small linear translations (Figure 65). Thus, two cameras are required to get depth information (i.e. true curvature).

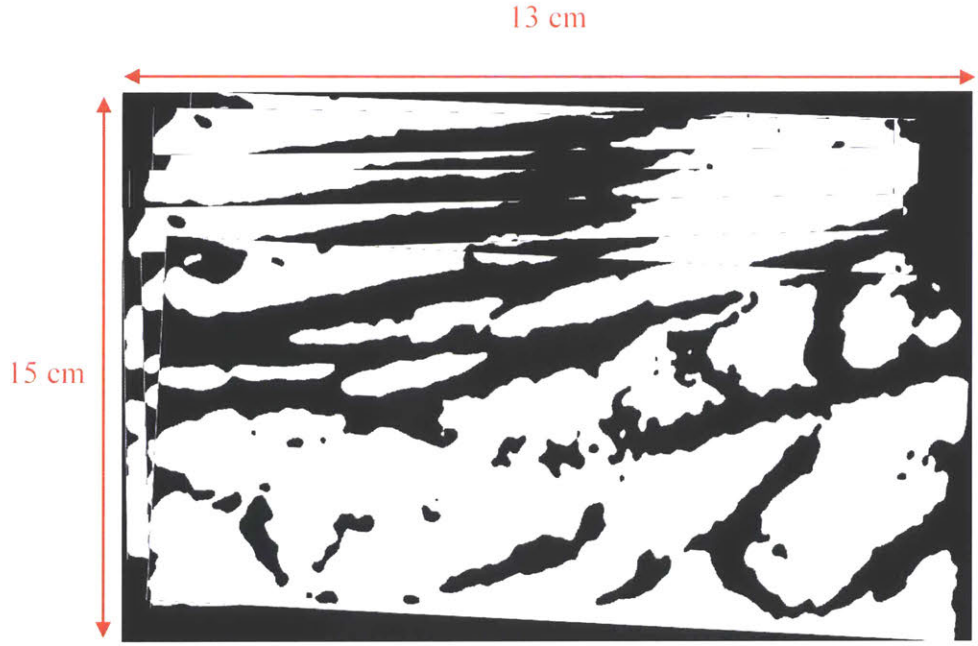

Figure 65: Drawback of One Camera System to Detect Curvature: Multiple images of small angle rotations of the forearm stitched together are seen as many small linear translations rather than small angle rotations. Therefore, to "unwrap" the human limb, we would need two cameras to understand true curvature, rather than the one camera system we have designed.

3.5.2 Future Work

Presented here was the experimental process and analysis of forearm vasculature; an obvious extension is imaging the superficial veins across other areas of the body (i.e. bicep/upper arm and legs) and understanding the vascular variation across the body. Some preliminary image acquisition on the hamstrings and biceps are shown in Figure 66.

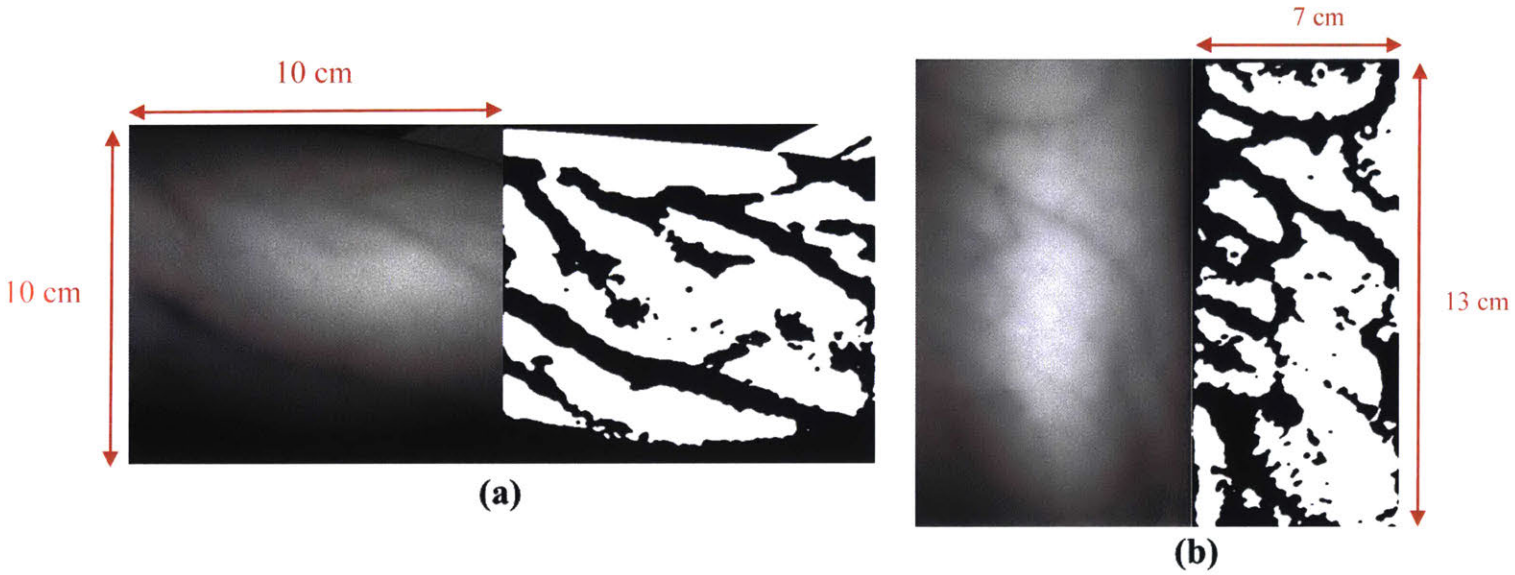

Figure 66: Sample Images and Vein Extractions of Other Parts of the Body: **(a)** The biceps **(b)** The hamstrings

Note that the binarized images in Figure 66 have more high frequency noise than those of the forearm (Figure 41), due in part to the parameters selected for the extraction. Although the vascular network is not extremely prominent in these images, they serve as a first demonstration for the possibility of imaging and extracting the vasculature in other areas of the body. The vasculature in other parts of the body are still recognizable and can be extracted with the existing camera and algorithms. For a cleaner extraction of these slightly deeper vessels, the parameters for filtering and image enhancement (i.e. size of median filters and σ's for DoG) in the pre-processing code would need to be fine-tuned.

The resolution and magnification of the developed device can image veins at a depth of ~1cm. A future direction may be to image the smaller capillaries (responsible for nutrient transport) or the deeper veins by using either an increased magnification lens, a more powerful light source, or imaging at a different wavelength. Although capillaries are not as clinically significant as the veins, the ability to image the capillaries is a more interesting scientific question as we try to push the

limits of optical imaging systems and try to generate a full vessel map of the body (deep veins, capillaries, superficial veins, and arteries). By imaging the capillaries, superficial veins, and deep veins, we can better understand the first layer of the human body.

CHAPTER

4

CONCLUSIONS AND FUTURE WORK

Non-invasive imaging of the human skin and vein structures has many clinical and scientific applications. By studying the evolution of skin and vein networks over time, we can better understand disease progression and gain insight into the overall health of an individual. The uniqueness of these networks can also be applied as a more secure biometric identifier (compared to existing fingerprints). Finally, the long-term stability of these structures allows them to be used as a body positioning system.

4.1 Skin and Vein Network Commonalities

This work focused on the hardware and software developed to image the skin microrelief and vein structures, particularly looking at the stability of healthy skin and veins for applications in using these biological networks for feature-based body registration algorithms. We recognized that these networks are not disparate; rather, the challenges associated with imaging and analyzing the networks are the same. As such, we came up with similar solutions fine-tuned for the features of different length scales. We found that both skin and veins were biological networks from which features could be extracted for analysis. Both required a series of image processing steps that were similar: (1) pre-process raw images to get the networks and (2) find unique features in the network for aligning two images.

Assuming both sets of images are pre-processed optimally, we see that the two networks are texturally similar; they both consist of a network of quadrangles and triangles that are formed by junction points and edges. When normalized to the same length scale, there are no discernable differences in processing the skin microrelief and vein images; we always look for unique feature points that can be extracted and matched from the geometrical network as discussed in Sections

2.4 and 3.3. This processing and matching procedure can therefore be used for any network with lines (edges) and intersection points (junction/branch points).

However, in practice, there were some noticeable differences between the two networks. Imaging the skin microrelief (millimeter scale) requires much higher resolution, whereas imaging the veins (centimeter scale) requires a higher FOV since the features are different length scales; this drives the camera selection and working distance parameters. Veins are more prominent in the IR region, since blood absorbs IR light and surrounding tissue reflects it, providing greater contrast between skin and veins. The microreliefs are shallow on the skin surface; we rely on the light source and camera resolution to capture the contrast (Figure 67). Because of the lower contrast for microrelief images, pre-processing is more challenging for skin microrelief images than for veins. Finally, since the experimental microrelief images are very small and more images are required for the same region of interest, stitching the individual images together to get a map is computationally expensive; stitching the vein images is less challenging since the images are physically an order of magnitude larger. These considerations were incorporated into the final design of the devices as seen in Figure 68. Some important metrics are compared in Table 15.

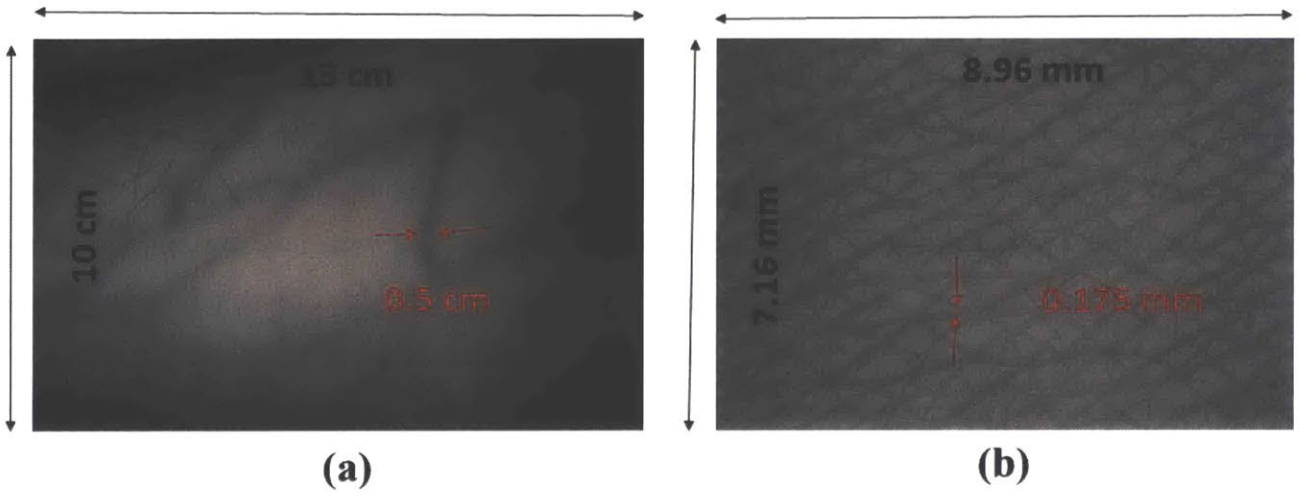

Figure 67: Experimental Images of Skin and Veins with Dimensions Provided: (a) Vein images are larger and the features are more prominent because of greater contrast between the veins and surrounding skin **(b)** Skin images are smaller in size and features are less prominent because of the limited contrast between shallow microrelief and skin.

Table 15: Skin and Vein Devices Compared

	Working Distance (cm)	Resolution (μm/pixel)	Field of View (cm, in)
Skin Device	6.8	26.6	5.3 x 5.3 (2.1 x 2.1)
Vein Device	17.78	100	13.6 x 6.9 (5.4 x 2.7)

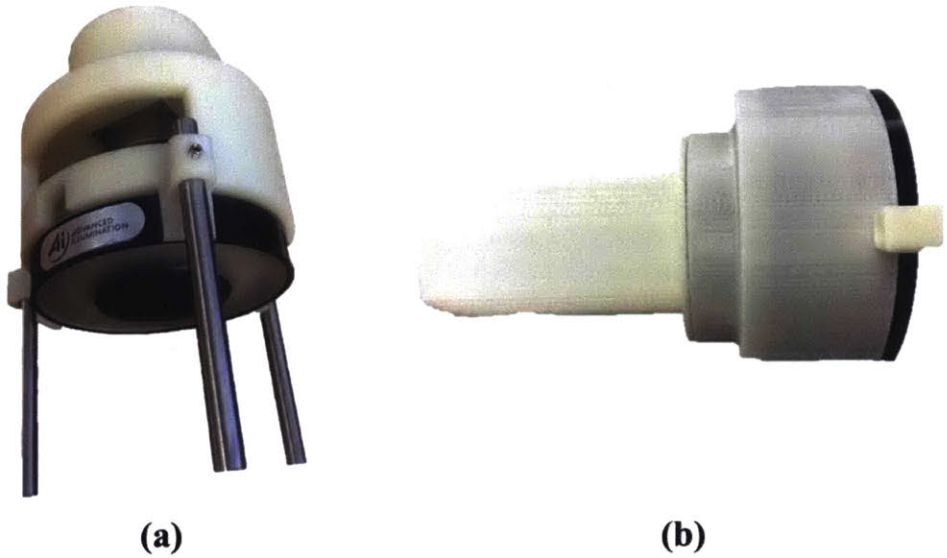

(a) **(b)**

Figure 68: Skin and Vein Imaging Devices: (a) Skin microrelief imaging device **(b)** Vein imaging device. Both are handheld and comprise of a camera, light source, and housing fixture.

The devices and algorithms developed contribute to the scientific, clinical, and technical communities. From the scientific viewpoint, we have a better understanding of how the skin and vein networks are connected. The microrelief system alone enables us to study the evolution of healthy skin in individuals over time, looking specifically at adults and children and the longitudinal stability of this localized skin structure over time. Similarly, the vein imaging system allows us to study the longitudinal stability of localized vasculature and potentially use the vein networks in other parts of the body as a biometric. Clinically, the microreliefs and vascular networks can be used as a body positioning system that could help with post-operative care and monitoring disease progression. Structural changes in the networks can help diagnose various diseases non-invasively. Finally, from the technology standpoint, we created multi-modal

handheld, high resolution imaging systems that are light invariant and can easily be integrated into clinics. These systems are comprised of hardware and algorithms fine-tuned to study the features of interest. They are also modular and minor design changes can be made to be useful in various other applications as discussed in Sections 2.6.2 and 3.5.2.

4.2 Future Work

With the current systems, we have shown that the biologic features on the human body are stable over time and can be used as a body positioning system, especially on the limbs. Naturally, the obvious extension is mapping across the entire body to get the full body map. Furthermore, 3D reconstructions of human organs or other limbs are possible with multi-modal imaging and by using local features for position tracking.

4.2.1 Future Design Changes

Studying the skin and vein structures does not end here. While this thesis lays the technical foundation for imaging and studying biological networks on and below the skin surface, more design iterations can greatly impact the clinical usability. As we move towards a digital and miniaturized age, the imaging systems should be incorporated into an even smaller form factor (like current cell phone cameras). With the appropriate magnification and filter attachments, the millimeter scale microreliefs and subdermal veins are visible, as is seen with current experimentation. Incorporating the two modalities into one imaging device presents a technical challenge as the features on the veins and skin are of different length scales and therefore have different imaging requirements. Furthermore, image processing two imaging modalities simultaneously requires nontrivial registration techniques. However, one device would enable a better understanding of the vein and skin connection and perhaps permit earlier diagnosis of various health conditions.

4.2.2 Future Experiments

The diagnostic capabilities of the biological networks can be further explored with controlled experimentation. Weight lifting and caffeine affects vein prominence as anyone who has gone to the gym or had a cup of coffee can attest to; however, these effects have not been quantified in existing literature. Our developed systems have the resolution and capability of quantifying the

vascular changes, but time constraints prevented carrying out these experiments. Finally, we come to the long-term monitoring of individuals, which is one of the original goals of this research. The changing nature of laboratory personnel permitted us to follow individuals for 2 years at most. Without these constraints, we can understand the longer stability of the skin and vein structures.

4.2.3 Improved Biological Understanding

Although there are a number of imaging and processing techniques for the skin microrelief and superficial vascular networks, their structural formation and change is lesser known. Preliminary experimentation found that microreliefs are not visible when there are moles, which suggests there is a cellular or structural change that occurs in the microrelief prior to freckle/mole formation. This could be verified by imaging at-risk individuals consistently and noticing changes in the micrometer scale features. By doing this, we could potentially predict a mole formation before it becomes apparent to the naked eye. Additionally, if the structural changes for the skin cancerous lesions are different than for benign moles, then we could potentially diagnose skin cancer earlier than conventional methods by looking at the *type* of structural change in the microrelief pattern.

The importance of the vasculature for health is much less contested. However, even so, the significance of the superficial vasculature is less widely known. Veins help transport blood throughout the body; for subjects with excessively cold hands and feed, we suspect poor circulation. If we can understand the normal structure of the superficial vascular network for transporting blood throughout the body, we may better understand when cold extremities are a medical concern. Additionally, since the superficial veins feed into the deep veins, we suspect the structural changes in these superficial veins will mirror those of the deep veins. This could be potentially useful for early diagnosis of various vascular conditions (i.e. DVT). Both these applications would require further experimental verification to understand the connection between the deep vein and superficial vein structures and their variation for human health.

Despite the various avenues for future directions, the applications of the current work are far-reaching: from clinicians, who are interested in the diagnostic and reconstruction applications, to the cosmetics industry, which is focused more on anti-aging skin health and hydration. With continued iterations of the mechanical structure and optical hardware, and improved computational efficiency, the effects of this work can have significant repercussions.

REFERENCES

[1] J. Sun *et al.*, "Reflectance of human skin using colour photometric stereo: with particular application to pigmented lesion analysis," *Ski. Res. Technol.*, vol. 14, no. 2, pp. 173–179, May 2008.

[2] P. C. Valery, R. Neale, G. Williams, N. Pandeya, G. Siller, and A. Green, "The Effect of Skin Examination Surveys on the Incidence of Basal Cell Carcinoma in a Queensland Community Sample: A 10-Year Longitudinal Study," *J. Investig. Dermatology Symp. Proc.*, vol. 9, no. 2, pp. 148–151, Mar. 2004.

[3] O. G. Cula, K. J. Dana, F. P. Murphy, and B. K. Rao, "Bidirectional Imaging and Modeling of Skin Texture," *IEEE Trans. Biomed. Eng.*, vol. 51, no. 12, pp. 2148–2159, Dec. 2004.

[4] Research Areas Innovation, "Measurement / Visualization Technology," *Shiseido*, 2015. [Online]. Available: https://www.shiseidogroup.com/rd/development/measurement.html. [Accessed: 23-May-2018].

[5] L. Li *et al.*, "Age-related changes in skin topography and microcirculation," *Arch. Dermatol. Res.*, vol. 297, no. 9, pp. 412–416, Mar. 2006.

[6] Y. Zou, E. Song, and R. Jin, "Age-dependent changes in skin surface assessed by a novel two-dimensional image analysis," *Ski. Res. Technol.*, vol. 15, no. 4, pp. 399–406, Nov. 2009.

[7] C. Piérard-Franchimont, F. Cornil, J. Dehavay, F. Deleixhe-Mauhin, B. Letot, and G. . Piérard, "Climacteric skin ageing of the face—a prospective longitudinal comparative trial on the effect of oral hormone replacement therapy," *Maturitas*, vol. 32, no. 2, pp. 87–93, Jun. 1999.

[8] J. M. Waller and H. I. Maibach, "Age and skin structure and function, a quantitative approach (I): blood flow, pH, thickness, and ultrasound echogenicity," *Ski. Res. Technol.*, vol. 11, no. 4, pp. 221–235, Nov. 2005.

[9] I. Kundu, J. Beaudoin, X. Du, and B. W. Anthony, "Skin Registration and Analysis of Microrelief Structure," in *MEDRC*, 2017.

[10] G. E. Pierard, I. Uhoda, and C. Pierard-Franchimont, "From skin microrelief to wrinkles. An area ripe for investigation," *J. Cosmet. Dermatol.*, vol. 2, no. 1, pp. 21–28, Jan. 2003.

[11] K.-P. Wilhelm, *Bioengineering of the skin : skin imaging and analysis*. Informa Healthcare, 2007.

[12] M. Setaro and A. Sparavigna, "Irregularity skin index (ISI): a tool to evaluate skin surface texture.," *Skin Res. Technol.*, vol. 7, no. 3, pp. 159–63, Aug. 2001.

[13] O. G. Cula, K. J. Dana, F. P. Murphy, and B. K. Rao, "Skin Texture Modeling," *Int. J. Comput. Vis.*, vol. 62, no. 1–2, pp. 97–119, Apr. 2005.

[14] A. Barel *et al.*, "Effect of oral intake of choline-stabilized orthosilicic acid on skin, nails and hair in women with photodamaged skin," *Arch. Dermatol. Res.*, vol. 297, no. 4, pp. 147–153, Oct. 2005.

[15] "Skin-Visiometer® SV 700 USB," *Courage - Khazaka Electronic*, 2004. [Online]. Available: http://www.courage-khazaka.de/index.php/en/products/scientific/142-visiometer. [Accessed: 23-May-2018].

[16] I. A. Kundu, "Imaging platforms for detecting and analyzing skin features and Its stability : with applications in skin health and in using the skin as a body-relative position-encoding system," 2015.

[17] S. Yoon and A. K. Jain, "Longitudinal study of fingerprint recognition.," *Proc. Natl. Acad. Sci. U. S. A.*, vol. 112, no. 28, pp. 8555–60, Jul. 2015.
[18] C. N. E. Anagnostopoulos, D. D. Vergados, and P. Mintzias, "Image registration of follow-up examinations in digital dermoscopy," in *13th IEEE International Conference on BioInformatics and BioEngineering*, 2013, pp. 1–4.
[19] S. Belongie, J. Malik, and J. Puzicha, "Shape matching and object recognition using shape contexts," *IEEE Trans. Pattern Anal. Mach. Intell.*, vol. 24, no. 4, pp. 509–522, Apr. 2002.
[20] S. Zambanini, G. Langs, R. Sablatnig, and H. Maier, "Automatic Robust Registration of Cutaneous Hemangiomas for Follow-up Examinations 1)."
[21] S. Madan, K. J. Dana, and G. O. Cula, "Multimodal and time-lapse skin registration," *Ski. Res. Technol.*, vol. 21, no. 3, pp. 319–326, Aug. 2015.
[22] J. Mahmud, C. A. Holt, and S. L. Evans, "An innovative application of a small-scale motion analysis technique to quantify human skin deformation in vivo," *J. Biomech.*, vol. 43, no. 5, pp. 1002–1006, Mar. 2010.
[23] X. Du, B. W. Anthony, and N. C. Kojimoto, "Grid-based matching for full-field large-area deformation measurement," *Opt. Lasers Eng.*, vol. 66, pp. 307–319, Mar. 2015.
[24] National Institute on Aging, "Heart Health," *NIH*, 2018. [Online]. Available: https://www.nia.nih.gov/health/heart-health. [Accessed: 23-May-2018].
[25] "Vascular Imaging," *ThermoFisher*. [Online]. Available: https://www.thermofisher.com/us/en/home/life-science/cell-analysis/cellular-imaging/small-animal-in-vivo-imaging-saivi/vascular-imaging.html. [Accessed: 23-May-2018].
[26] M. Attas, T. Posthumus, B. Schattka, M. Sowa, H. Mantsch, and S. Zhang, "Long-wavelength near-infrared spectroscopic imaging for in-vivo skin hydration measurements," *Vib. Spectrosc.*, vol. 28, no. 1, pp. 37–43, Feb. 2002.
[27] I. V Meglinski and S. J. Matcher, "Quantitative assessment of skin layers absorption and skin reflectance spectra simulation in the visible and near-infrared spectral regions.," *Physiol. Meas.*, vol. 23, no. 4, pp. 741–53, Nov. 2002.
[28] "Cardiac and Vascular Surgery," *Ascension*, 2018. [Online]. Available: https://ascension.org/Our-Work. [Accessed: 23-May-2018].
[29] "Vein Matching," *Wikipedia*, 2018. [Online]. Available: https://en.wikipedia.org/wiki/Vein_matching.
[30] E. A. V. Jones, F. le Noble, and A. Eichmann, "What Determines Blood Vessel Structure? Genetic Prespecification vs. Hemodynamics," *Physiology*, vol. 21, no. 6, pp. 388–395, Dec. 2006.
[31] J. R. Ryder *et al.*, "Heritability of Vascular Structure and Function: A Parent-Child Study.," *J. Am. Heart Assoc.*, vol. 6, no. 2, p. e004757, Feb. 2017.
[32] M. H. Meissner, "Lower extremity venous anatomy.," *Semin. Intervent. Radiol.*, vol. 22, no. 3, pp. 147–56, Sep. 2005.
[33] J. Raffetto and A. Schmaier, "VA Medical Center." West Roxbury, MA.
[34] N. Bouzida, A. H. Bendada, and X. P. Maldague, "Near-infrared image formation and processing for the extraction of hand veins," *J. Mod. Opt.*, vol. 57, no. 18, pp. 1731–1737, Oct. 2010.
[35] N. Labropoulos, K. L. Summers, I. E. Sanchez, and J. Raffetto, "Saphenous vein wall thickness in age and venous reflux-associated remodeling in adults," *J. Vasc. Surg. Venous Lymphat. Disord.*, vol. 5, no. 2, pp. 216–223, Mar. 2017.

[36] Lee Dubay, "Near-infrared camera enables real-time, accurate vein procedures - BioOptics World," *BioOptics World*, 2014. [Online]. Available: https://www.bioopticsworld.com/articles/2014/06/near-infrared-camera-enables-real-time-accurate-vein-procedures.html. [Accessed: 23-May-2018].
[37] K. Orlick, "Interview with AZ Dermatologist." Tucson, AZ.
[38] M. Porter, "Interview with BIDMC Dermatologist." Cambridge, MA.
[39] A. Shrotri, S. C. Rethrekar, M. H. Patil, D. Bhattacharyya, and T. Kim, "Infrared Imaging of Hand Vein Patterns for Biometric Purposes," *J. Secur. Eng.*, pp. 57–66, 2009.
[40] L. Wang and G. Leedham, "Near- and Far- Infrared Imaging for Vein Pattern Biometrics," in *2006 IEEE International Conference on Video and Signal Based Surveillance*, 2006, pp. 52–52.
[41] I. Khan, "Vein Pattern Recognition - Biometrics Underneath the Skin," *Frost & Sullivan Market Insight*, 2006. [Online]. Available: https://www.frost.com/prod/servlet/market-insight-print.pag?docid=86268767. [Accessed: 30-May-2018].
[42] "Superficial vein," *Wikipedia*, 2018. [Online]. Available: https://en.wikipedia.org/wiki/Superficial_vein. [Accessed: 23-May-2018].
[43] SummitSkin, "The Function of Veins, and Their Role in the Human Body," *Summit: Skin and Vein Care*, 2013. [Online]. Available: https://www.summitskinandveincare.com/veins/veins-their-function-and-importance/. [Accessed: 23-May-2018].
[44] "Blood Vessel Structure and Function | Boundless Anatomy and Physiology," *LumenCandela*. [Online]. Available: https://courses.lumenlearning.com/boundless-ap/chapter/blood-vessel-structure-and-function/. [Accessed: 23-May-2018].
[45] S. Gioux, H. S. Choi, and J. V Frangioni, "Image-guided surgery using invisible near-infrared light: fundamentals of clinical translation.," *Mol. Imaging*, vol. 9, no. 5, pp. 237–55, Oct. 2010.
[46] G. Hong *et al.*, "Multifunctional in vivo vascular imaging using near-infrared II fluorescence," *Nat. Med.*, vol. 18, no. 12, pp. 1841–1846, Dec. 2012.
[47] R. K. MIYAKE *et al.*, "Vein Imaging: A New Method of Near Infrared Imaging, Where a Processed Image Is Projected onto the Skin for the Enhancement of Vein Treatment," *Dermatologic Surg.*, vol. 32, no. 8, pp. 1031–1038, Aug. 2006.
[48] R. Fuksis, M. Greitans, O. Nikisins, and M. Pudzs, "Infrared Imaging System for Analysis of Blood Vessel Structure," *Elektron. ir Elektrotechnika*, vol. 97, no. 1, pp. 45–48, 2015.
[49] WebMD, "Chronic Venous Insufficiency: Symptoms, Causes, Diagnosis, Treatment," *WebMD LLC*, 2018. [Online]. Available: https://www.webmd.com/dvt/dvt-venous-insufficiency#1. [Accessed: 24-May-2018].
[50] D. Marr and E. Hildreth, "Theory of Edge Detection," *Proc. R. Soc. B Biol. Sci.*, vol. 207, no. 1167, pp. 187–217, Feb. 1980.
[51] S.-Y. Sun, "Ultrasound probe localization by tracking skin features," 2014.
[52] T. Niewiara, "What USB cameras are suitable with Vision Acquisition module for myRio." Cambridge, MA.
[53] P. van Walree, "Distortion," *Photogr. Opt.*
[54] P. Sheridan, "Practical aspects of clinical photography: Part 1 - Principles, equipment and technique," *ANZ J. Surg.*, vol. 83, no. 3, pp. 188–191, Mar. 2013.
[55] I. Kundu, X. Du, and B. Anthony, "Imaging platforms for registering and analyzing the skin microrelief structure," in *Health Monitoring of Structural and Biological Systems XII*, 2018,

vol. 10600, p. 29.
[56] M. Soriano, B. Martinkauppi, S. Huovinen, and M. Laaksonen, "Skin detection in video under changing illumination conditions," in *Proceedings 15th International Conference on Pattern Recognition. ICPR-2000*, vol. 1, pp. 839–842.
[57] "Keratosis pilaris," *American Academy of Dermatology*, 1938. [Online]. Available: https://www.aad.org/public/diseases/bumps-and-growths/keratosis-pilaris. [Accessed: 01-Jun-2018].
[58] "Psoriasis," *American Academy of Dermatology*, 1938. [Online]. Available: https://www.aad.org/public/diseases/scaly-skin/psoriasis. [Accessed: 01-Jun-2018].
[59] I. Lee, X. Du, and B. Anthony, "Hair segmentation using adaptive threshold from edge and branch length measures," *Comput. Biol. Med.*, vol. 89, no. C, pp. 314–324, Oct. 2017.
[60] D. Maltoni, D. Maio, A. K. Jain, and S. Prahakar, *Handbook of Fingerprint Recognition*, 2nd ed. London: Springer, 2009.
[61] D. G. Lowe, "Distinctive Image Features from Scale-Invariant Keypoints," *Int. J. Comput. Vis.*, 2004.
[62] M. Brown, R. Szeliski, and S. Winder, "Multi-Image Matching Using Multi-Scale Oriented Patches," in *2005 IEEE Computer Society Conference on Computer Vision and Pattern Recognition (CVPR'05)*, vol. 1, pp. 510–517.
[63] T. R. Jones, A. Carpenter, and P. Golland, "Voronoi-Based Segmentation of Cells on Image Manifolds," Springer, Berlin, Heidelberg, 2005, pp. 535–543.
[64] K. Q. I. Lee, "Computational tools for enabling longitudinal skin image analysis," 2016.
[65] "Feature Extraction," *The MathWorks, Inc.*, 2018. [Online]. Available: https://www.mathworks.com/discovery/feature-extraction.html. [Accessed: 23-May-2018].
[66] Matlab and Simulink, "Nearest Neighbor, Bilinear, and Bicubic Interpolation Methods," *The MathWorks, Inc.*, 2018. [Online]. Available: https://www.mathworks.com/help/vision/ug/interpolation-methods.html. [Accessed: 02-Jun-2018].
[67] M. Sonka, V. Hlavac, and R. Boyle, *Image Processing, Analysis, and Machine Vision*, 4th ed. Canada: Cengage Learning, 2015.
[68] S. Belongie, J. Malik, and J. Puzicha, "Shape matching and object recognition using shape contexts," *IEEE Trans. Pattern Anal. Mach. Intell.*, vol. 24, no. 4, pp. 509–522, Apr. 2002.
[69] A. S. Chaudhari, G. K. Patnaik, and S. S. Patil, "Implementation of Minutiae Based Fingerprint Identification System Using Crossing Number Concept," *Inform. Econ.*, vol. 18, no. 1, 2014.
[70] J. Munkres, "Algorithms for the Assignment and Transportation Problems," *J. Soc. Ind. Appl. Math.*, vol. 5, no. 1, pp. 32–38, 1957.
[71] "PRIMOS: Product Guide," *J. Am. Acad. Dermatol.*, 2011.
[72] R. R. Anderson, "Polarized light examination and photography of the skin.," *Arch. Dermatol.*, vol. 127, no. 7, pp. 1000–5, Jul. 1991.
[73] I. Kundu and B. Anthony, "Imaging the superficial vascular structure for mapping and identification," in *Health Monitoring of Structural and Biological Systems XII*, 2018, vol. 10600, p. 32.
[74] "Manta G-145 NIR," *Allied Vision Technologies GmBH*. [Online]. Available: https://www.alliedvision.com/en/products/cameras/detail/Manta/G-145 NIR.html. [Accessed: 23-May-2018].

[75] "What is absorbance/absorption spectroscopy?," *Edaphic Scientific*, 2018. [Online]. Available: http://www.edaphic.com.au/knowledge-base/articles/light-articles/what-is-absorbance-spectroscopy/. [Accessed: 05-Jun-2018].
[76] A. R. Tilley and S. B. Wilcox, *The Measure of Man and Woman: Human Factors in Design*, Revised. New York: John Wiley & Sons, Inc., 2002.
[77] "Best practices in phlebotomy," *WHO Guidel. Draw. Blood*, no. Geneva, 2010.
[78] E. Ali, E. Ullah Khan, E. Zarrar Mahmudi, and R. Ullah, "A Comparison of FAST, SURF, Eigen, Harris, and MSER Features," *Int. J. Comput. Eng. Inf. Technol.*, vol. 8, no. 6, pp. 100–105, 2016.
[79] D. V. Garbuzenko, N. O. Arefyev, and D. V. Belov, "Restructuring of the vascular bed in response to hemodynamic disturbances in portal hypertension.," *World J. Hepatol.*, vol. 8, no. 36, pp. 1602–1609, Dec. 2016.
[80] T. Aittokallio and B. Schwikowski, "Graph-based methods for analysing networks in cell biology," *Brief. Bioinform.*, vol. 7, no. 3, pp. 243–255, May 2006.
[81] S. Negahdaripour, R. Prados, and R. Garcia, "Planar homography: accuracy analysis and applications," in *IEEE International Conference on Image Processing 2005*, 2005, p. I-1089.

A

APPENDICES

A.1 Homography Overview

Assuming two points, (x,y) and $(\tilde{x}, \tilde{y})$, in images 1 and 2, respectively, the homography matrix, **H**, provides the translations and rotations relating image 1 and image 2 by solving the linear system with 9 unknowns. Since **H** Is not a square matrix, Singular Value Decomposition (SVD) is required to solve.

$$[\beta_1, \beta_2, \beta_3] = [x, y, 1] \begin{bmatrix} H_{11} & H_{12} & H_{13} \\ H_{21} & H_{22} & H_{23} \\ H_{31} & H_{32} & H_{33} \end{bmatrix}$$

Scaling Factor: $$\tilde{x} = \frac{\beta_1}{\beta_3}$$

From the linear system of equations: $$\beta_1 - \tilde{x}\beta_3 = 0$$

Plugging in the scaling factor:

$$xH_{11} + yH_{21} + H_{31} - x\tilde{x}H_{13} - y\tilde{x}H_{23} - \tilde{x}H_{33} = 0$$

A.2 Vein Code Overview

Pre-Processing Overview:

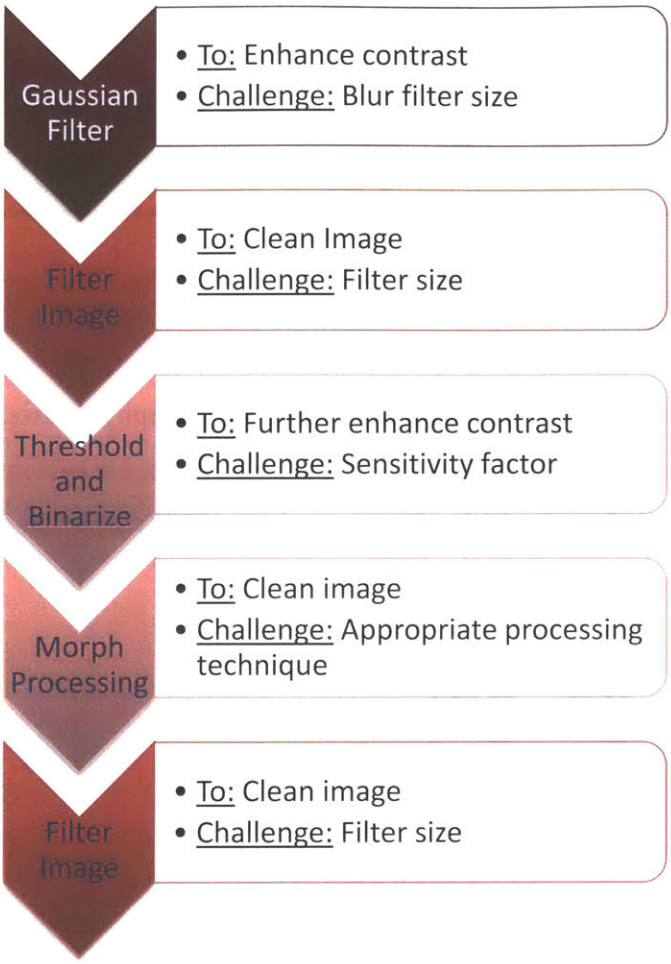

Registration Overview:

Stitching images is this process repeated over all images.

Detect Features from each of the vein images

Look for **Matching Features** between the two images and obtain locations

Apply obtained Transformation to one of the images to **align both images in the same reference frame**

Extract Feature Locations in each image

X	Y
256	367
445	317

Rot	Rot	X Trans
Rot	Rot	Y Trans
Rot	Rot	1

Using only the Strongest Matched Features, **find the transformation** between the images

Re-Localization Overview:

Similar process as registration: use features to find location of template within stitched image.

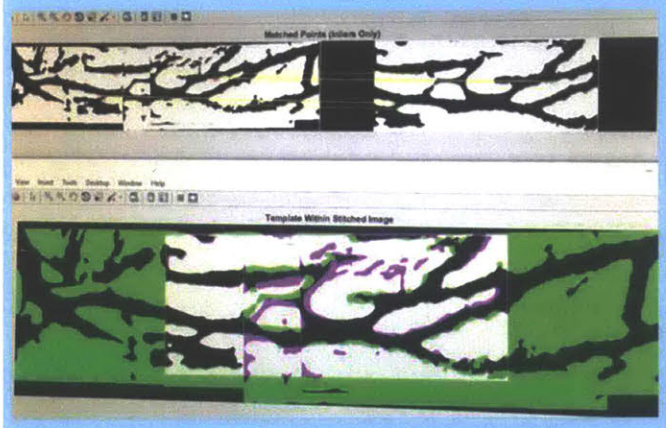

Detect Features from template and source image

Look for **Matching Features** between the two images and obtain locations

Apply obtained Transformation to one of the images to **align both images in the same reference frame**

Extract Feature Locations in each image

Using only the Strongest Matched Features, **find the transformation** between the images

A.3 Skin Registration and Matching Procedure

Algorithm flowchart for large area distortion registration and matching procedure

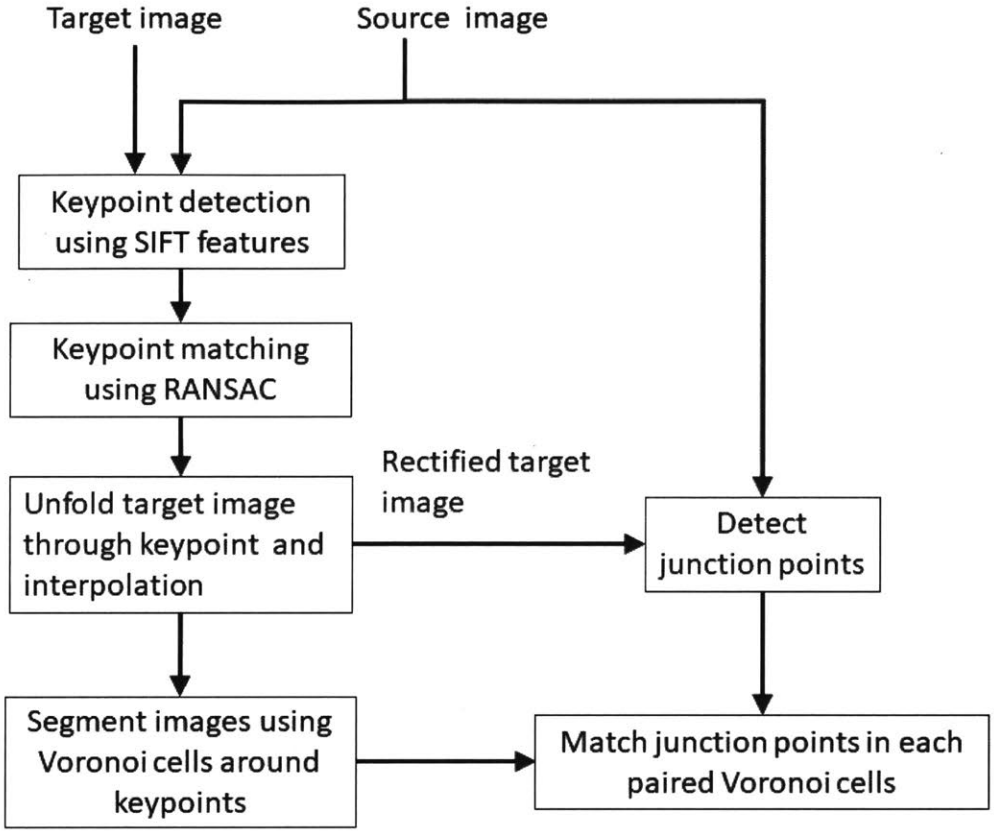

Voronoi cell-Based Point Pattern Matching (VC-PPM) of Skin Microrelief Structure

Algorithm *VC-PPM of skin microrelief structure*
Input: cost matrix

for the skin patches in pair Voronoi cells A and A' **do**

- *Extract shape context and for each junction point in the patches of A and A'*
- *Compute matching cost of junction points k_A of A and $k_{A'}$ of A' via bipartite matching*
- *Assign $k_{A'}$ to k_A if their matching cost is better than other matching with k_A*

end for

Output: matching list